Validation of Wall Shear Stress Measurements Obtained with Magnetic Resonance Velocimetry

Vom Fachbereich Maschinenbau
der Technischen Universität Darmstadt
zur
Erlangung des Grades eines Doktor-Ingenieurs (Dr.-Ing.)
genehmigte

Dissertation

vorgelegt von

Andreas Sebastian Bauer, M.Sc.

aus St. Ingbert

Berichterstatter:	Prof. Dr.-Ing. Cameron Tropea
Mitberichterstatter:	Prof. Dr.-Ing. habil. Sven Grundmann
Tag der Einreichung:	11.11.2019
Tag der mündlichen Prüfung:	28.01.2020

Darmstadt 2020

D 17

Bauer, Andreas:
Validation of Wall Shear Stress Measurements Obtained with Magnetic Resonance Velocimetry
Darmstadt, Technische Universität Darmstadt
Jahr der Veröffentlichung der Dissertation auf TUprints: 2020
Tag der mündlichen Prüfung: 28.01.2020

Bitte zitieren Sie dieses Dokument als:
URN: urn:nbn:de:tuda-tuprints-90309
URL: http://tuprints.ulb.tu-darmstadt.de/id/eprint/9030

Dieses Dokument wird bereitgestellt von TU Prints, E-Publishing-Service der Technischen Universität Darmstadt http://tuprints.ulb.tu-darmstadt.de
tuprints@ulb.tu-darmstadt.de

Dedicated to my wife Meike

Abstract

Wall shear stress acting on the vessel walls has been identified as an important factor for the initiation and development of cardiovascular diseases. *In vivo* measurements of the wall shear stress are usually conducted with Magnetic Resonance Velocimetry (MRV). Due to the limited spatial and temporal resolution, measurements in the near-wall region are challenging and the results are associated with high systematic and stochastic errors. Thus, an ongoing effort towards new post-processing methods to overcome this problem is observed. However, the underlying 'true' values of the wall shear stress are seldom known, inhibiting the evaluation of these methods.

The present thesis is devoted to investigate this problem by conducting *in vitro* MRV measurements under well-known flow conditions and by providing reliable reference values of the wall shear stress. Flow situations have been selected in which wall shear stress values from laser Doppler velocimetry (LDV), analytical solutions, and results from numerical simulations are available as a reference. The *in vitro* experiments are performed in various flows with a step-by-step increase of the complexity, ranging from simple steady laminar pipe flows to unsteady transitional flows through complex geometries, representative for the human aorta.

Extensive LDV measurements are presented, and the results of the velocity fields and wall shear stresses are compared to the MRV measurements. This thesis discusses possible systematic and random sources of errors in both measurement techniques. Additionally, it provides helpful advice for the practical measurement of the wall shear stress with LDV.

In the course of this work a database has been established, which contains the MRV data as well as the corresponding reference wall shear stress values acquired under the well-known and controlled flow conditions. This database has been used by other research groups in a collaborative interdisciplinary project, which has the final goal of improving the estimation of the wall shear stress from MRV data.

Kurzfassung

Für die Entstehung von Herz-Kreislauf-Erkrankungen wurde die Wandschubspannung auf Gefäßwände als wichtige Größe identifiziert. *In vivo* Messungen der Wandschubspannung werden gewöhnlich mittels Magnetic Resonance Velocimetry (MRV) durchgeführt. Aufgrund einer begrenzten räumlichen und zeitlichen Auflösung sind Messungen in Wandnähe allerdings schwierig, sowie mit hohen systematischen und zufälligen Fehlern verbunden. Daher ist ein Trend zu beobachten, dieses Problem mit einer Nachbearbeitung der Daten lösen zu wollen. Die ‚wahren' Werte der zugrunde liegenden Wandschubspannung bleiben in der Regel allerdings unbekannt, was eine Evaluierung neuer Methoden schwierig gestaltet.

Die vorliegende Arbeit untersucht dieses Problem, indem *in vitro* MRV Messungen unter bekannten Strömungsbedingungen durchgeführt werden, sowie zuverlässige Referenzwerte der zugrunde liegenden Wandschubspannung ermittelt werden. Es wurden Strömungen ausgewählt, für welche Referenzwerte aus Laser-Doppler-Anemometrie (LDA) Messungen, analytischen Lösungen sowie numerischen Berechnungen vorliegen. Die *in vitro* Experimente werden in verschiedenen Strömungen mit einer schrittweisen Steigerung der Komplexität durchgeführt, beginnend von einfachen stationären laminaren Rohrströmungen, bis hin zu instationären transitionellen Strömungen durch komplexe Geometrien, die repräsentativ für die menschliche Aorta sind.

Umfangreiche LDA Messungen werden vorgestellt, deren Ergebnisse bezüglich der Geschwindigkeitsfelder und Wandschubspannungen mit MRV Messungen verglichen werden. Diese Arbeit diskutiert mögliche systematische und zufällige Fehlerquellen beider Messtechniken. Weiterhin werden praktische Hinweise zur Messung der Wandschubspannung mittels LDA gegeben.

Im Verlauf dieser Arbeit wurde eine Datenbank aufgebaut, welche die MRV Daten sowie die dazugehörigen Referenzwerte der Wandschubspannung enthält, welche unter den bekannten Strömungsbedingungen gemessen wurden.

Diese Datenbank wurde von anderen Forschungsgruppen innerhalb eines interdisziplinären Projekts genutzt, um letztendlich die Bestimmung der Wandschubspannung aus MRV Daten zu verbessern.

Acknowledgments

First, I would like to thank Prof. Cameron Tropea for giving me the opportunity to work at the *Institute for Fluid Mechanics and Aerodynamics* at the *Technische Universität Darmstadt*, and for advising me during my doctoral work. Second, I would like to express my sincerely thanks to Prof. Sven Grundmann for agreeing to be a second reviewer of this thesis. Without Sven, I would have never become acquainted with this topic.
The financial support from the DFG through Grant TR 194/56-1 is also thankfully acknowledged.
I am very appreciative of the support I received from apl. Prof. Suad Jakirlić and my colleagues Maximilian Bopp and Sebastian Wegt. Their numerical simulations, which are presented in this thesis, greatly improved the outcome of my work.
I would also like to thank my colleagues Axel Krafft and Nina Shokina from the University of Freiburg as well as Gabriel Teschner from the Institute for Numerical Analysis and Scientific Computing, who all worked together with me on this interdisciplinary collaborative project. Thank you for the good and productive time we had during our measurements in Freiburg.
I would like to thank Ilona Kaufhold and her team from the mechanical workshop, as well as Martin Weiß from the electrical workshop for their support and the last-minute work before several measurement campaigns in Freiburg. Also all the student thesis projects as well as the support of my student assistant Jonas Gröger enhanced the experimental outcome of this thesis.
Special thanks go to all present and former colleagues in Griesheim, who made the last years not only fruitful through discussions and helpful advice, but also a very enjoyable place to work. These are Johannes Feldmann, Fabian Tenzer, Maximilian Kuhnhenn, Johannes Kissing, Jan Breitenbach, Benedikt Schmidt, Max Luh, Till Kaupe, Bernhard Simon, Martin Bruschewski, Daniel Freudenhammer, Florian Wassermann, Alexander Beck, Klaus Schiffmann, Amandine Guissart, Patrick Seiler, Lingxi Li, Kilian Köbschall, Philipp Brockmann and Niklas Apell.
Last but not least I would like to thank my wonderful wife Meike and my parents for their endless support, not only during my time in Darmstadt, but during all my life. Thank you for encouraging me and always standing by my side.

Contents

1 Introduction

In the present chapter the motivation and the background of this thesis are presented. The timeliness and relevance of the current study is shown using a critical review of previously published studies, and the goals and structure of this work are introduced. Parts of this chapter have already been published in Bauer et al. (2019).

1.1 Motivation

During the past two centuries the human life expectancy has increased from 25 years to more than 65 years (Oeppen et al., 2002). This increase in life span is mainly based on advances in health care, food supply and an overall increase in prosperity. Nevertheless, through the extended lifetime, the human body can be submitted to higher stress levels. This assumption is supported by the findings of McMahon & Bonner (1983); Levine et al. (1997) and Vennemann et al. (2007). Examination of the circulatory system of mammals reveals that the number of heartbeats per lifespan is almost constant over all species, except for humans. When the life expectancy of a mammal is compared to its cardiac cycle, a remarkable correlation exists, shown in Figure 1.1. Among all mammals, human life expectancy differs the most from the correlation, which suggests the assumption that the circulatory system, including arteries, veins and the heart, may be subject to a higher risk of disorders and diseases. In fact, at 23 %, the major cause of death in developed countries is associated with cardiovascular diseases, increasing dramatically with a person's age (Siegel et al., 2018).
A prominent example of such a change is the enlargement of the aortic vessel diameter, so called abdominal aortic aneurysms (Figure 1.2a), whose initiation and growth-triggers are subject to current discussions (Aggarwal et al., 2011; Kemmerling & Peattie, 2018). In general, the question needs to be answered, under which conditions the rupture of such an aneurysm is most likely, and at

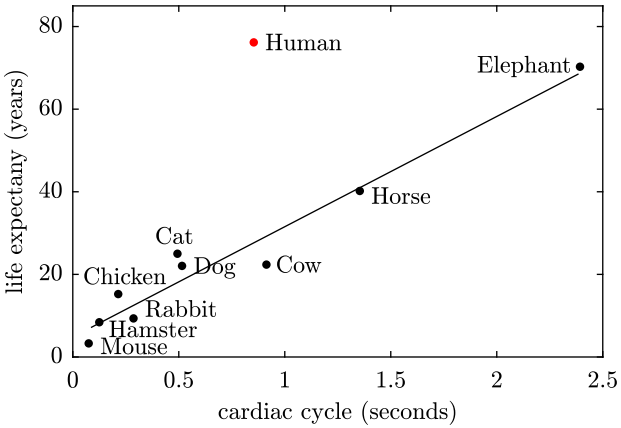

Figure 1.1: Cardiac cycle of mammals compared to their life expectancy, adapted from Vennemann et al. (2007). Mammals with a low cardiac cycle die earlier, while species with a long cardiac cycle live longer. Humans exhibit an outstanding position.

which stage of development surgical intervention is reasonable (Fillinger et al., 2002; Munarriz et al., 2016). Another kind of vascular disease is atherosclerosis (Figure 1.2b) where various types of tissue accumulate in the vessel wall, thus forming plaque and narrowing the cross-sectional area of the lumen. At those so-called stenosis, a thrombus may form with a potential chance to detach and subsequently occlude the entire vessel downstream, leading to an infarction or stroke (Lusis, 2000).

Beside the congenital risk factors for such diseases, vessel walls of mammals may transform and adapt over time due to biochemical processes (Davies, 2009). One trigger mechanism for those transformations is the blood flow, acting on the vessel wall. The endothelium, which is the inner cell layer of the vessel, is sensitive to mechanical influences introduced by the flow field (Lasheras, 2007; Davies, 2009).

Almost all investigations corroborate that the mechanical tangential force per unit area, which is introduced due to the friction between the blood and the vessel wall, the so-called wall shear stress (WSS), is of major importance in the emergence and development of many cardiovascular diseases. However,

different opinions exist about which quantitative values of the wall shear stress initiate which kind of disease. Since the WSS is highly temporally and spatially distributed, as well as being a vectorial quantity, the specification of a single value may not be appropriate. The general assumption at the moment is, that very high or low magnitudes of the WSS contribute to aneurysm growth (Boussel et al., 2008; Watton et al., 2011; Miura et al., 2013; Boyd et al., 2016), while spatial gradients provoke the initial development (Meng et al., 2007; Boussel et al., 2008; Dolan et al., 2013). Regarding the formation of atherosclerosis, regions of low WSS, e.g. recirculation zones at bifurcations, are at a higher risk to be affected (Chiu & Chien, 2011). Nevertheless, no consensus exists on these issues and the discussion is still in progress (Davies, 2009). Chiu & Chien (2011) and Arzani & Shadden (2016) provide a good overview of the current state of the art.
In summary, the knowledge of the wall shear stress in vessels may be beneficial not only for the treatment of existing diseases, but can hopefully be used in the future as an indicator for prophylactic and early treatments in cardiovascular medicine. Due to the aforementioned reasons, a high demand for accurate and reliable wall shear stress measurements within the human body (*in vivo*) exists in the medical community.

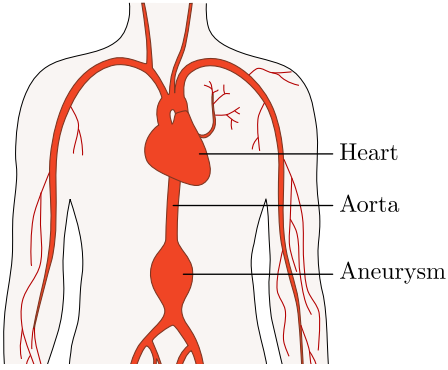

(a) Enlargement of a vessel in the human abdomen, a so-called abdominal aortic aneurysm.

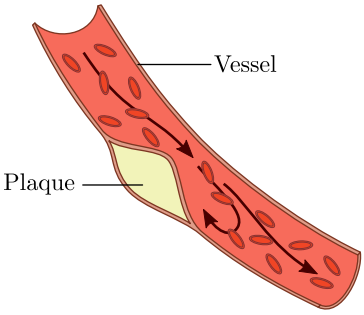

(b) Cross sectional view of a vessel with atherosclerosis, which leads to a disturbed blood flow.

Figure 1.2: Examples of cardiovascular diseases.

1.2 Measurement of Wall Shear Stress

In this section, the most common methods for an *in vivo* measurement of the wall shear stress are reviewed from the literature and existing problems in this field are pointed out.

The shear stress τ is in general defined as the product of the shear rate $\dot{\gamma}$, a measure of the deformation of the fluid elements, and the dynamic viscosity $\eta(\dot{\gamma})$, thus

$$\tau = \eta(\dot{\gamma})\dot{\gamma}\,. \tag{1.1}$$

For an incompressible Newtonian fluid the shear stress at the wall (wall shear stress) τ_w is simply

$$\tau_w = \eta \left.\frac{\partial u}{\partial y}\right|_{y=0}\,, \tag{1.2}$$

where u is the velocity component tangential to the wall and y the coordinate in wall normal direction (Spurk, 2013). τ_w can either be measured directly at the wall with a sensor, which is sensitive to the shear $\dot{\gamma}$ (usually requires calibration), but the most common practice is to determine τ_w from the flow field. The calculation includes three steps, which are

1. the measurement of the velocity field as close to the wall as possible,
2. the determination of the position of the wall and
3. the calculation of the velocity gradient at this position.

The first step, the *in vivo* measurement of the velocity field, can be achieved with the following measurement techniques (Vennemann et al., 2007).

Optical Particle Image Velocimetry (PIV) is based on the displacement of tracer particles between two consecutive captured image frames. A high speed camera is focused on the region of interest, which is usually illuminated with a synchronized pulsed laser source. Depending on the technique, the illuminated region is either two or three dimensional, and two or three velocity

components can be measured. The velocity is calculated in post-processing by dividing the captured frame into smaller interrogation areas, for which the displacement between the images is determined via cross correlation.
For *in vivo* applications, tracer particles are either the red blood cells or fluorescent liposomes, which are added to the blood. Typical spatial and temporal resolutions depend strongly on the optical setup and camera, but are in the order of 0.1 µm and 1 ms.
As this technique requires optical access, the tissue covering the vessel of interest needs to be removed during surgical intervention. The vessel also needs to be transparent to some extent. Despite its superior spatiotemporal resolution, optical PIV is therefore only used in animal experiments (Poelma et al., 2008; Jamison et al., 2013).

Ultrasound Particle Image Velocimetry, also known as *EchoPIV*, uses the same post-processing methods as optical PIV to determine the flow velocity between two consecutive images. However, images are acquired with ultrasonic transducers. The amplitude and time delay of reflected sound waves are used to generate the image.
Micro air bubbles are usually injected as seeding particles for *in vivo* applications, which reflect the incident sound waves in a different manner than the surrounding tissue and thus are clearly visible in the image. The spatial resolution is in the order of 0.1 mm, while 1 ms temporal resolution can be achieved.
This non-invasive method is used for animal experiments and sometimes also for human research. Due to the relatively large effort, EchoPIV is not employed in clinical routine (Zhang et al., 2009; Zhou et al., 2018).

Magnetic Resonance Imaging (MRI) uses the proton spin of hydrogen atoms, which are exposed to a strong magnetic field. A radio frequency pulse is applied to excite the spins within the volume of interest. The precession frequency of the spins is linearly proportional to the local magnetic field strength, which is subsequently altered with additional magnetic gradient fields. As a consequence, the frequency and phase of the precessing spins are changed, which in turn is used for spatial encoding during reconstruction. Additionally, the velocity of moving spins can be encoded in the phase, which is used to measure flow velocities (Haacke et al., 1999; McRobbie et al., 2006).

In principle, the resolution is only limited by the time the patients can hold still, but is typically in the order of 100 ms (time-averaged) and 1 mm for *in vivo* applications.
Due to the great distribution in medical diagnostics as well as its fast and easy usage, MRI is the most common technique for *in vivo* flow measurements today.

In the medical community, flow measurements using MRI are mostly referred to as phase contrast magnetic resonance imaging (PC-MRI), while in the engineering context the term Magnetic Resonance Velocimetry (MRV) is used. In the past two decades, considerable progress has been achieved regarding time-resolved, three-dimensional MRV measurements, which include velocity encoding in all three spatial directions. The most prominent sequence is the 4D flow sequence (Markl et al., 2012), sometimes also referred to as 4D flow MRI. Beside its popularity in the medical diagnosis, it has to be emphasized that MRV was recently discovered by engineers as a valuable tool to measure technical flows (Elkins & Alley, 2007). Examples are the flows through the models of an internal combustion engine or turbine blade cooling channels (Freudenhammer et al., 2014; Bruschewski et al., 2015).
The wide acceptance of MRV is based upon numerous advantages over other measurement techniques. First of all, it is non-invasive, making it a powerful tool in routine diagnostics and early detection examination. For experimental investigations, this allows the examination of internal flow fields with opaque walls or at locations where no optical access is possible. The non-ionizing radiation is beneficial in contrast to computed tomography (CT). MRV can capture velocity fields starting from a two-dimensional slice with only one velocity component (2D1C) up to a three-dimensional field including all velocity components (3D3C) without additional experimental effort. Probably the most significant advantage in comparison to other *in vivo* measurement techniques is the fact that MRI scanners are available in most hospitals for conventional imaging anyways.
MRV does not only offer advantages, but also exhibits a number of disadvantages. Measurements of unsteady phenomena are only possible if the flow is periodic. In this case, phase-averaged measurements can be performed. It has to be emphasized that current developments, especially in the field of data reconstruction, allow very fast acquisitions up to several images per second

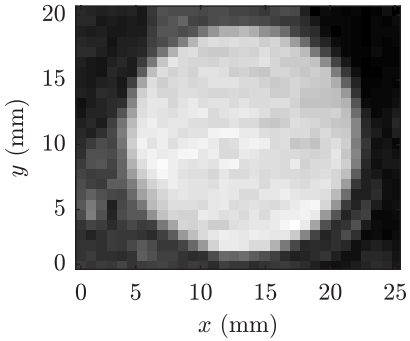

(a) MRI scan of the human aorta. Although this is the largest human vessel and the spatial resolution is rather fine (0.8 mm), the WSS will be subject to high errors.

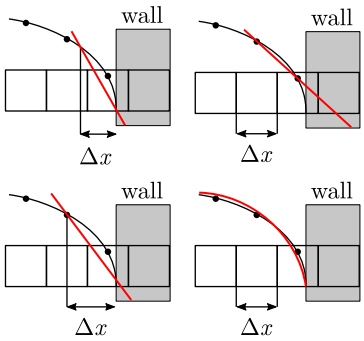

(b) Different methods to evaluate the velocity gradient (red) from measurement values (black dots). The black curve represents the true velocity. Adapted from Petersson et al. (2012).

Figure 1.3: Example of MRI data and post-processing methods.

(Lustig et al., 2007). This reconstruction technique, called *compressed sensing*, may be used in the future to significantly reduce measurement time and give access to 'true' unsteady quantities.

Probably the most significant drawback of MRV is its spatial resolution of about 1 mm for *in vivo* measurements. For large objects like bones and organs this does not represent a major problem. However, flow measurements in small vessels are not possible, and even in larger vessels like the aorta, shown in Figure 1.3a, the spatial resolution is far from being sufficient to accurately investigate the flow field close to the wall. The spatial resolution is even more severe for the calculation of the WSS. As outlined before, three steps are necessary to estimate τ_w. Each of these strongly rely on a high spatial resolution.

To circumvent this drawback, numerous techniques have been developed to estimate τ_w from the sparse MRV data. The determination of the position of the wall, which is the second step of the calculation of the WSS, is often performed manually (Stalder et al., 2008; Frydrychowicz et al., 2009; Bieging et al., 2011; Cibis et al., 2014). Several points at the boundary are selected by an user and afterwards the curvature of the wall is smoothed with splines.

This procedure is carried out for each slice and each time step, thus it is time consuming as well as user-specific. A better approach is the automated detection of the boundary, which can be achieved for example with a level-set method (Cheng et al., 2002; Van Ooij et al., 2013). The most common method is thresholding, where all voxels below a certain value in the image are excluded. This can be performed either by means of the magnitude data (Oyre et al., 1997; Papathanasopoulou et al., 2003; Ahn et al., 2007; Boussel et al., 2009) or from the velocity information (Box et al., 2007). For thresholding of the velocity data, the velocity image is averaged over the cardiac cycle, which subsequently yields a mean flow field. In some cases the determination of the wall is even missed, and the wall is assumed to be located at the position of zero velocity from the subsequent processing of the velocity field.
The last step, the calculation of the gradient at the vessel wall, incorporates in most cases an interpolation scheme. Some authors interpolate the entire velocity field of the vessel with splines or polynomials (Papathanasopoulou et al., 2003; Ahn et al., 2007). Other authors even assume a Hagen-Poiseuille velocity profile, actually only valid in fully developed laminar pipe flow (Box et al., 2007; Efstathopoulos et al., 2008). In most cases, the velocity information is interpolated along a vector perpendicular to the wall. Sometimes only the wall-next velocity information is used, resulting in a linear interpolation (Oyre et al., 1997; Boussel et al., 2009; Bieging et al., 2011), but often several voxels are used together with splines and higher order polynomials (Köhler et al., 2001; Cheng et al., 2002; Stalder et al., 2008; Cibis et al., 2014; Potters et al., 2015).
Figure 1.3b shows some methods to determine the velocity gradient. It is obvious that those methods depend strongly on the velocity field, the spatial resolution and the applied methods. The low spatial resolution generally results in an underestimation of the WSS, yielding errors of up to 40 % (Petersson et al., 2012).

1.3 Interdisciplinary Project

As outlined in the previous section this problem is manifold, and satisfying solutions have not yet been proposed. However, it is apparent that collaboration within an interdisciplinary group will be essential to make further progress. One such collaboration has been established among the Department of Radiology from the University Medical Center Freiburg, the Institute of Numerical and Scientific Computing from the TU Darmstadt, and the Institute of Fluid Mechanics and Aerodynamics from the TU Darmstadt. The overall goal is to improve the estimation of the WSS with MRV.
On the one hand, the MRV measurement technique itself is improved by the radiology group. New sequences especially suited for the near-wall region at high spatial resolutions are developed. On the other hand, a remarkable improvement is proposed due to the application of a variational *data assimilation* to process the sparse and noisy MRV data and to obtain a refined estimate of the flow field. The refined flow field can be used to improve the estimation of wall shear stress, since the gradient can then be better approximated in the near-wall region. This step is carried out by the mathematicians at TU Darmstadt. Data assimilation relies neither solely on measurement data nor on numerical simulations, rather these two inputs are used in combination. This method has already been successfully used on MRV data for two-dimensional flows in Egger et al. (2017). It has also been used extensively in other fields, for example in meteorology to utilize measurement data from sparse and unevenly distributed weather stations around the globe in numerical computations of weather forecasts (Ghil & Malanotte-Rizzoli, 1991), or to refine and improve PIV data (Schneiders & Scarano, 2016; Yang et al., 2017).
The present approach significantly differs from other studies, in that a strong emphasis is placed on a preliminary assessment step, carried out by the fluid mechanics group, which is the topic of this thesis. In this additional step the reliability of the WSS estimates from MRV is first evaluated using comparisons to *ground truth*, sometimes also called *gold standard*. The term ground truth refers to the knowledge of the 'true' value of a quantity, to which the measured or computed results are compared. If the ground truth remains unknown, like in almost all *in vivo* MRV measurements, it is rather difficult or even impossible to evaluate and quantify a post-processing method regarding expectation, variance and reproducibility. This notion is not new (Carvalho

et al., 2010; Markl et al., 2010, 2011; Potters et al., 2015; Van Ooij et al., 2015), but has often been neglected (D'Elia et al., 2012).
Lacking such comparisons, there exists a variety of rather unsuitable alternatives. Some authors resort to comparisons of relative WSS values to each other (Van Ooij et al., 2015), for instance using WSS values before and after a surgical intervention, or WSS values between patients and healthy volunteers measured with the same MRV sequence. Comparability between different studies or research groups is in general relatively poor, since the absolute values remain unknown. Other authors revert to computational fluid dynamics (CFD), which are often thought to provide a gold standard (Boussel et al., 2009; Piatti et al., 2017). However, this should be viewed critically, since the flow within the aorta can be in the transitional regime between laminar and turbulent, which is extremely challenging even for advanced CFD simulations; hence, the results may be questionable for serving as ground truth (Glaßer et al., 2014). Even if the flow domain is not in the transitional or turbulent regime, results from CFD may vary widely. A good example are so-called CFD challenges, where different research groups compute the same problem set, i.e. the flow through aneurysms (Steinman et al., 2013; Berg et al., 2015; Janiga et al., 2015; Valen-Sendstad et al., 2018). The disparity between these results is large. Another approach to test WSS estimators is the generation of synthetic flow fields and associated synthetic MRV data, with a subsequent application of the post-processing algorithm (Carvalho et al., 2010; Piatti et al., 2017). However, also this procedure should be viewed critically, since it is unlikely that all influencing physical quantities and noise sources can be captured properly in such synthetic data generation.
The problem can only be solved if the *in vivo* flow conditions are abstracted to more simple and controllable flows, which are reproduced with an experimental setup (*in vitro*). Also an *alternative* measurement technique is required, which is better suited for the measurement of WSS. Results from MRV can then be compared to this reference. Table 1.1 gives an overview over the most common experimental methods for the *in vitro* determination of the WSS (Tropea & Yarin, 2007). In general, those measurement techniques can be classified in *invasive* and *non-invasive* techniques. Invasive techniques always influence the flow field up to some extent and are therefore not recommended if other techniques are available. Some of those invasive techniques like surface hot-wire, hot-film, oil film and floating elements rely on a direct measurement

Table 1.1: Comparison of common WSS measurement techniques, including a reason why the respective method was not used in this thesis.

Measurement technique	Invasive	Optical access	Direct	Why not used?
PIV		×		Light refraction
LDV		×		
Hot-wire	×			Highly intrusive
Surface hot-wire	×		×	Single point
Hot-film	×		×	Single point
Oil film	×	×	×	Not time-resolved
Floating element	×		×	Single point
Pressure drop			×	Integral value

of the WSS, which means that they produce a signal directly proportional to the WSS. However, those methods require time-consuming calibration. Additionally, most invasive methods like surface hot-wire, hot-film and floating element are located at a single location. A spatial distribution of the WSS cannot be measured. Other restrictions may be that they are not compatible with water flows or restricted to time-averaged values. A very simple method is the calculation of the WSS from the pressure drop. The drawback is that this method only gives integral values. PIV is a common method, which is well-suited due to its high spatial and temporal resolution. However, due to a limited depth of view from the camera, the optical setup requires that the refractive indices of the fluid and the flow model are matched, which is not possible in this study.

Laser Doppler velocimetry (LDV) is a non-invasive technique, which can measure the fluid velocity very close to the wall and thus determine the WSS with a much higher precision compared to MRV. In comparison to other techniques LDV offers the best trade-off regarding spatial and temporal resolution as well as applicability. LDV is therefore used to obtain reference values of the WSS in this study.

1.4 Objectives and Outline of the Current Work

The current work is devoted to provide the aforementioned ground truth reference for wall shear stress measurements. In a first step, this includes the selection and supply of well-defined flow fields with an experimental setup. Subsequently MRV data of those flows are acquired for the newly developed data assimilation. In a second step, additional information about the 'true' WSS values of these flows are obtained. For those reference measurements laser Doppler velocimetry is used. It is the purpose of this thesis to develop methods and to provide guidelines on how ground truth experiments for MRV WSS measurements can be conducted. As outlined in the previous section, this step has not been performed to such an extent in any other study. Hence, this work is assumed to contribute to the field of experimental and *in vitro* measurement techniques as well as to the overall interdisciplinary goal of improving WSS measurements.
The present thesis is structured as follows:
In **chapter 2** the methods and experimental setups are presented. As *in vivo* flows are far from being well-defined, simplifications of the circulatory system are proposed, which are suitable for experimental investigations. The flow supply system, designed to achieve such flows, is presented. Finally, the basic principles of the measurement techniques LDV and MRV used throughout this thesis are introduced.
In **chapter 3** methods to accurately measure the WSS with LDV are developed. To evaluate the results and to identify possible sources of errors, rather simple flows through straight pipes are used. The purpose of this step is to use mostly laminar flows with analytical solutions.
In **chapter 4** techniques and results obtained from chapter 3 are applied to more complex flows, where no analytical solutions are available. On the basis of a common *in vivo* situation, the model of an aneurysm is therefore exemplary used. In this chapter, WSS results from LDV are compared to CFD and, where possible, literature values.
In **chapter 5** conclusions are drawn and an outlook is given.

2 Methods and Facilities

This chapter provides an overview of existing experimental methods and facilities. In **section 2.1** the fluid mechanical conditions in the human aorta are described and expressed with dimensionless parameters to properly reproduce those conditions in *in vitro* experiments. **Section 2.2** describes the flow supply unit, which is necessary to provide these conditions. Subsequently a short overview of the relevant measurement techniques used in this study (LDV and MRV) is presented in **section 2.3**. Parts of this chapter have already been published in Bauer et al. (2019).

2.1 Abstraction of the Human Aorta

Similarity between *in vivo* and *in vitro* flow fields is ensured, when geometric, kinematic and dynamic similarity is given. As the spatial resolution is a crucial parameter for the estimation of the wall shear stress from MRI data, the geometric dimensions of the aorta have not been scaled for the experiments in the present study. Hence, geometric similarity is always given. For an incompressible fluid, where body forces can be neglected, two dimensionless numbers are required in order to guarantee kinematic and dynamic similarity. The first dimensionless number is the time dependent Reynolds number $Re(t)$

$$Re(t) = \frac{U(t)d}{\nu} = \frac{\text{inertia forces}}{\text{viscous forces}}, \tag{2.1}$$

with the cross sectional mean velocity $U(t)$, the pipe (or vessel) diameter d and the kinematic viscosity ν. Re describes the ratio of inertia forces to viscous forces. The second dimensionless number is the Womersley number Wo

$$Wo = R\sqrt{\frac{\omega}{\nu}} = \frac{\text{transient inertia forces}}{\text{viscous forces}}, \tag{2.2}$$

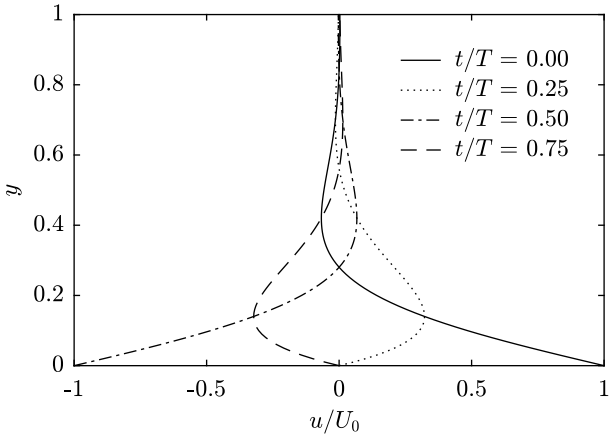

Figure 2.1: Exemplary velocity field of Stokes second problem for different times t/T during the cycle, adapted from Brenn (2016). The wall at the bottom oscillates periodically and transfers momentum into the fluid.

first described by Womersley (1955), where R is the pipe radius and ω the (pulse) frequency. The Womersley number is closely related to the Stokes layer thickness δ, derived from Stokes second problem:
Consider an infinite flat plate, which oscillates periodically in tangential direction with frequency ω and velocity amplitude U_0. The plate is surrounded by a viscous fluid. Then the solution of the fluid velocity u is given in the form (Brenn, 2016)

$$u(y,t) = U_0 e^{-\sqrt{\omega/2\nu}\, y} \cos(\omega t - \sqrt{\omega/2\nu}\, y)\,, \tag{2.3}$$

where y is the coordinate normal to the plate and t the time. Figure 2.1 shows the velocity field at specific times during the cycle. The term $\sqrt{\omega/2\nu}$ defines the damping rate of the oscillations. Its inverse is the Stokes layer δ

$$\delta = \sqrt{\frac{2\nu}{\omega}}\,, \tag{2.4}$$

which is a measure of how far momentum due to viscous forces is transferred from the wall into the fluid. In this problem domain, there exists no appropriate scaling factor for the length scale, thus a dimensionless number

Table 2.1: Typical dimensionless numbers and length scales of the human aorta from literature. Since *Re* is time dependent, it is common to specify time averaged and maximum values. The bottom row shows the range of values which are used in this study.

Publication	Re_{ta} (-)	Re_{max} (-)	*Wo* (-)	*d* (mm)
Caro (2012)	1785	4891	20	19-25
Fortini et al. (2015)	2174-3220	-	15	27
Kousera et al. (2013)	-	4000-5700	17-24	-
Liepsch et al. (1992)	1350	-	20	-
Moore & Ku (1994)	590	-	16	24.2
Ohmi et al. (1982)	1250	7000	17	-
Wolak et al. (2008)	-	-	-	24
Present study	**1300-5300**	**3952-7651**	**20**	**26**

cannot be defined. Equation 2.3 can be rewritten for the case of an oscillating flow field with stationary walls, for example a pressure driven oscillating flow through a pipe. A typical length scale is then given as the pipe radius R. Thus, a dimensionless number can be defined, which is the Womersley number $Wo = \sqrt{2}R/\delta = R\sqrt{\omega/\nu}$. The Womersley number is a measure of how far, relative to the pipe radius, momentum due to viscous forces from the wall is transferred. *Wo* defines the ratio of transient inertia forces to viscous forces. For $Wo \ll 1$ viscous forces dominate, generating a large Stokes boundary layer, while for $Wo \gg 1$ inertia forces dominate and the wall effects are confined to a thin region in the vicinity of the wall.
Table 2.1 summarizes typical values from literature for *Re* and *Wo* found in the human aorta as well as the values chosen in the present study. Their rationale will be explained in the subsequent chapters.
The human aorta has a very complex, patient specific geometry, which is not very suitable for generic experiments. Also the *in vivo* flow conditions are far from being analytically accessible or well-defined, including irregular vessel shape, flexible walls, fluid structure interaction, transition to turbulence, patient specific viscosity, non-Newtonian fluids, slightly moving walls caused by patient respiration and many more. The objective of the current study is not to investigate flow phenomena within a specific aorta, but to develop

techniques, which can serve as ground truth experiments in aorta-like models. Therefore, some simplifications and abstractions of the aorta are required. In a first step, the following assumptions and simplifications are made for **all** flows within this study:

- **Incompressible and Newtonian fluids:** For Newtonian fluids, there exists a fixed ration between the shear rate and the shear stress (see Equation 1.2), thus the dynamic viscosity is constant. Blood is a very complex fluid, containing various sorts of fluids and solid particles like plasma, molecules, proteins and blood cells, which additionally tend to agglomerate and deform when submitted to stress (Chien, 1970). This makes it in general a non-Newtonian but incompressible fluid. However, the assumption of a Newtonian fluid is a valid assumption for the flow through large vessels like the aorta, where the influence of solid particles is negligible (Caro, 2012).
- **Rigid and stationary walls:** Vessels are in general elastic and the flow field may significantly differ between compliant and rigid boundaries (Lantz et al., 2011). Downstream of the heart, the pressure increases during systole and stretches the aorta. The blood flow is effectively stored in the ascending and descending aorta and continuously released over time through the small capillaries, known as the Windkessel model (Caro, 2012). However, since compliant models significantly increase the difficulty of the determination of the instantaneous wall position, rigid and stationary boundaries are assumed.
- **Axisymmetry:** Although this is not true for the aorta, the assumption is beneficial for the laser Doppler measurement technique, which cannot capture the entire flow field. By means of a careful experimental setup, the flow can therefore also assumed to be axisymmetric so that measurements at only one circumferential position need to be conducted.
- **Strict temporal periodicity of the flow rate:** Although not completely valid, this assumption is approximately true when the patient is calmly lying on the patient bed.

Despite all of these simplifications, flow conditions are still expected to be complicated. Measurements will therefore start with an easy experimental flow and increase complexity step-by-step to ensure that the flow conditions

are always known. During this process possible sources of errors can be detected more easily. Stages of abstraction of the human aorta are shown in Figure 2.2. These stages also represent the structure of the following chapters. The most simple flow is fully developed steady pipe flow (**section 3.1**). The complexity can be increased in the time domain by altering the flow conditions, for instance when a time varying, cyclic volume flow rate is applied. For a sinusoidal flow rate this results in pulsating pipe flow (**section 3.2**). Alternatively, an increase in complexity can be achieved by changing the geometry, for instance by using steady flows through generic aneurysm models (**section 4.1**). The last stage of abstraction is the combination of both geometric and flow complexity, i.e., pulsating flow through generic aneurysms (**section 4.2**).

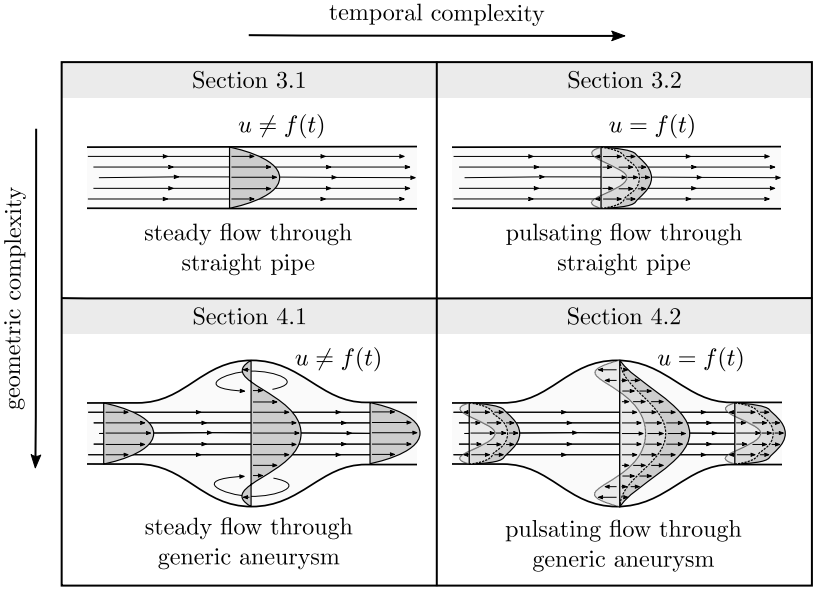

Figure 2.2: Different stages of abstraction of the human aorta. Complexity can either be increased in the temporal or spatial domains. These stages also represent the structure of the following chapters. Adapted from Bauer et al. (2019).

2.2 Flow System

The experimental setup is schematically shown in Figure 2.3. It comprises a portable flow supply unit explicitly designed for this study (shown in Figure 2.4) to generate the desired time-varying volume flow rate at specified temperatures. The flow is then guided through flexible hoses to the LDV or MRV measurement section.
Water is used as a working fluid, which is stored in a pressure tank and can be heated with a 1.5 kW immersion heater or cooled with a 0.45 kW dipping cooler (FT402, Julabo). The temperature in the tank is monitored with thermocouples and the fluid is constantly circulated to ensure a homogeneous temperature distribution. For the LDV experiments, the water is seeded with titanium dioxide tracer particles of approximately 1 µm diameter. For the MRV experiments, 1 g copper sulfate is added per liter of water to serve as a contrast agent, as suggested by Schenck (1996). It is emphasized that the contrast agent itself is not measured, contrary to the seeding particles for LDV measurements. Instead the copper sulfate reduces the relaxation time of the hydrogen spins and thus causes a faster decay of the electromagnetic signal, which in turn accelerates the MRI measurements. Copper sulfate of this concentration does not alter other relevant properties of the water.
The flow supply system contains two different pumps for either steady or unsteady flow conditions. The first pump is a magnetically driven centrifugal pump (RM-MS1, Sondermann) with a volume flow rate of up to $\dot{V} \approx 120\,\mathrm{L/\,min}$. Small volume flow rates can be achieved with an electronic frequency converter included in the pump, and additionally by pinching the whole system with a valve at the outlet. The second pump is a gear pump, driven by a computer controlled stepper motor (CardioFlow MR 5000, Shelley Med.), which can provide volume flow rates up to $\dot{V} \approx 18\,\mathrm{L/\,min}$. Time varying flow waveforms can easily be implemented via built-in software or a Matlab® code.
Downstream of the pumps the flow passes through a high precision Coriolis flow meter (CORI-FLOW M55, Bronkhorst) with a full scale range of $\dot{V} = 10\,\mathrm{L/min}$ and an accuracy of 0.2 % full scale, which is used for steady flow rates. For unsteady flows, the sensor is not fast enough to follow the volume flow rate precisely and thus underestimates the amplitudes. The flow rate is therefore extracted from the time resolved MRV data, as later

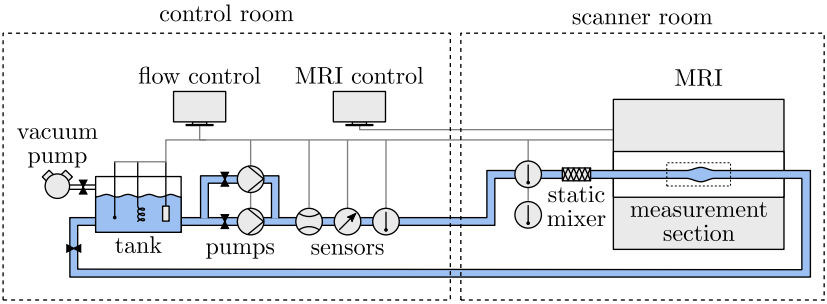

Figure 2.3: Schematic drawing of the experimental setup, here shown for the case of MRV measurements. Adapted from Bauer et al. (2019).

described in section 3.2.1. The flow supply unit provides a 5 V TTL trigger signal for the synchronization of the periodic flow with both the MRI scanner and the laser Doppler signal processor. All parameters of the flow supply unit are monitored and controlled via LabView®.
The fluid is guided from the flow supply unit with PVC hoses of 25.4 mm inner diameter to the measurement section. For the MRV experiments, the pump is placed in the control room next to the MRI scanner room and the hoses are passed through dedicated waveguides of the radio frequency cabin. To ensure fully developed flow conditions at the measurement section several precautions must be taken. All upstream disturbances caused by bends are eliminated with a static mixer. The design follows the guidelines of Paul et al. (2004) and is based upon the x-configuration (SMX) with a total of 8 elements, which are shifted at 90° to each other. The working principle of a static mixer is based on an interchange of fluid from different sides of the cross section with static elements. Downstream of the mixer an acrylic tube of $d = 26\,\text{mm}$ inner diameter and $l = 2\,\text{m}$ length is used as an inlet, corresponding to $l/d \approx 77$. This is the maximum length, which fits on the patient bed of the scanner. The measurement section downstream of the inlet pipe consists of the flow models introduced in Figure 2.2. These consist either of a $l = 1\,\text{m}$ long straight acrylic tube with $d = 26\,\text{mm}$ inner diameter, a high precision glass tube with $d = 25.885\,\text{mm}$ inner diameter, or an aneurysm model followed by a straight outflow of $l = 0.5\,\text{m}$ length.

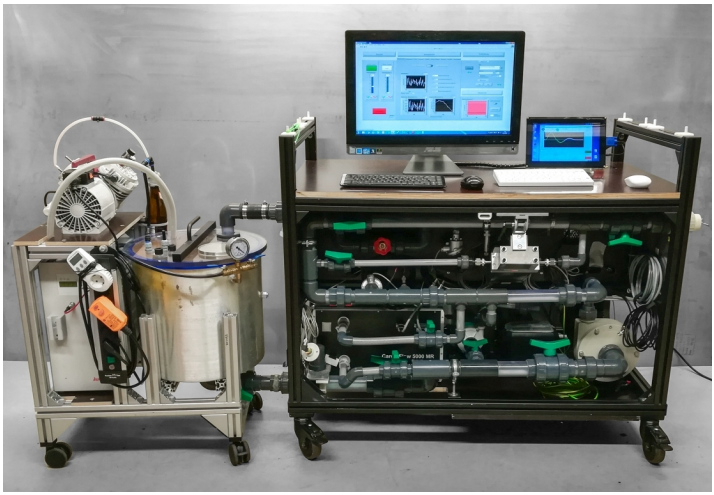

Figure 2.4: Flow supply unit designed for this study.

As pointed out later in section 3.1.1, heat exchange between the fluid and the surrounding air has to be avoided. Thus, the pipe is thermally insulated with a 20 mm thick layer of rubber, and inner and outer temperatures are matched. The room temperature and the fluid temperature are measured at the static mixer with two thermocouples of type K.
Furthermore, the water contains dissolved gases, which originate from the flushing process. After a short time, small air bubbles coalesce into larger bubbles and disturb the measurement process as well as the flow field. This is especially the case for unsteady flow rates, where the pressure during the decelerating parts of the cycle falls below the ambient pressure, which promotes the formation of bubbles. The air is removed with a vacuum pump before each experiment. An absolute pressure of $p = 0.1$ bar is applied to the whole system, including the tank, hoses and flow models, while the water is circulated to speed up the degassing process.

2.3 Measurement Techniques

In this section, the basic principles of the two measurement techniques LDV and MRV are introduced. Additionally, several system considerations for the experimental procedure are proposed.

2.3.1 Laser Doppler Velocimetry

The laser Doppler system used in this study is a two-velocity component system (Flow Explorer, Dantec Dynamics) operated in backscatter mode. Specifications are given in Table 2.2. The wavelengths of the laser beams are $\lambda_1 = 660\,\text{nm}$ and $\lambda_2 = 785\,\text{nm}$. Each laser diode has an output of $P = 120\,\text{mW}$. A short focal length of $f = 150\,\text{mm}$ is used to reduce the size of the measurement volume, which is beneficial for measurements close to the wall. The laser is split into two beams for each velocity component with a Bragg cell, which additionally introduces a frequency shift of $f_s = 80\,\text{MHz}$ in one of the beams for directional sensitivity. At the lens the laser beam diameter is $d_L = 2.6\,\text{mm}$ and the beam separation is $b_s = 60\,\text{mm}$. First order moments are calculated using transit-time weighting. The LDV head is mounted onto a three axis traverse (MS200HT, ISEL) with a minimum step size of $\Delta x = 12.5\,\mu\text{m}$ in each direction.
In the following section, only important features of the LDV technique are

Table 2.2: Specifications of the laser Doppler system used in the present study.

Parameter	Value
Laser power	$P = 120\,\text{mW}$
Wavelength laser 1	$\lambda_1 = 660\,\text{nm}$
Wavelength laser 2	$\lambda_2 = 785\,\text{nm}$
Frequency shift	$f_s = 80\,\text{MHz}$
Focal length	$f = 150\,\text{mm}$
Beam diameter at lens	$d_L = 2.6\,\text{mm}$
Beam separation at lens	$b_s = 60\,\text{mm}$

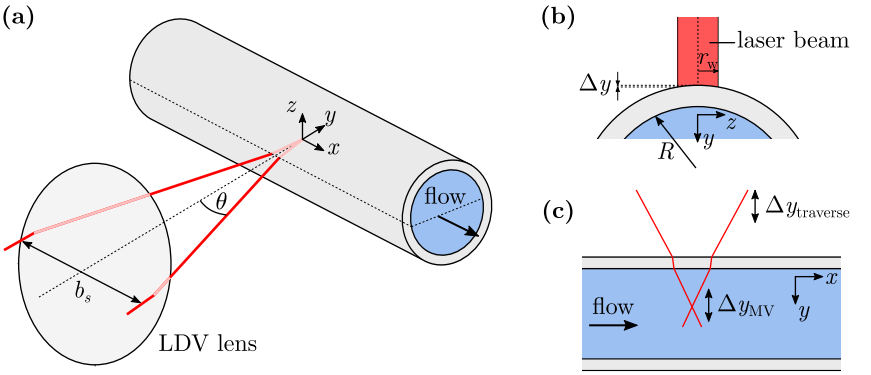

Figure 2.5: Visualization of the optical setup for LDV measurements of the axial velocity component in the straight pipe.

introduced, which are essential for the measurement of near wall flows and the wall shear stress. This section is based upon the book of Albrecht et al. (2013), where the basic principles of LDV can be found.

Optical Setup

The optical setup for measurements in pipe flows is depicted in Figure 2.5. The system is aligned with the first velocity component pointing in the streamwise direction x. The laser beams pass through the pipe at the center axis $z = 0$, thus refraction is only present in one plane (Figure 2.5c). The second LDV component (not shown here) is aligned such that the circumferential flow direction z can be measured. The velocity component in y-direction (radial) cannot be measured.
Due to the different incidence angles of the lasers, the two measurement volumes in general do not overlap. Thus, the measurement of both velocity components at the same time (coincidence) is not possible. A common method to circumvent this problem is matching the refractive indices of the fluid and the wall, and using a plane surface at the outer interface (Zhang, 2004). However, this requires for example a glycerol-water mixture instead of pure water, which is significantly more complex to handle. Since there is no mean velocity component in circumferential and radial direction in a pipe flow this

does not interfere with the measurements.
The refraction additionally results in a position error, as shown in Figure 2.5c. A movement of the traverse $\Delta y_{\text{traverse}}$ results in a different displacement of the measurement volume Δy_{MV}. For the current setup this can be calculated to $\Delta y_{\text{MV}}/\Delta y_{\text{traverse}} \approx 1.34$. Although the laser beams of the streamwise component are located at the pipe center axis $z = 0$, the curvature of the pipe may influence the beam path (Figure 2.5b). The laser beam is not infinitesimally small and thus the refraction of the beam differs along the z-direction. The outer radius of the pipe is $R = 16\,\text{mm}$, while the laser beam radius, assuming that it is near its beam waist, is $r_w \approx 24\,\mu\text{m}$. The height difference Δy over the beam cross section is $\Delta y \approx 3 \times 10^{-5}\,\text{mm}$, which is of the same order as the surface roughness of acrylic glass and therefore negligible.

Measurement Volume and Detection Volume Size

The size of the measurement volume (MV), which is the volume where the laser beams intersect and an interference pattern forms, is important for the measurement of WSS. The semi-axis b_0 of the measurement volume determines the minimum distance to the wall, at which a measurement can be performed (Figure 2.6). The knowledge of its size is also necessary for the correction of a possible velocity gradient bias, explained in the next paragraph. The MV size is defined as the location where the laser light intensity is below the threshold of e^{-2} of the maximum intensity. The MV size of the corresponding velocity component in streamwise direction can be estimated to

$$a_0 = \frac{r_w}{\cos\theta/2} \approx 24\,\mu\text{m}, \quad b_0 = \frac{r_w}{\sin\theta/2} \approx 164\,\mu\text{m}, \quad c_0 = r_w \approx 24\,\mu\text{m}, \tag{2.5}$$

with the beam waist radius r_w

$$r_w = \frac{2}{\pi}\frac{\lambda_1 f}{d_L} \approx 24\,\mu\text{m}\,, \tag{2.6}$$

and the intersection angle θ between the laser beams. A more appropriate definition of a volume is the detection volume (DV), which is the volume wherein tracer particles are detected. The DV size depends strongly on the optical setup, electronics and particles. Large particles for example may scatter enough light due to their size to be detected by the signal processor

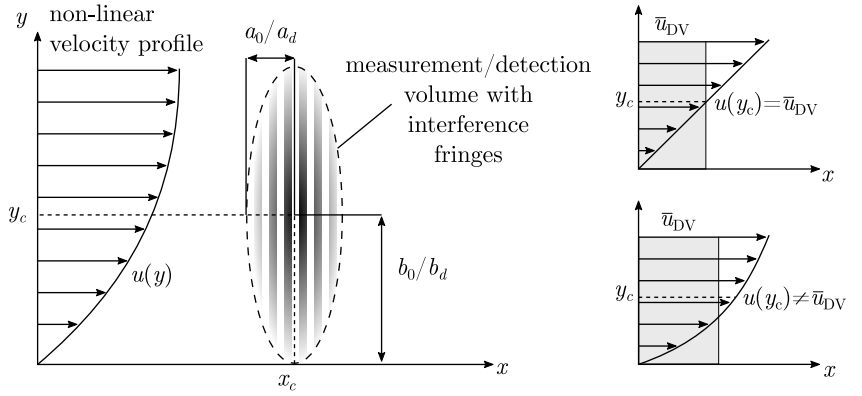

Figure 2.6: Left: Dimensions of the measurement/detection volume with a velocity gradient, adapted from Albrecht et al. (2013). Right: Depending on the shape of the velocity profile the value at the center point $u(y_c)$ may not correspond to the average value $\overline{u}_{\mathrm{DV}}$.

even though they are outside the e^{-2} volume. The size of the detection volume a_d, b_d, c_d can be determined experimentally in a laminar flow with a linear velocity gradient. Particles, which pass the DV at different locations, have different velocities due to the velocity gradient. This is detected as an apparent velocity fluctuation u'_{DV}

$$\overline{u'^2_{\mathrm{DV}}} = \frac{b_d^2}{4} \frac{\mathrm{d}\overline{u}\,(y)}{\mathrm{d}y}\bigg|^2_{y=y_c} , \tag{2.7}$$

where overbars denote temporal averaging and the index c refers to the center point of the DV. The velocity fluctuation $\overline{u'^2_{\mathrm{DV}}}$ can in turn be related to the detection volume semi-axis b_d, if the velocity gradient is measured or known. However, a linear gradient is necessary, which cannot be achieved in a fully developed laminar pipe flow. Thus, the detection volume size is estimated from the determination of the wall position, as later outlined in section 3.1.

Correction of Velocity Gradient Bias

The measurement of WSS always implies that a velocity gradient is present over the region of the detection volume, as shown in Figure 2.6. Thus, it may cover a relatively large area of this gradient. All computed LDV quantities are spatially averaged values over the detection volume and are assumed to be located in the center point of the detection volume (x_c, y_c). This assumption may be biased in the presence of a velocity gradient. Figure 2.6 shows typical velocity profiles and the spatial averaged values $\overline{u}_{\mathrm{DV}}$ in comparison to the center point values $u(y_c)$. If the gradient is known, the bias can be corrected in post-processing. It is assumed that the particles are monodispersed and the detection probability is unity for all particles passing through the center plane $x = x_c$ of the detection volume. Also the velocity gradient must only be present along y. The velocity gradient can then be expanded into a Taylor series up to second order. For a DV of elliptic shape the spatially averaged velocity $\overline{u}_{\mathrm{DV}}$ is

$$\overline{u}_{\mathrm{DV}} = \overline{u}\,(y_c) + \frac{b_d^2}{8} \frac{\mathrm{d}^2 \overline{u}\,(y)}{\mathrm{d}y^2}\bigg|_{y=y_c} . \tag{2.8}$$

This equation states that the computed average value $\overline{u}_{\mathrm{DV}}$ over the detection volume equals the velocity in the center of the DV biased by a factor proportional to the length of the detection volume along the gradient and the curvature of the velocity profile. Note that a linear gradient, for example in the viscous sublayer, does not lead to a systematic error. The velocity in the center point $\overline{u}(y_c)$ can be iteratively determined using Equation 2.8 and multiple measurement points along the gradient direction.

Tracer Particles

The seeding particles used in this study are titanium dioxide particles of $d_p \approx 1\,\mu\mathrm{m}$ diameter. Beside the optical properties like a high scattered light intensity, the particles need to follow the flow without significant slip. This is especially important for unsteady flows, where the difference of the fluid density ρ_f and the particle density ρ_p may lead to a slip motion. Allowing a relative slip s between the fluid and the particle velocity of 0.1 %, a critical frequency f_c can be determined up to which the particles follow the flow with

less than the specified slip, which is

$$f_c = \frac{\sqrt{(2s - s^2)}}{2\pi\tau_0\sqrt{(1-s)^2\left(1+\frac{1}{2}\frac{\rho_f}{\rho_p}\right)^2 - \left(\frac{3}{2}\frac{\rho_f}{\rho_p}\right)^2}} \approx 31\,\mathrm{kHz}\,, \tag{2.9}$$

for the current setup. In comparison to the human heart rate this is sufficiently large and the slip is negligible.
A second issue arises due to the high density of the titanium dioxide particles of $\rho_p \approx 3900\,\mathrm{kg/m^3}$. In laminar flows the tracer particles slowly settle. The settling velocity u_s can be calculated from the characteristic time τ_0 and the gravitational acceleration g to

$$u_s = \tau_0 g = \frac{d_p^2 \rho_p}{18\eta} g \approx 2.1\,\mu\mathrm{m/s}. \tag{2.10}$$

The flow velocity of a laminar steady pipe flow at $Re \approx 1300$ in the vicinity of the wall ($0\,\mathrm{mm} < y < 1\,\mathrm{mm}$) is $u \approx 0.01\,\mathrm{m/s}$ for the current setup. Downstream of the inlet pipe length of $l = 2.5\,\mathrm{m}$ the settling distance y_s of a titanium dioxide particle can be estimated to

$$y_s = \frac{u_s}{u} l \approx 531\,\mu\mathrm{m}, \tag{2.11}$$

which is significantly larger that the semi-axis b_0 of the measurement volume. In this region on the top of the pipe the seeding density is expected to be too low for measurements. To avoid low particle concentrations at the top and too high particle concentrations at the bottom of the pipe wall, LDV measurements are conducted from the side, as previously shown in Figure 2.5.

2.3.2 Magnetic Resonance Velocimetry

The MRI system used in this study is a 3 T whole-body scanner (Magnetom Prisma, Siemens Healthcare) located at the University Medical Center Freiburg. System specifications are given in Figure 2.7. For signal reception, a small flexible surface coil provided by the system vendor ('Flex Loop small') is tightly wrapped around the flow models. For the experiments no additional changes compared to standard medical diagnosis were made to either the hardware nor to the software.

Parameter	Value
Field strength	3 T
Bore diameter	600 mm
Gradient strength	80 mT/m
Gradient slew rate	200 T/(m s)
Field of view	500 mm

Figure 2.7: MRI scanner at the University Medical Center Freiburg, which was used in this study, including the corresponding specifications.

Analogue to the previous section about LDV, this section provides a short overview of relevant characteristics of the measurement technique, which are used in the later chapters. The following explanations are based upon the books of Haacke et al. (1999) and McRobbie et al. (2006), where also further information about MRI can be found.

Spins

MRI uses the spin, which is a quantum mechanical property similar to the angular momentum in classical mechanics, of protons and neutrons. Due to its rotation, the spins build up a magnetic dipole moment with a distinct magnitude and direction. The magnitude can only take discrete values, which are denoted as *spin-up* and *spin-down*. In atoms with an even number of protons and neutrons, two spins align anti-parallel and the magnetic dipoles cancel each other out. Therefore, only atoms with an odd number of protons and neutrons can be used. As MRI devices are designed for medical applications, they use only hydrogen atoms, which are the most frequent atoms in the human body and additionally have a net magnetic dipole.
When the spins are exposed to a strong external magnetic field with field vectors along the z-direction, they align with their magnetic orientation parallel or anti-parallel to this external field. The parallel orientation can be interpreted as the lower of two energy levels, thus the probability for spins to point into the direction of the external magnetic field is slightly higher. The

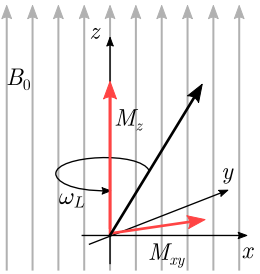

(a) Spin magnetization, which precess around the external magnetic field vector, decomposed into its axial and transversal magnetization.

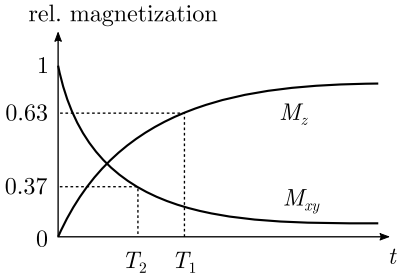

(b) Temporal evolution of the magnetization after the excitation. The transversal magnetization decreases significantly faster than the axial magnetization increases.

Figure 2.8: Visualization of the axial and transversal magnetization and its corresponding decay after excitation.

net amount of magnetization M_z generated by the alignment of the spins is small compared to the external magnetic field and cannot be measured.
A second consequence of the external magnetic field is that the spins start to precess with their magnetic axis around the external magnetic field vector. The precession frequency, also called Larmor frequency ω_L, is proportional to the local magnetic field strength B_0, and the substance-specific gyromagnetic ratio γ

$$\omega_L = \gamma B_0 \,. \tag{2.12}$$

Due to the precession, a single spin generates a rotating magnetic field in the transversal xy-plane, shown in Figure 2.8a. However, it is not possible to measure only one individual hydrogen atom but only macroscopic ensembles of spins. Although the precession frequency of all spins located in a magnetic field of equal strength is the same, their precession is not in phase with each other. The net transversal magnetization M_{xy} is zero.

Excitation and Relaxation

The behavior of the spins changes when a circularly polarized wave is applied to the field of view (FOV), which interferes with the spins. The excitation, also called radio-frequency (RF) pulse, is only possible when it has the same frequency as the Larmor frequency ω_L. After the application of the RF pulse, the spins are in phase and a net rotating transversal magnetization M_{xy} can be detected as an induced electric signal with a receiver coil. The signal starts to decay immediately after the RF-pulse ends. The spins then realign along the external field, which is called relaxation. The axial magnetization M_z increases, while the transversal magnetization M_{xy} decreases (Figure 2.8b). The transversal magnetization decays much faster than the axial magnetization builds up, since the spins interfere with each other and get out of phase. This de-phasing of the spins is called *spin-spin* relaxation. The characteristic time scale of these two phenomena are denoted with T_1 and T_2.

Spatial Encoding

The electromagnetic signal received during readout from the FOV does not yet include any information about the spatial distribution of the spins. As stated in Equation 2.12, the Larmor frequency ω_L is proportional to the local magnetic field B_0. Spatial encoding of the spins is achieved by altering the external magnetic field with additional magnetic gradients $G_s(\vec{x}, t)$ in each direction. This influences the frequency

$$\omega_L(\vec{x}, t) = \gamma \left(B_0 + G_s(\vec{x}, t) \cdot \vec{x}\right) , \tag{2.13}$$

as well as the phase

$$\Phi(\vec{x}, t) = \gamma \int_0^{\mathrm{TE}} G_s\left(\vec{x}, t\right) \cdot \vec{x} \, \mathrm{d}t \, , \tag{2.14}$$

of each spin depending on the gradient strength G_s and the time between excitation and readout, the so-called echo time TE.
In a first step, the so-called *slice selection* gradient is applied in x-direction during the RF pulse excitation. The spins along the gradient direction precess at different frequencies, thus the resonance condition is only fulfilled within a thin slice. Only spins located at this specific position in x-direction are

excited. In a second step, the *phase encoding* gradient is applied for a short time in y-direction. During this time the precession frequency is linearly altered in this direction. After the phase encoding gradient is switched off, a resulting phase difference (Equation 2.14) proportional to the y-location remains. In a last step, the *frequency encoding* gradient in z-direction is applied during readout, changing the Larmor frequency proportional to the location in z-direction (Equation 2.13). For 3D imaging the slice selection gradient can be replaced with an additional frequency encoding gradient, which improves the spatial resolution and the signal quality.
Each location in space can now be associated with a distinct phase and frequency included in the received signal. However, it is not possible to reconstruct the image from only one electromagnetic signal. The sequence is repeated with varying phase encoding gradients with the number of image lines in the phase encoding direction. Each received signal is Fourier transformed and stored as a complex value containing a magnitude and phase in the so-called k-space. An inverse Fourier transform of the complex k-space yields two images, which are the magnitude and the phase image. The magnitude is a measure of the spin density, while the phase image does not include a specific information up to now.

Velocity Encoding

The phase of the spins can be altered to encode the velocity information. The application of a bipolar gradient, termed velocity encoding gradient G_v, results in a net phase of moving spins, while stationary spins do not gain additional phase (Figure 2.9). The total phase Φ of a spin consists of

$$\Phi(\vec{x},t) = \Phi_0 + \gamma x \underbrace{\int_0^{\mathrm{TE}} G_v \,\mathrm{d}t}_{M_0=0} + \gamma u \underbrace{\int_0^{\mathrm{TE}} G_v t \,\mathrm{d}t}_{M_1} + \gamma \frac{1}{2} a \underbrace{\int_0^{\mathrm{TE}} G_v t^2 \,\mathrm{d}t}_{M_2 \approx 0} + \ldots . \quad (2.15)$$

The gradient moments M_n are proportional to the position x, velocity u, acceleration a and higher order moments of the spin trajectory. Φ_0 is the phase that includes already present phase information not related to the velocity encoding like a background phase or eventually systematic errors from e.g. eddy currents. Acceleration and higher order terms can in general

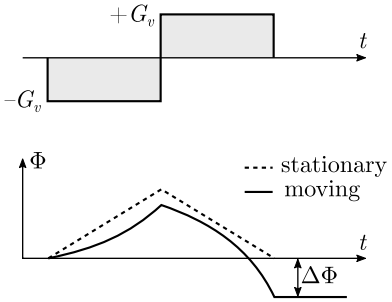

Figure 2.9: Bipolar gradient for the encoding of velocity, adapted from Haacke et al. (1999). While for stationary spins the net amount of phase is zero, the moving spins acquire a phase, which is linearly proportional to the velocity.

be neglected. Φ_0 can be removed by subtracting a reference scan, also called *flow-compensated* scan, for which also the phase from moving spins is $M_1 = 0$. A subtraction of the *flow-compensated* scan from the first *flow-encoding* scan yields a phase difference $\Delta\Phi$, which is linear proportional to the velocity

$$\Delta\Phi = \gamma u M_1 \,. \tag{2.16}$$

This can be rearranged with the definition of the velocity encoding value *venc*

$$venc = \frac{\pi}{\gamma \mathrm{M}_1} \,, \tag{2.17}$$

to

$$u = \frac{venc}{\pi} \Delta\Phi \,. \tag{2.18}$$

However, a systematic error from eddy currents induced from the flow field may be present in Φ_0 and therefore also in $\Delta\Phi$. This systematic error can be removed with an additional reference measurement with stationary flow (pumps turned off).

Measurement Uncertainty

Stochastic errors in the MRV acquisition may originate from internal and external sources, also termed intrinsic and extrinsic noise (Gudbjartsson & Patz, 1995). Intrinsic sources of errors are associated with the electronics of the MRI scanner and the signal processing, which for example depend on the Brownian motion of electrons. Extrinsic uncertainties are mainly based on the stochastic motion of the spins, for example due to turbulent flow. Depending on the magnitude or phase image, the noise is expressed in two different terms, which should be introduced in this section. The following paragraphs are mainly based on the work of Bruschewski et al. (2016).

Signal-to-noise ratio (SNR): The signal-to-noise ratio is a measure of the quality of a measurement and describes the relation of the undisturbed measurement value to the noise (Tropea & Yarin, 2007). In a MRI acquisition the SNR is used for the assessment of the magnitude image and calculated with

$$\mathrm{SNR} = \frac{A}{\sigma_{\mathrm{mag}}}\,, \tag{2.19}$$

where A is the noise-free magnitude in the region of interest (ROI) and σ_{mag} is the standard deviation of the noise. There exist numerous methods in literature to practically determine the SNR from a MRI image. A good overview can be found in Bruschewski et al. (2016). Two approaches are used in this thesis.

The first method, which is described in Constantinides et al. (1997), is used when only a single acquisition is available. Manual segmentation of the MRI image is required. A region in the artifact-free background and a second region in the ROI have to be defined. σ_{mag} can then be calculated from the region in the artifact-free background with

$$\sigma_{\mathrm{mag}} = \sqrt{\frac{\langle \mathbf{M}^2 \rangle}{2N_c}}\,, \tag{2.20}$$

where $\mathbf{M}$ contains all values of the magnitude in this region, N_c is the number of receiver coils and $\langle\ \rangle$ denotes the arithmetic mean. The signal value A is determined from the ROI with

$$A = \sqrt{\langle \mathbf{M}^2 \rangle - 2N_c\sigma_{\mathrm{mag}}^2}\,. \tag{2.21}$$

Then, the SNR can be calculated with Equation 2.19.
The second method, described in NEMA (2014), is used when two identical acquisitions are available. This method also requires a segmentation of the image, but only in the ROI. A careful choice of the artifact-free background is not necessary. First, the magnitude value in the image is calculated in one of the two images

$$A = \langle \mathbf{M} \rangle \,. \tag{2.22}$$

In the same region the standard deviation of the magnitude is calculated from the difference of both measurements according to

$$\sigma_{\mathrm{mag}} = \sqrt{\frac{\mathrm{var}(\mathbf{M}_1 - \mathbf{M}_2)}{2}} \,, \tag{2.23}$$

where var( ) is the variance. Due to the subtraction the noise increases, which would lead to a higher σ_{mag} and thus an underprediction of the SNR. The factor $\sqrt{2}$ accounts for this uncorrelated noise in both images.
According to (McRobbie et al., 2006) the SNR is proportional to

- The voxel size, respectively the voxel volume V_{vox}: SNR $\propto V_{\mathrm{vox}}$.
- The number of acquisitions N_{acq}: SNR $\propto \sqrt{N_{\mathrm{acq}}}$.
- The magnetic field strength B_0: SNR $\propto B_0$.
- Several other factors like the receiver bandwidth and the scanner hardware.

Velocity uncertainty: For the phase image, respectively the velocity, it is more appropriate to calculate a standard deviation. It can be shown that the uncertainty of the phase σ_Φ is approximately the inverse of the SNR (Haacke et al., 1999)

$$\sigma_\Phi \approx \frac{1}{\mathrm{SNR}} \,. \tag{2.24}$$

For SNR > 8 this approximation is reasonable with an error less than 1 %. With the relation between velocity and phase from Equation 2.18 and the SNR from Equation 2.19 this can be rearranged to yield the uncertainty of the velocity (Bruschewski et al., 2016)

$$\sigma_u = c_\Delta \frac{venc}{\pi} \frac{\sigma_{\mathrm{mag}}}{A} \,. \tag{2.25}$$

The factor c_Δ results from the phase difference measurement. Since the velocity is calculated from the phase difference of a *flow encoded* and a *flow compensated* measurement, the increased noise has to be considered, similar as in Equation 2.23. For an one component velocity measurement, also termed two-point measurement, $c_\Delta = \sqrt{2}$. Analogous as for the SNR, there exist two methods for the calculation of σ_u.
For the single-acquisition method, the SNR is determined with Equation 2.20 and Equation 2.21 and inserted into the velocity uncertainty of Equation 2.25. For the dual-acquisition method, Equation 2.23 can be equivalently rewritten to determine the velocity uncertainty directly from two phase images

$$\sigma_u = \frac{venc}{\pi} \sqrt{\frac{\mathrm{var}(\Delta\mathbf{\Phi}_1 - \Delta\mathbf{\Phi}_2)}{2}}\,, \tag{2.26}$$

where $\Delta\mathbf{\Phi}$ contains all phase differences in the respective ROI (Bruschewski et al., 2016).
As shown by Bruschewski et al. (2016), the single-acquisition method may be biased in the case of turbulent flows or when other systematic sources of errors are present in the image. Those artifacts may then considerably influence the SNR calculation. Therefore it is strongly recommended to use the second method, which uses two consecutive measurements. However, this is sometimes not possible, especially when the measurement time is limited.
The velocity uncertainty σ_u is inversely proportional to the parameters described for the SNR, and as seen from Equation 2.26 additionally linearly proportional to the *venc*. Thus, the *venc* is an important parameter to significantly reduce the noise. It should therefore be chosen as low as possible. However, special care must be taken to properly treat phase wraps when setting the *venc* too low.

3 Flow Through Pipes

In this chapter rather simple flows through straight pipes are investigated. In a first step, steady pipe flows are discussed in **section 3.1**. The results and methods are then transferred to pulsating pipe flows in **section 3.2**.

3.1 Steady Pipe Flows

In this section methods to accurately measure the WSS with LDV are developed, while MRV measurements of the same flows are conducted in parallel. As outlined in the previous chapter, the conditions in the aorta are close to transitional. Therefore, a laminar and a turbulent flow close to the transition regime are chosen for the generic experiments. The maximum Reynolds number of the laminar pipe flow is restricted due to the inflow length of the pipe. The necessary inlet length can be estimated according to Durst et al. (2005) with

$$\frac{l}{d} = \left[(0.619)^{1.6} + (0.0567Re)^{1.6}\right]^{1/1.6} , \tag{3.1}$$

which is iteratively solved to yield the maximum Reynolds number. With the current setup of $l/d \approx 77$ a Reynolds number of $Re_{\max} \approx 1356$ can be achieved.

For the turbulent pipe flow the Reynolds number is chosen at the lower bound of turbulent conditions. The exact value of the Reynolds number for transition depends strongly on the setup and the sources of disturbance in the flow. In the present case a flow with $Re = 5300$ is used because of an existing direct numerical simulation (DNS) from El Khoury et al. (2013) at this Reynolds number.

The experimental results of this chapter can be compared to the well-known Hagen-Poiseuille solution (Brenn, 2016)

$$u(r) = \frac{2\dot{V}}{\pi R^2}\left(1 - \frac{r^2}{R^2}\right) \quad \text{and} \quad \tau_w = \eta\frac{4\dot{V}}{\pi R^3} , \tag{3.2}$$

Table 3.1: Flow conditions of the steady pipe flows and corresponding MRV measurement parameters.

Parameter	Case 1	Case 2
Flow	laminar	turbulent
Re (-)	1310	5277
$\dot{V}$ (L/min)	1.56	6.14
Sequence type	2D1C	2D1C
Voxel size (mm)	$0.50 \times 0.50 \times 3.0$	$0.30 \times 0.30 \times 3.0$
$venc$ (m/s)	0.01	0.25
TE (ms)	13.7	5.0
TR (ms)	33.4	17.2
FOV (voxels)	192×192	320×320
N_{acq} (-)	4	15

in the case of the laminar flow, and to the DNS data in the case of the turbulent flow. MRV and flow parameters for this chapter are given in Table 3.1.

3.1.1 Preliminary Tests: Influence of Temperature

Inspection of the velocity profile reveals that in most cases the flow field is not symmetric for the laminar case. Exemplary MRV measurements are shown in Figure 3.1. The location of maximum velocity is shifted approximately $\Delta y \approx 2.3\,\mathrm{mm}$ towards the bottom of the pipe. However, the turbulent flow does not exhibit such behavior. This effect occurs in various preliminary tests with different degrees of asymmetry, but the shift is only present in laminar flows and only in the vertical direction.
It is presumed that gravitational forces, respectively buoyancy, may be responsible for the asymmetry. Buoyancy may occur due to temperature differences in the flow field. As shown by Kyomen et al. (1996), a temperature difference between fluid and room temperature $\Delta T = T_{\mathrm{fluid}} - T_{\mathrm{ambient}}$ may introduce secondary flow motion in horizontally orientated pipes with laminar flow conditions. In this section, the degree to which a temperature difference ΔT will potentially influence the velocity field is examined and a tolerable ΔT for the following study is derived.

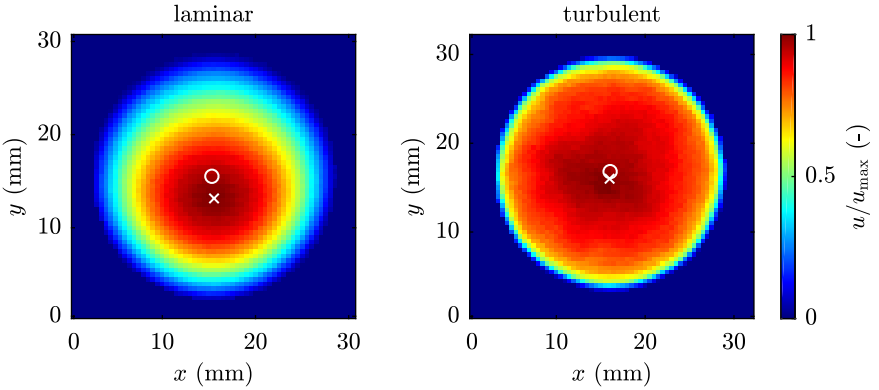

Figure 3.1: MRV measurement of a laminar flow at $Re \approx 1300$ (left) and a turbulent flow at $Re \approx 5300$ (right). The symbols represent the geometric pipe center (◯) and the position of maximum velocity (×).

When a temperature difference between a fluid and the wall (ambient) is present, heat transfer takes place at the boundary, which leads to a change in the density of the fluid. Density gradients in turn cause buoyancy forces and thus natural convection. Depending on the sign of the temperature difference an upward or downward facing flow develops in the vicinity of the wall, shown in Figure 3.2. At the stagnation point of the two impinging flows the fluid circulates to the opposite side through the center of the pipe. As a consequence, two counter rotating vortices develop. The velocity field introduced by natural convection is superimposed on the pressure driven, axial pipe flow. The velocity component in vertical direction in the center of the pipe influences the axial velocity component and shifts the position of maximum velocity out of the center; hence, the velocity profile will be asymmetric. This asymmetry will in turn affect the magnitude and spatial distribution of the wall shear stress. In addition, the influence on the flow through complex geometries will be even stronger, since small upstream disturbances may have a significant influence on possible separation and reattachment points downstream. This effect is assumed to be most prominent in laminar flows, since in turbulent flows the mixing process usually dominates.
According to Kyomen et al. (1996), the degree of asymmetry of the velocity profile is a function of the magnitude of the secondary flow motion as well as

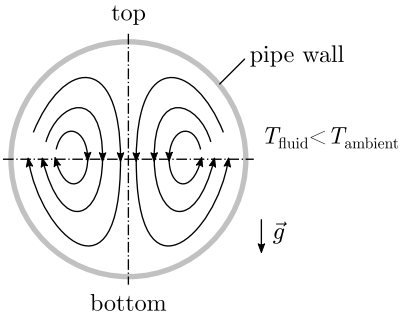

Figure 3.2: Schematic representation of the streamlines due to natural convection in the cross sectional view of a pipe, shown for the case when the ambient temperature is above the mean fluid temperature.

the pressure driven flow. The first one depends on the heat transfer, and thus on the Rayleigh number Ra, which is a measure of buoyancy driven forces. The latter is proportional to the Reynolds number Re. The asymmetry itself is a function of the product of both, thus $ReRa$.
To confirm that the initial assumption of a temperature influence is present, LDV measurements of the axial velocity are conducted within the horizontally orientated pipe at laminar ($1291 < Re < 1512$) and turbulent ($5068 < Re < 6863$) flow conditions. After each measurement the temperature is gradually increased, while the volume flow rate is kept constant over each series of measurements. The fluid temperature is measured at the inlet of the pipe. The room temperature is acquired approximately 0.1 m above the pipe. All sensors are identically constructed thermocouples type K.
Figure 3.3a shows the normalized laminar velocity profiles for various temperature differences ΔT between fluid and ambient. The top of the pipe is on the left, while the bottom is on the right. The black dots represent LDV measurement points, while the lines are spline interpolations. The colors indicate whether the fluid temperature is above (red) or below (blue) the ambient temperature. The analytical Hagen-Poiseuille profile is shown for reference. Even though ΔT is only in the range $-2.4\,°\text{C} < \Delta\text{T} < 1.7\,°\text{C}$, the degree of asymmetry is substantial. In accordance with theory, the position of maximum velocity is monotonically dependent on the sign and magnitude of the temperature difference.

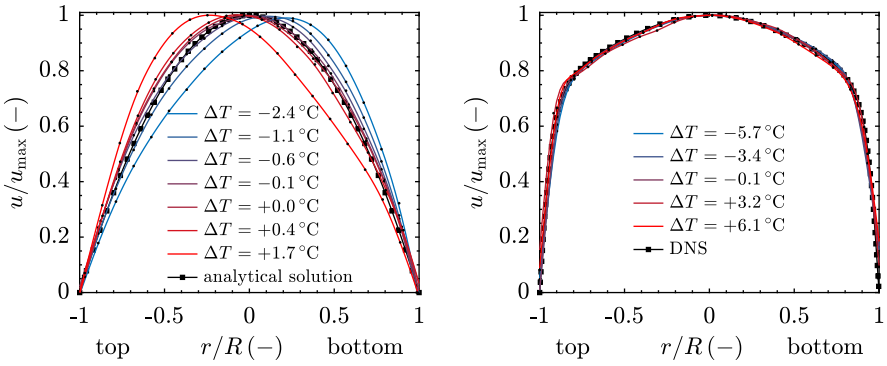

(a) Laminar case. **(b)** Turbulent case.

Figure 3.3: Velocity profiles for different temperature differences ΔT between fluid and ambient in comparison to the analytical solution respectively the DNS data. The top of the pipe is on the left, bottom at the right. Black dots represent LDV measurement points, lines are spline interpolations. Colors indicate whether the fluid temperature is above (red) or below (blue) the ambient temperature.

Velocity profiles for the turbulent case are shown in Figure 3.3b. Although ΔT is significantly higher than in the laminar flow case, no asymmetry is noticeable. The solution of the DNS from El Khoury et al. (2013) is shown for reference.

The question that should be answered is, which ΔT is acceptable in order to guarantee a certain symmetry? The degree of symmetry is defined as the deviation of the position of maximum velocity $r_{u_{\max}}$ from the center $r = 0$, normalized with the pipe diameter d. For the present work an acceptable asymmetry of 2 %, corresponding to approximately $r_{u_{\max}} \approx 0.5\,\mathrm{mm}$ is proposed. This is a typical spatial resolution of MRI measurements and seems therefore sufficiently accurate.

Figure 3.4a shows the dependence of the temperature difference ΔT on the asymmetry $r_{u_{\max}}/d$ for the laminar flow. To achieve an asymmetry lower than 2 %, ΔT must not exceed $\pm 0.3\,°C$. Note that the relation in Figure 3.4a is nonlinear, since the volume flow rate is kept constant over all measurements and due to the change in temperature the Reynolds number also changes. $ReRa$, the measure of asymmetry, is therefore higher for positive ΔT. Figure 3.4b shows the results of the turbulent flow. As already concluded from

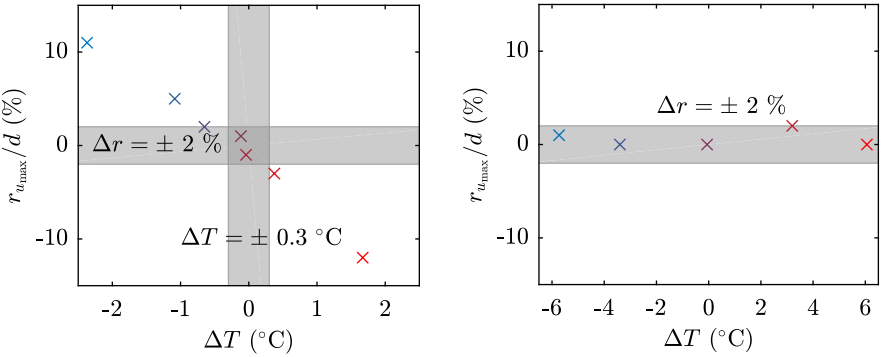

(a) Laminar case. **(b)** Turbulent case.

Figure 3.4: Position of maximum velocity, normalized with the pipe radius, in relation to the temperature difference. The vertical shaded area indicate the necessary temperature stability to achieve the specified maximum deviation from symmetry.

the velocity profiles, no dependence on ΔT is found.
For all experiments conducted within this study the asymmetry is minimized by adjusting the fluid temperature to the ambient temperature. The temperature difference ΔT is measured at the entrance of the pipe, since this point is located furthest away from the magnetic isocenter. In addition, a thermal insulation of 20 mm thick rubber is used, which is wrapped around the entire pipe.

3.1.2 Wall Shear Stress Measurements

MRV

For a better comparison with the LDV reference measurements and because all experiments are conducted within axisymmetric pipes, a mean velocity profile can be obtained by azimuthal averaging the MRV data. First, the magnitude is used to segment the signals of the flow model from surrounding noise. If the magnitude is less than a certain threshold, the corresponding voxel in the phase image is masked out. The threshold is calculated based on a method proposed by Otsu (1979), using the histogram of the magnitude, which is shown in Figure 3.5a. The signal of the flow model and the noise

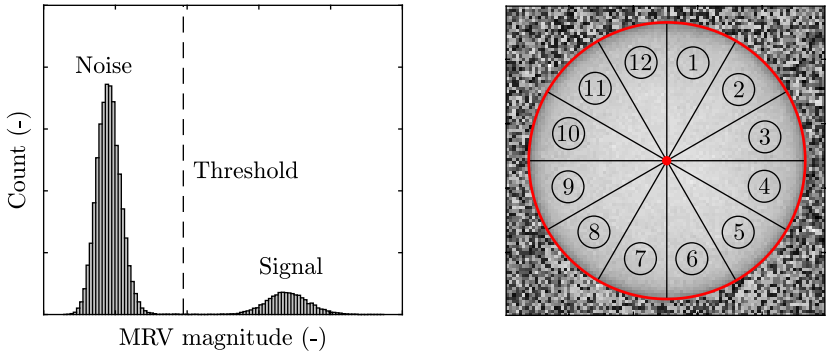

(a) Histogram of the magnitude including the segmentation threshold.

(b) Velocity field of the pipe, divided into 12 equally spaced segments.

Figure 3.5: Segmentation and spatial averaging of the MRV data. Adapted from Bauer et al. (2019).

can be distinguished as two separate distributions in the histogram. After the segmentation the midpoint of the circular shaped pipe is detected using a Matlab® code employing the approach of Atherton & Kerbyson (1999). Starting from this point, the corresponding radius of each voxel can be determined. The mean velocity profile is obtained by grouping the voxels into bins along the radius with a bin width of the same size as the initial voxel size.

To avoid conflicts with potential asymmetric flow conditions, i.e. from temperature differences, and to detect those visually, the flow field is divided into 12 equally spaced segments around the circumference, shown in Figure 3.5b. This method is common for *in vivo* measurements, where the flow is typically not symmetric (Frydrychowicz et al., 2009; Harloff et al., 2010, 2013). For each segment the velocity and later on the WSS is calculated separately.

For the calculation of the wall shear stress, the position of the wall needs to be determined exactly. In the MRV data, the position of the wall is determined from the detected midpoint and the known pipe diameter, where the no-slip condition is assumed. The WSS is calculated with a linear gradient between the wall and the second measurement point (bin) inside the flow field. The first measurement point may be subject to systematic errors caused by partial volume effects and is therefore not used.

For the laminar und turbulent flows the SNR and velocity uncertainty is

calculated from the dual-acquisition method described in section 2.3.2. The SNR for the laminar flow is SNR = 15 and for the turbulent flow SNR = 21. The velocity uncertainty, normalized with the maximum velocity in each ROI, is $\sigma_u = 0.2\,\%$ and $\sigma_u = 4\,\%$ respectively. Note that the uncertainty is significantly reduced due to multiple acquisitions, especially in the turbulent case. Although the SNR is higher for the turbulent case, the relative velocity uncertainty is also higher compared to the laminar case. This is due to the turbulent velocity fluctuations.

LDV

The determination of the wall position from LDV data is more difficult. The method is discussed with the data obtained from the turbulent case.
In a first step, the detection volume is positioned manually at the inner wall, which can be achieved with an accuracy of approximately $\pm 0.3\,\mathrm{mm}$. The validation settings of the laser Doppler signal processor are adjusted so that no signal is detected when the detection volume is fully embedded in the wall. In a second step, the histogram of the LDV data is used to initially estimate the wall position by taking short 'referencing measurements', while traversing the detection volume from the flow field into the wall. This is shown in Figure 3.6 for different positions with a schematic representation of the DV position. When the DV is completely located in the flow field (Position 3), there is a gap in the histogram between the velocity distribution and the point of origin. The width of the velocity distribution results from the velocity gradient across the DV. As soon as the DV reaches the wall (Position 2), the gap closes. When the DV is partially embedded in the wall (Position 1), the histogram is cut off at the lower end and the distribution narrows because the transparent wall does not give a signal. The measurement position, at which the lower end of the histogram is located at $u = 0\,\mathrm{m/s}$ is approximately the position where the DV is just completely located outside the wall.
In the last step the method proposed by Durst et al. (1988) is used. A velocity profile is acquired in the region where the wall was estimated in the previous step, shown at the bottom of Figure 3.6. When the DV is moved into the wall, the actual center of measurement does not coincide with the geometric center of the measurement volume. At the wall, where the velocity should be zero (Position 1), a velocity can still be detected from the part

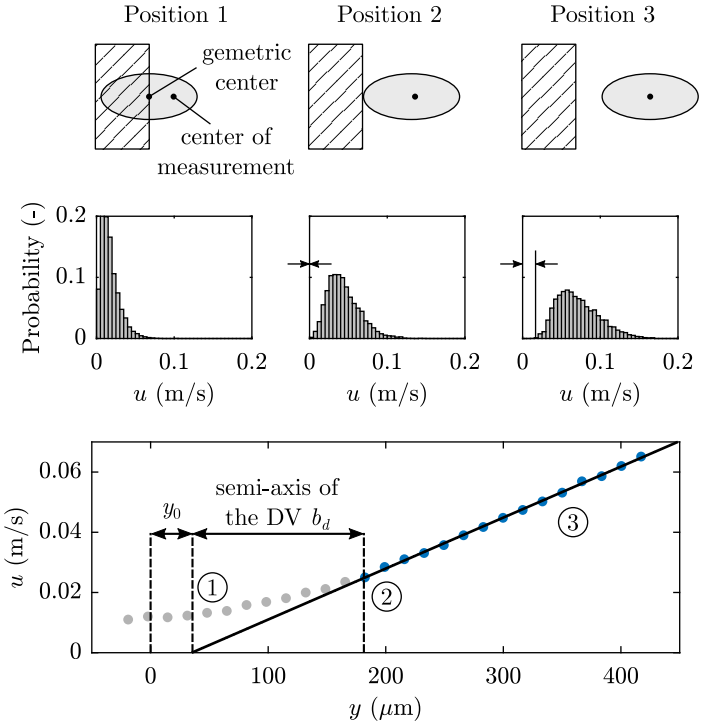

Figure 3.6: Determination of the wall position shown for the turbulent case ($Re = 5277$). Top: Schematic illustration of the DV relative to the wall, adapted from Durst et al. (1988). Middle: Histogram of the velocity at the respective position. Bottom: Final determination of the wall with the velocity profile.

of the detection volume, which is located in the flow field. The velocity is systematically overestimated. The location of the wall is determined with a linear fit through the measurement points not embedded in the wall. The position of the initial guess y_0 can be corrected in a post-processing step. The semi-axis of the detection volume b_d is estimated to $b_d \approx 150\,\mu\text{m}$, which is in very good agreement with the theoretical size of the measurement volume of $b_0 = 164\,\mu\text{m}$.

Afterwards, the wall shear stress is calculated with a linear gradient between the wall, where the no-slip condition is assumed, and several measurement points inside the fluid.

Results

Results of the WSS calculations from LDV and MRV are given in Table 3.2 together with the reference values. For both flows the laser Doppler can capture the wall shear stress with the methods proposed in this chapter with a high accuracy and only with a slight underestimation of $\Delta\tau_w = 1.4\,\%$ (laminar) and $\Delta\tau_w = 0.5\,\%$ (turbulent). The MRV yields very good results for the laminar case, only slightly underestimating the wall shear stress by about $\Delta\tau_w = 0.8\,\%$. In the turbulent case a more pronounced deviation of $\Delta\tau_w = 9\,\%$ is present. Overall, the LDV results yield excellent agreement with the reference values. A possible explanation of the discrepancy between MRV and the reference value for the turbulent case is given below.

For turbulent flows there exists a more or less universal shape of the velocity profile when non-dimensionalized. In a small region in the vicinity of the wall, where viscous forces are dominant, the velocity profile follows a linear relationship $u^+ = y^+$, where y^+ is denoted as the dimensionless wall coordinate and u^+ as the dimensionless velocity. These are given by the definitions $u^+ = u/u_\tau$ and $y^+ = yu_\tau/\nu$ with the wall shear velocity u_τ defined as $u_\tau = \sqrt{\tau_w/\rho}$. This relation is valid for $y^+ < 5$. For $y^+ > 30$, a logarithmic law in the form of $u^+ = 1/\kappa \ln(y^+) + B$ applies, while the constants κ and B may slightly vary for different types of flows (Rodríguez-López et al., 2015). In the intermediate region ($5 < y^+ < 30$), a buffer layer smoothly connects both regions.

For the turbulent case the WSS reference value from Table 3.2 is used to obtain the wall shear velocity u_τ and subsequently the wall coordinates u^+ and y^+. The velocity profiles from the LDV and MRV measurements are

Table 3.2: Results of the wall shear stress τ_w and the relative difference to the reference value $\Delta\tau_w$. For the laminar case the reference is the Hagen-Poiseuille solution from Equation 3.2; for the turbulent case the DNS data is used.

	Laminar case		Turbulent case	
	τ_w ($10^{-3}\,\mathrm{N/m^2}$)	$\Delta\tau_w$ (%)	τ_w ($10^{-3}\,\mathrm{N/m^2}$)	$\Delta\tau_w$ (%)
Reference	14.9	–	175.6	–
LDV	14.7	-1.4	174.6	-0.5
MRV	14.8	-0.8	159.7	-9.0

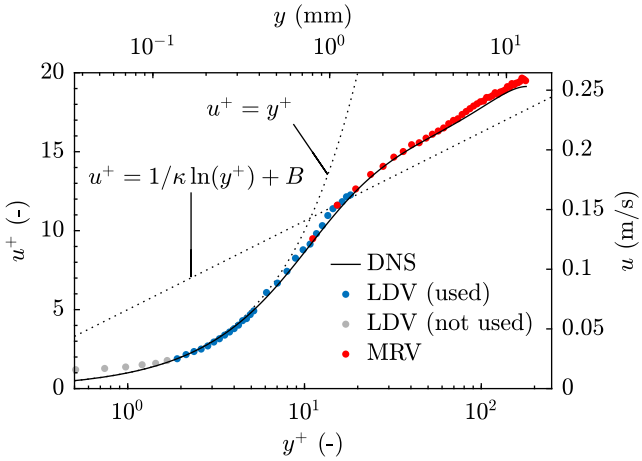

Figure 3.7: LDV and MRV data of the turbulent flow, shown in dimensionless coordinates (lower and left axis) and dimensional coordinates (upper and right axis). Gray displayed LDV values are located within the wall. Note that for the determination of the WSS with LDV, the velocity profile was acquired only in the region near the wall.

shown in Figure 3.7 together with the DNS and the linear and logarithmic law. The linear region $y^+ < 5$ equals approximately $y < 0.4\,\text{mm}$ in dimensional coordinates. The LDV measurement point next to the wall is located within this viscous sublayer. A linear gradient therefore yields an accurate estimate of the WSS, only biased by stochastic measurement errors. On the other hand, the first MRV measurement point is located at $y^+ \approx 10$, which corresponds to $y \approx 0.8\,\text{mm}$, which is inside the buffer region. A linear gradient for the determination of the WSS thus results in a systematic underestimation.

3.1.3 Summary: Steady Pipe Flows

As discussed in section 3.1.1, a strong dependence of the velocity field on even small temperature gradients is found for steady laminar pipe flows. In steady turbulent pipe flows such behavior could not be detected, presumably caused by the enhanced mixing. In order to reduce the asymmetry in the flow, a thermal insulation of the setup is used and the inner and outer temperatures are closely matched.
For the analysis of the MRV data, an azimuthal averaging process is proposed in section 3.1.2. However, it is not the purpose to develop a new evaluation method. Rather this method should be used for a fast and easy comparison of MRV and LDV data regarding velocity profiles and WSS. This should ensure that the flow conditions in both experimental investigations are similar and thus a comparison is legitimate.
The results of the WSS measurements from LDV showed very good agreement with the expected values, yielding a deviation of only 0.5 - 1.4 %. Thus, the present laser Doppler system seems suitable to conduct the reference measurements for the present study. On the other hand, the WSS results from MRV differed up to 9 % for turbulent flows.
In comparison to the laminar flow, the turbulent case offers several benefits, which makes it an advantageous scenario for the initial determination of the wall position with LDV:

- The first few LDV measurement points are located in the viscous sublayer. A linear gradient fit should therefore be accurate to yield the wall position.
- For a linear velocity gradient no systematic errors due to the finite size of the DV is expected. A velocity gradient correction, as introduced in section 2.3.1, can therefore be omitted.
- No asymmetry from temperature differences is expected.
- The turbulent mixing provides an additional benefit of a higher data rate due to more seeding particles close to the wall, which can effectively reduce the measurement time.

Therefore, this method will be used in combination with a turbulent flow in the following chapters.

3.2 Pulsating Pipe Flows

Investigations are extended to time dependent flows and phase-averaged measurements in this chapter. In a first section, additional background material is provided, which is necessary for the understanding of such flows. Afterwards, two categories of pulsating pipe flows are analyzed. The first one corresponds to laminar flows; the second one to transitional flows. Parts of this chapter have already been published in Bauer et al. (2019).

3.2.1 Background Material

Definitions

A pipe flow with a sinusoidal varying volume flow rate $\dot{V}(t)$, respectively Reynolds number $Re(t)$, and zero time-averaged mean flow rate is termed *oscillating* pipe flow. It can be described with the amplitude of the oscillating Reynolds number Re_{os} and a frequency ω. In contrast to an oscillating pipe flow, a *pulsating* pipe flow does have a net flow rate. In other words, a pulsating pipe flow is the superposition of a steady pipe flow and an oscillating pipe flow. The time averaged Reynolds number of the sinusoidal pulsating pipe flow equals the Reynolds number of the steady flow, thus it is termed Re_{ta}. For a complete description of a pulsating pipe flow three dimensionless variables Re_{ta}, Re_{os} and Wo are necessary, which are related through

$$Re(t) = Re_{\mathrm{ta}} + Re_{\mathrm{os}} \sin(\omega t) \quad \text{and} \quad Wo = R\sqrt{\frac{\omega}{\nu}}\,. \tag{3.3}$$

Sinusoidal pulsating pipe flows have been extensively studied in literature. Overviews can be found in Gündogdu & Çarpinlioğlu (1999a,b) and Çarpinlioğlu & Gündogdu (2001).
A combination of different sinusoidal pulsating or oscillating pipe flows is also possible. Depending on Re_{ta}, Re_{os} and Wo for each flow, the resulting flow waveform is in general not sinusoidal, but periodic and arbitrary in shape. With this method, realistic volume flow rate found in the aorta can be achieved. In this study, pulsating pipe flows with non-sinusoidal shapes are therefore called *physiological* pulsating pipe flows.

Analytical Laminar Solution

Under certain conditions there exists an analytical solution of the velocity field of a pipe flow with time varying volume flow rate $\dot{V}(t)$. However, the general solution from literature does not fulfill the needs of this thesis. For example, it does not yield the wall shear stress. Additionally, those solutions are based on a known pressure gradient $\partial p/\partial x$, which is not accessible for the present experimental setup. It is considerably easier to measure the volume flow rate $\dot{V}(t)$ with a flow meter. With the knowledge of $\dot{V}(t)$ the pressure gradient can then be replaced. As this solution is uncommon and cannot be found in literature, it is derived in the following section, and based upon the work of Lambossy (1952); Womersley (1955); Durst et al. (1996a) and Brenn (2016). The following assumptions are necessary to obtain a solution:

- The fluid is homogeneous, incompressible and Newtonian.
- The flow is laminar, symmetrically in circumferential direction and only one velocity component along the pipe axis exists.
- The flow is fully developed and the no-slip condition applies at the wall.
- The walls are rigid, smooth and the cross section is circular.
- Body forces can be neglected.
- The pressure gradient is periodic in time (not necessarily harmonic).
- For simplification no phase difference between the pressure gradient and the volume flow rate is assumed. This is obviously not the case in reality, but does not affect the solution except for a phase shift. Since the information about pressure is neither available nor of interest for the current experiments, this assumption does not constitute an impediment. However, it considerably simplifies the derivation of the solution.

The continuity equation simplifies due to the assumption of homogeneous density and velocity in axial direction to

$$\frac{\partial u}{\partial x} = 0\,. \tag{3.4}$$

The Navier-Stokes equation simplifies due to those assumptions to

$$\rho \frac{\partial u}{\partial t} = \frac{\partial p}{\partial x} + \eta \left(\frac{\partial^2 u}{\partial r^2} + \frac{1}{r} \frac{\partial u}{\partial r} \right) . \tag{3.5}$$

The pressure gradient along the pipe axis $\frac{\partial p}{\partial x}$ can be decomposed into its N harmonic components

$$\frac{\partial p}{\partial x}(t) = P_0 + \sum_{n=1}^{N} P_n e^{i\omega n t} , \tag{3.6}$$

where P_0 and P_n represent the constant and time dependent amplitudes of the pressure gradient of the respective n-th harmonic excitation. The fundamental frequency is denoted by ω.
Solving the Navier-Stokes equation together with the pressure gradient and the continuity equation gives the well-known solution of the velocity field $u(r,t)$ commonly found in literature, e.g. in Womersley (1955) and Brenn (2016)

$$u(r,t) = -\frac{P_0}{4\eta} \left(R^2 - r^2 \right) + \sum_{n=1}^{N} \frac{i P_n}{\rho \omega n} \left[1 - \frac{J_0 \left(\Lambda_n \frac{r}{R} \right)}{J_0 \left(\Lambda_n \right)} \right] e^{i\omega n t} , \tag{3.7}$$

with $\Lambda_n = Wo_n i^{3/2}$, the Womersley number $Wo_n = R\sqrt{\frac{\omega n}{\nu}}$, the pipe radius R and the Bessel function of the first kind, zeroth order J_0.
This solution contains the unknown coefficients P_0 and P_n of the pressure term, which are not accessible. In the following paragraphs, a solution is shown how the coefficients P_0 and P_n can be replaced with the volume flow rate $\dot{V}(t)$.
$\dot{V}(t)$ can be represented as the integral of the velocity field $u(r,t)$ over the cross section of the pipe as

$$\dot{V}(t) = \int_0^R \int_0^{2\pi} u(r,t) r \, \mathrm{d}\varphi \, \mathrm{d}r . \tag{3.8}$$

The time dependent volume flow rate $\dot{V}(t)$ can be decomposed into its N harmonic parts in the same manner as the pressure gradient

$$\dot{V}(t) = \dot{V}_0 + \sum_{n=1}^{N} \dot{V}_n e^{i(\omega n t + \Delta\varphi_n)}\,, \tag{3.9}$$

where $\Delta\varphi_n$ represents the phase difference of each mode between pressure and volume flow rate. As pointed out earlier, this phase difference can be neglected ($\Delta\varphi_n = 0$) and thus

$$\dot{V}(t) = \dot{V}_0 + \sum_{n=1}^{N} \dot{V}_n e^{i\omega n t}\,. \tag{3.10}$$

Combining Equation 3.7, Equation 3.8 and Equation 3.10 results in

$$\begin{aligned} \dot{V}_0 + \sum_{n=1}^{N} \dot{V}_n e^{i\omega n t} = 2\pi \int_0^R -\frac{P_0}{4\eta} r \left(R^2 - r^2\right) \\ + \sum_{n=1}^{N} \frac{iP_n}{\rho\omega n} \left[1 - \frac{J_0\left(\Lambda_n \frac{r}{R}\right)}{J_0\left(\Lambda_n\right)}\right] e^{i\omega n t} r \,\mathrm{d}r\,. \end{aligned} \tag{3.11}$$

This can be considered as a polynomial of degree n, thus

$$\begin{aligned} \dot{V}_0 + \sum_{n=1}^{N} \left(\dot{V}_n e^{i\omega t}\right)^n = 2\pi \int_0^R -\frac{P_0}{4\eta} r \left(R^2 - r^2\right) \\ + \sum_{n=1}^{N} \left(\frac{iP_n}{\rho\omega n} \left[1 - \frac{J_0\left(\Lambda_n \frac{r}{R}\right)}{J_0\left(\Lambda_n\right)}\right] e^{i\omega t}\right)^n r \,\mathrm{d}r\,. \end{aligned} \tag{3.12}$$

The method of equating coefficients is used to determine P_0 and P_n. Starting with the time independent term ($n = 0$) gives

$$\dot{V}_0 = 2\pi \int_0^R -\frac{P_0}{4\eta} r \left(R^2 - r^2\right) \,\mathrm{d}r\,, \tag{3.13}$$

which yields after a few steps

$$P_0 = -\frac{8\dot{V}_0\eta}{\pi R^4}\,. \tag{3.14}$$

The same procedure is applied for the time dependent polynomials ($n \geq 1$). For the integration the relation for Bessel functions

$$\int cxJ_0(cx)\,\mathrm{d}x = xJ_1(cx)\,, \tag{3.15}$$

where c is a constant, is used. J_1 is the Bessel function of the first kind, first order. For the present case $c = \frac{\Lambda_n}{R}$ and $x = r$, and therefore

$$\int \frac{\Lambda_n r}{R} J_0\left(\frac{\Lambda_n r}{R}\right)\,\mathrm{d}r = rJ_1\left(\frac{\Lambda_n r}{R}\right)\,. \tag{3.16}$$

With this relation the integration and a subsequent rearrangement of the time dependent part

$$\dot{V}_n e^{i\omega t} = 2\pi \int_0^R \frac{iP_n}{\rho\omega n}\left[1 - \frac{J_0\left(\Lambda_n \frac{r}{R}\right)}{J_0\left(\Lambda_n\right)}\right] e^{i\omega t}\, r\,\mathrm{d}r \tag{3.17}$$

can be carried out, which gives

$$P_n = \frac{1}{\pi R^2}\frac{\dot{V}_n\rho\omega n}{1 - \frac{2}{\Lambda_n}\frac{J_1(\Lambda_n)}{J_0(\Lambda_n)}}\frac{1}{i}\,. \tag{3.18}$$

Inserting P_0 from Equation 3.14 and P_n from Equation 3.18 in Equation 3.7, and taking only the real part, finally yields the solution of the velocity field

$$\boxed{u(r,t) = \frac{2\dot{V}_0}{\pi R^2}\left(1 - \frac{r^2}{R^2}\right) + \Re\left\{\sum_{n=1}^{N}\frac{\dot{V}_n}{\pi R^2}\,\frac{1 - \frac{J_0\left(\Lambda_n \frac{r}{R}\right)}{J_0(\Lambda_n)}}{1 - \frac{2}{\Lambda_n}\frac{J_1(\Lambda_n)}{J_0(\Lambda_n)}}\, e^{i\omega nt}\right\}}\,. \tag{3.19}$$

The wall shear stress is defined according to Equation 1.2 as

$$\tau_w = \eta \left. \frac{\partial u}{\partial r} \right|_{r=R} . \tag{3.20}$$

Since $u(r,t)$ contains Bessel functions, the following expression is used for the calculation of the derivative

$$\frac{\partial}{\partial r}\left[J_0\left(\frac{\Lambda_n}{R}r\right)\right] = -\frac{\Lambda_n}{R} J_1\left(\frac{\Lambda_n}{R}r\right) , \tag{3.21}$$

and thus

$$\frac{\partial u}{\partial r} = -\frac{4\dot{V}_0 r}{\pi R^4} + \Re\left\{ \sum_{n=1}^{N} \frac{\dot{V}_n}{\pi R^2} \frac{\frac{\Lambda_n}{R} J_1\left(\Lambda_n \frac{r}{R}\right)}{J_0(\Lambda_n)} \frac{}{1 - \frac{2\,J_1(\Lambda_n)}{\Lambda_n J_0(\Lambda_n)}} e^{i\omega n t} \right\} . \tag{3.22}$$

Insertion of $\frac{\partial u}{\partial r}$ in τ_w from Equation 3.20 and evaluation at the wall ($r = R$) finally gives the wall shear stress

$$\boxed{\tau_w = \eta \left(-\frac{4\dot{V}_0}{\pi R^3} + \Re\left\{ \sum_{n=1}^{N} \frac{\dot{V}_n}{\pi R^3} \frac{\frac{\Lambda_n J_1(\Lambda_n)}{J_0(\Lambda_n)}}{1 - \frac{2\,J_1(\Lambda_n)}{\Lambda_n J_0(\Lambda_n)}} e^{i\omega n t} \right\} \right)} . \tag{3.23}$$

Measurement of Unsteady Volume Flow Rates

The unsteady volume flow rate $\dot{V}(t)$, respectively the amplitudes $\dot{V}_0$ and $\dot{V}_n$ of each mode, needs to be measured for the calculation of the analytical solution. Compared to steady flows, the measurement of an unsteady volume flow rate is a challenging task. Conventional flow meters have a response time typically in the order of one second. Thus, the amplitudes of varying flow rates may be underestimated. Compared to steady flows, additional problems arise due to the compliance of the walls, for example introduced from the hoses, which may dampen changes of the flow rate. An example

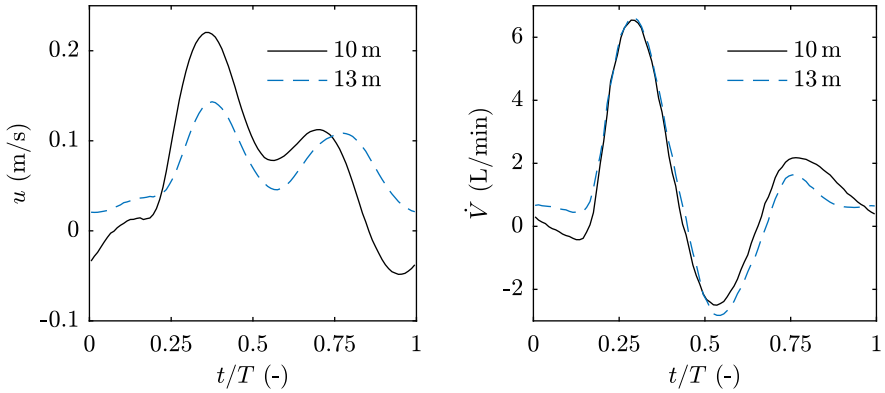

(a) Center line velocity in the measurement section.

(b) Volume flow rate measured with the Coriolis flow meter.

Figure 3.8: Effect of different hose lengths on the flow. Although the increase of the hose length is only 3 m and the flow rate at the flow supply unit is nearly the same, the center line velocity field at the measurement section is significantly influenced.

of the damping effect is shown in Figure 3.8, taken from an unsteady flow rate from the following chapter. Figure 3.8a shows the centerline velocity of a pulsating pipe flow measured with LDV with two equal volume flow rates but different hose lengths. Although the Coriolis flow meter, which is located directly at the outlet of the pump, shows almost no change between both cases (Figure 3.8b), the longer hose significantly dampens the velocity amplitude and introduces a phase shift. It seems therefore not applicable to measure the flow rate at the flow supply unit, but directly in the measurement section. As discussed in Büttner et al. (2008), LDV is a possible but also time-consuming method to measure the flow rate, since it is a point-wise technique. A more convenient solution is the determination of $\dot{V}(t)$ from the MRV data using the thresholding method explained in Figure 3.5a. The volume flow rate is then simply the sum over all voxels in the region of interest.

3.2.2 Laminar Pulsating Pipe Flows

The first flow to be examined is a laminar sinusoidal pulsating pipe flow with a time-averaged Reynolds number of $Re_{\mathrm{ta}} = 1038$ and an amplitude of $Re_{\mathrm{os}} = 596$ (case 1). The second and third flows examined represent realistic flow conditions for the human aorta. Their time dependent flow rate is very similar to those from Salsac et al. (2006) and shown in Figure 3.9. The first physiological pulsating pipe flow has a maximum of $Re_{\mathrm{max}} = 3952$ (case 2), the second flow $Re_{\mathrm{max}} = 7651$ (case 3), corresponding to resting and exercise conditions of a patient. According to Ray et al. (2012), the development length in pulsating pipe flows may be considerably shorter than those for steady flows. Thus, higher Reynolds numbers compared to the steady flows from the previous chapter can be realized. All experiments are conducted at a cycle duration of $T = 2.7\,\mathrm{s}$, which corresponds to a Womersley number of $Wo \approx 20$, characteristic for the ascending and descending aorta (Caro, 2012). Flow conditions and measurement parameters are summarized in Table 3.3. In the following paragraphs, the velocity profiles are first discussed and subsequently the WSS is evaluated.

Table 3.3: Flow conditions of the laminar pulsating pipe flows and corresponding MRV measurement parameters.

Parameter	Case 1	Case 2	Case 3
Flow	sinusoidal	physiological	physiological
Re (-)	$Re_{\mathrm{ta}} = 1038$ $Re_{\mathrm{os}} = 596$	$Re_{\mathrm{max}} = 3952$	$Re_{\mathrm{max}} = 7651$
Wo (-)	20.1	20.3	20.3
T (s)	2.7	2.7	2.7
Sequence type	2D1C + time	2D1C + time	2D1C + time
Voxel size (mm)	$0.4 \times 0.4 \times 3.0$	$0.4 \times 0.4 \times 3.0$	$0.4 \times 0.4 \times 3.0$
$venc$ (m/s)	0.05	0.1	0.2
TE (ms)	8.0	6.1	5.2
TR (ms)	45.2	37.6	34.0
FOV (voxels)	160×160	160×160	160×160
Phases (-)	59	71	79
N_{acq} (-)	3	3	3

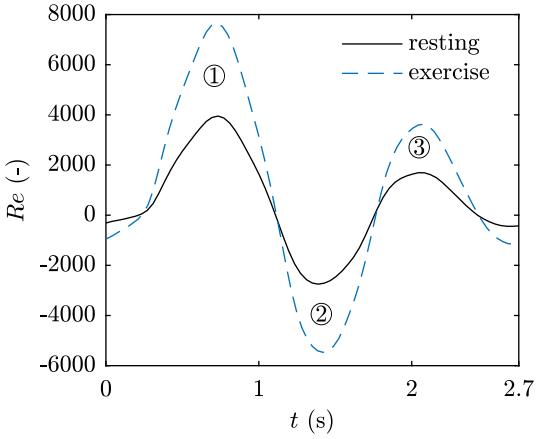

Figure 3.9: Temporal evolution of the Reynolds numbers, corresponding to resting and exercise conditions in the human aorta. The numbers refer to the points where the velocity profiles are analyzed. Adapted from Bauer et al. (2019).

The LDV signal, which is acquired over multiple cycles is phase-averaged in the same time intervals as the MRV data is measured, in order to compare the velocity profiles at the same time steps. Thus, it is necessary to examine how time resolved MRV data is acquired. The acquisition starts when the rising edge of the TTL trigger signal is detected (Figure 3.10). Then, a certain number of time steps is acquired during the cycle, which is schematically shown with gray boxes in Figure 3.10. In each time interval a complete MRV sequence, consisting of the excitation pulse, the spatial encoding, the velocity encoding, the readout and other parts like spoilers needs to be included. This corresponds to one single data point in the k-space. If additional time for multiple repetitions (multiple k-space coordinates) is available, the sequence can be repeated in the respective time interval. The duration of a single run of such a sequence is determined by many factors such as the FOV, the flip angle of the spins, the value of the *venc* and many more. Thus, its duration cannot be changed without changing the measurement parameters. This usually implies that at the end of the cycle a small dead time will be present, which is too short to fit in another time step.
It is assumed that the phase-averaged values from MRV and LDV are located

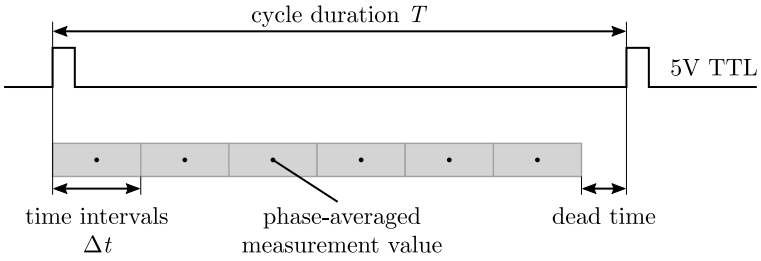

Figure 3.10: Triggering of the MRV sequence with the respective time intervals and the dead time at the end of the cycle.

in the middle of the respective time interval. Thus, the first time-averaged measurement data is located at $t = \Delta t/2$ after the rising edge of the TTL trigger signal, as shown in Figure 3.10.

Sinusoidal Flow

The velocity profile of the sinusoidal pulsating pipe flow, shown in Figure 3.11a, is evaluated at three characteristic time steps, which correspond to the instants of maximum, minimum and zero crossing of the volume flow rate. The SNR and relative velocity uncertainty of the MRV acquisition are calculated with the dual-acquisition method to SNR = 10 and $\sigma_u = 3.8\,\%$ of the maximum velocity. The red area represents the region, in which the velocity profiles of the 12 segments fall. Thus, this value gives an indication of the symmetry of the flow. The red curve represents the average value over all segments. The velocity profile shows small deviation from its symmetric values, especially for the time at maximum Reynolds number. However, the deviations become much smaller at the region near the wall. The analytical solution exhibits the characteristic parabolic velocity profile for laminar flows in the middle of the pipe. Near the wall the profile deviates from its steady solution due to the periodic change of the volume flow rate. Although the net volume flow rate is always positive, the flow experiences considerable back flow in the region near the wall, where viscous effects dominate over inertia forces. The laser Doppler and mean MRV data are in excellent agreement with the analytical prediction for all time steps.

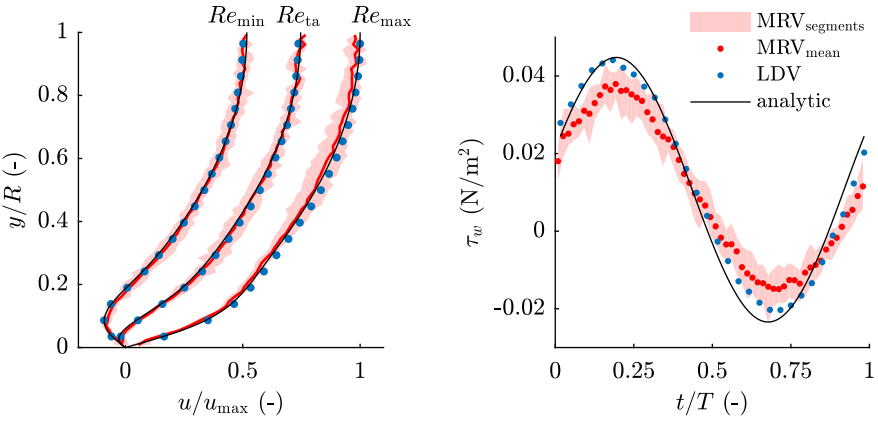

(a) Velocity profiles. **(b)** Wall shear stress.

Figure 3.11: Results of the laminar sinusoidal pulsating pipe flow from MRV and LDV, compared to the analytical solution. Adapted from Bauer et al. (2019).

The wall shear stress from LDV is calculated from a refined velocity measurement near the wall. The method developed in section 3.1.2 with a steady turbulent flow is used primarily for the exact determination of the wall position. In Figure 3.11b, the resulting wall shear stress τ_w is shown over the time t/T in the cycle. The laser Doppler data can capture the value of the wall shear stress very well. In the lower region of τ_w, the LDV data experience a slight underprediction of the amplitude of the wall shear stress as well as some minor phase shift. The MRV data shows a significant underprediction of the amplitude of about 25 %. Again a phase shift is noticeable. The red area marks the variations of the WSS between the individual pipe segments.

Physiological Flow at Resting Conditions

The velocity profile of the physiological pulsating pipe flow at resting conditions is shown in Figure 3.12a. The velocity shown is evaluated at the three peaks of the volume flow rate, which are maximum, minimum, and the second maximum, as indicated in Figure 3.9. The SNR of the MRV acquisition is SNR = 16 and the relative velocity uncertainty $\sigma_u = 3.2\,\%$ of the maximum velocity. Due to the higher frequencies present in the flow, compared to the

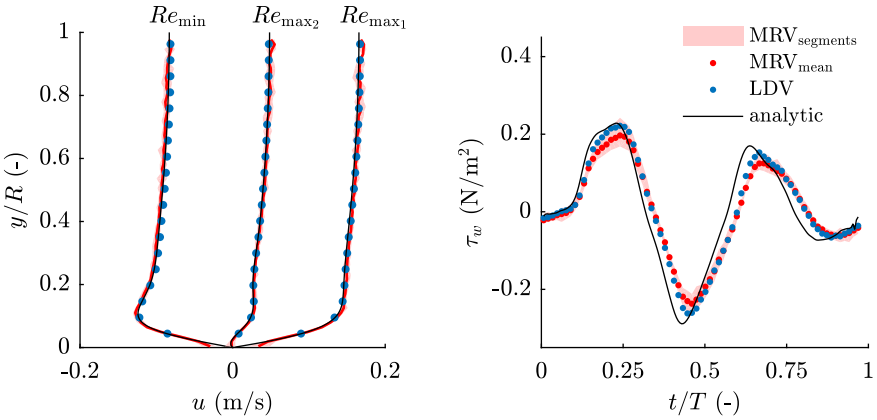

(a) Velocity profiles. **(b)** Wall shear stress.

Figure 3.12: Results of the physiological pulsating pipe flow at resting conditions from MRV and LDV, compared to the analytical solution. Adapted from Bauer et al. (2019).

sinusoidal case, the velocity profile has a very flat shape in the pipe center. Although the maximum Reynolds number is $Re_{\max} = 3952$, the velocity profile from both MRV and LDV measurements match perfectly the laminar solution. The accelerating motion appears to have a stabilizing effect on the flow, which is in accordance with previous findings from Iguchi & Ohmi (1984). The flow is perfectly symmetric in circumferential direction. Deviations between the individual pipe segments are insignificant.

The temporal evolution of the wall shear stress is depicted in Figure 3.12b. Although the flow waveform appears to have a smooth evolution in time, the analytical WSS experiences some additional curvature. The WSS shows three distinct extrema at $t/T = 0.25$, $t/T = 0.4$ and $t/T = 0.6$ from each of the amplitudes of the volume flow rate. Although the first maximum of the flow rate corresponds to $Re = 3952$ and the second maximum to $Re = 1694$, the amplitudes of the respective WSS do not differ so much with $\tau_w = 0.23\,\mathrm{N/m^2}$ and $\tau_w = 0.17\,\mathrm{N/m^2}$. The largest amplitude of the WSS at $t/T = 0.4$ ($\tau_w = -0.29\,\mathrm{N/m^2}$) originates from the backflow of the volume flow rate, which is not intuitively seen from Figure 3.9.

The laser Doppler is able to follow even the smaller excursions in the WSS.

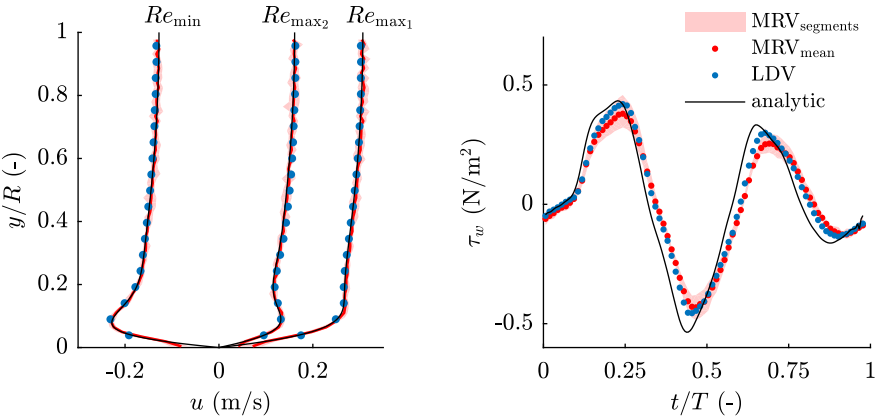

(a) Velocity profiles. **(b)** Wall shear stress.

Figure 3.13: Results of the physiological pulsating pipe flow at exercise conditions from MRV and LDV, compared to the analytical solution. Adapted from Bauer et al. (2019).

The data shows a slight underprediction of the amplitude of the theoretical value with a small phase shift. The WSS from the MRV measurements shows a larger underprediction of 14 % (first maximum, $t/T = 0.25$), 18 % (minimum, $t/T = 0.45$) and 26 % (second maximum, $t/T = 0.65$). The deviation of the WSS over the individual segments is minor.

Physiological Flow at Exercise Conditions

The velocity profile of the physiological pulsating pipe flow, shown in Figure 3.13a is almost equal in shape to the velocity profile from resting conditions. The curvature in the vicinity of the wall ($y/R < 0.2$) is slightly higher. One would expect the flow to be turbulent, with the maximum Reynolds number being $Re_{\max} = 7651$. As can be seen from the velocity profile in comparison to the analytical reference data, this is not the case. Again, all measured LDV and MRV data are in perfect agreement with the laminar solution. In addition, the flow is perfectly symmetric. The SNR and the velocity uncertainty of the MRV measurement are SNR = 16 and $\sigma_u = 2.9\,\%$ of the maximum velocity. The shape of the temporal wall shear stress (Figure 3.13b) is similar to that

under resting conditions, where only the amplitude increased. The laser Doppler shows a slightly larger underestimation of the amplitude in the back flow ($t/T = 0.45$) than in the former case. The MRV data underestimates the WSS about 12 % (first maximum, $t/T = 0.25$), 20 % (minimum, $t/T = 0.45$) and 24 % (second maximum, $t/T = 0.65$), which is in the same order than for the resting conditions. In general, the differences between resting and exercise conditions regarding underpredictions of the expected values are minor.

Discussion

Although the velocity profiles captured with LDV are in remarkable accordance with the analytical solution, the wall shear stress is systematically underestimated. The deviation can be explained with the finite size of the detection volume. In contrast to steady flows, the velocity profile close to the wall undergoes high curvature even in the laminar case. The linear gradient is not capable to resolve this curvature, which is schematically shown in Figure 3.14a. Theoretical considerations shall now be made to show how accurate the LDV measurements can capture the WSS for the given setup under ideal conditions without stochastic or other systematic sources of errors. This will give a quantitative estimation of the systematic error. The WSS is therefore evaluated between the point on the analytical velocity profile with a distance to the wall equal to the semi-axis of the DV b_d and the wall

$$\tau_{w,\text{biased}} = \eta \left.\frac{\Delta u}{\Delta y}\right|_{y=0} = \eta \, \frac{u_{\text{analytic}}(y = b_d)}{b_d} \quad . \tag{3.24}$$

Figure 3.14b shows the underestimation exemplary for the physiological flow at exercise conditions. The predicted underestimation at $t/T = 0.45$ is $\Delta\tau_w \approx 12\,\%$ of the maximum wall shear stress. The resulting curve coincides almost perfectly with the LDV measurements. With the finite size of the DV not only the underestimation can be explained, but also the reason for the phase shift becomes obvious. Recall Stokes second problem from section 2.1 and Equation 2.3:

$$u(y,t) = U_0 e^{-\sqrt{\omega/2\nu}\, y} \cos(\omega t - \sqrt{\omega/2\nu}\, y) \, . \tag{3.25}$$

As the distance y from the wall increases, the velocity from the oscillating wall is not only dampened, but also phase shifted. Note that the instantaneous WSS may be further under- or overestimated by this phase shift.

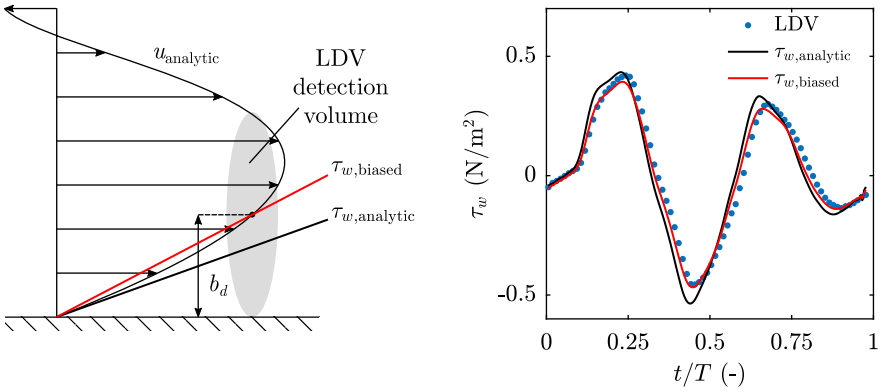

(a) Schematic representation of the analytical and biased velocity gradient.

(b) Predicted underestimation due to the finite size of the DV.

Figure 3.14: Systematic underprediction of the WSS from LDV, shown representative for the exercise conditions.

A possible solution to overcome this problem is to include more data points into the calculation of the wall shear stress and use polynomials instead of linear gradients. The use of a priori knowledge of the velocity profile can also be beneficial. As has been shown in Bauer et al. (2018), polynomials might improve the WSS. However, they are also susceptible for small stochastic errors. An interpolation with polynomials might result in even worse estimates, also known as Runge's phenomenon. On the other side, a priori knowledge is hard to achieve in more complicated flows or in *in vivo* situations. This problem is in general the same as the one introduced in section 1.2 about the treatment of MRV data with low spatial resolution, where different methods have been introduced to extrapolate the velocity profile to the wall position. In summary, the concept of linear gradients is maintained, while it can be confirmed that the finite size of the DV is the reason for some underestimation. However, LDV results are still considerably better than the reported errors in MRV measurements of up to 40 % (Petersson et al., 2012).

3.2.3 Transitional Pulsating Pipe Flows

As outlined in section 2.1, flows in the aorta may be in the laminar-turbulent transitional regime. Stochastically occurring turbulence and transition, whose onset is not clearly defined in space and time, cannot be measured with phase-averaging measurement techniques like MRV.
In contrast to steady flows, pulsating pipe flows do not have a critical Reynolds number, above which the flow changes from laminar to turbulent (Gündogdu & Çarpinlioğlu, 1999a). It is rather a combination of all three parameters Re_{ta}, Re_{os} and Wo, which determine whether a flow is laminar, transitional or turbulent. Furthermore, the transition can exhibit hysteresis, depending on the Womersley number. According to Iguchi & Ohmi (1984), pulsating pipe flows can be further categorized depending on their phase-locked behavior into four categories:

- *Laminar*, when the flow stays laminar over the entire cycle.
- *Transitional*, when the flow shows first and arbitrary turbulent structures, which do not occur phase-locked.
- *Conditionally turbulent*, when turbulence appears in every cycle at the same phase angle. These events do not persist over the entire cycle; the flow remains laminar in the remaining periods.
- *Fully turbulent*, when turbulence is present over the entire cycle.

Thus, the flows considered in this chapter need to be in the *conditionally turbulent* regime. The phase angle at which the turbulence occurs is then reproducible over consecutive cycles and measurable with MRV. In general, the flow does not transition to the turbulent regime as soon as the instantaneous Reynolds number $Re(t)$ exceeds a certain threshold. It is rather the case that the decelerating motion has a destabilizing effect on the flow (Iguchi & Ohmi, 1984). Thus, turbulence first appears in the decelerating phase of the cycle. The transition from the turbulent regime back to the laminar state during acceleration is called *relaminarization* (Ramaprian & Tu, 1980). On the other hand, the accelerating motion has a stabilizing effect. This may delay the transition to higher instantaneous Reynolds numbers compared to the steady case (Ramaprian & Tu, 1980). This effect has already been observed in the

Table 3.4: Flow conditions of the transitional pulsating pipe flows and corresponding MRV measurement parameters.

Parameter	Case 1	Case 2
Flow	sinusoidal	sinusoidal
Re (-)	$Re_{\mathrm{ta}} = 2642$ $Re_{\mathrm{os}} = 3265$	$Re_{\mathrm{ta}} = 2691$ $Re_{\mathrm{os}} = 3066$
Wo (-)	10.3	8.8
T (s)	10.5	14.5
Sequence type	2D3C + time	2D3C + time
Voxel size (mm)	$0.5 \times 0.5 \times 5.0$	$0.5 \times 0.5 \times 5.0$
venc (m/s)	0.3 (thr.), 0.05 (in)	0.3 (thr.), 0.05 (in)
TE (ms)	8.7	8.7
TR (ms)	187.2	187.2
FOV (voxels)	96×96	96×96
Phases (-)	53	77 (39+38)
N_{acq} (-)	2	2

previous chapter, where Reynolds numbers up to $Re_{\mathrm{max}} = 7651$ could be realized, which were still laminar.

Although the *conditionally turbulent* state has been studied extensively (Ohmi et al., 1982; Iguchi & Ohmi, 1982, 1984; Einav & Sokolov, 1993; Çarpinlioğlu & Özahi, 2012), controversy exists on the boundaries of this regime. However, all studies agree that *conditional turbulence* is more pronounced in flows with lower Womersley numbers than those considered in the previous sections. The flows used in this section are therefore conducted at $Wo = 10.3$ and $Wo = 8.8$, which are common conditions for the femoral arteries. The lower Womersley numbers imply rather long cycle durations of $T = 10.5\,\mathrm{s}$ and $T = 14.5\,\mathrm{s}$, which are beyond the maximum cycle length of $T = 10\,\mathrm{s}$ of the standard 4D flow sequence. Thus, the last $0.5\,\mathrm{s}$ of the first flow is cut off, while for the second flow the acquisition window is composed of two individual MRV measurements with starting points at $t/T = 0$ and $t/T = 0.5$ in the cycle. Detailed MRV measurement parameters and flow conditions are given in Table 3.4. These two flows are chosen because of an expected different behavior regarding turbulence.

The first goal of this chapter is to reproduce flow conditions which fall into the regime of *conditional turbulence* according to Iguchi & Ohmi (1984). In a second step methods are evaluated to detect transition and relaminarization in LDV and MRV measurements. This is essential to verify that transition occurs in both experimental investigations at the same time in order to allow comparison of the results. Afterwards, the effect of transition on the velocity field and wall shear stress is examined. Results of this section have already been reported on in the Master thesis of Mally (2019).

LDV Observations

Figure 3.15 shows the phase-locked axial and circumferential velocity components u_{LDV} and v_{LDV} from LDV in the center of the pipe. For the first case, velocity fluctuations u' and v' start to increase at $t/T \approx 0.15$, just shortly before the maximum axial velocity is reached. The fluctuations approach a maximum in the deceleration phase around $t/T \approx 0.5$ and then slowly decrease. In the accelerating phase, almost no fluctuations are present.
In contrast to this and also contrary to predictions from literature, velocity fluctuations in the flow case 2 appear in the acceleration phase, starting

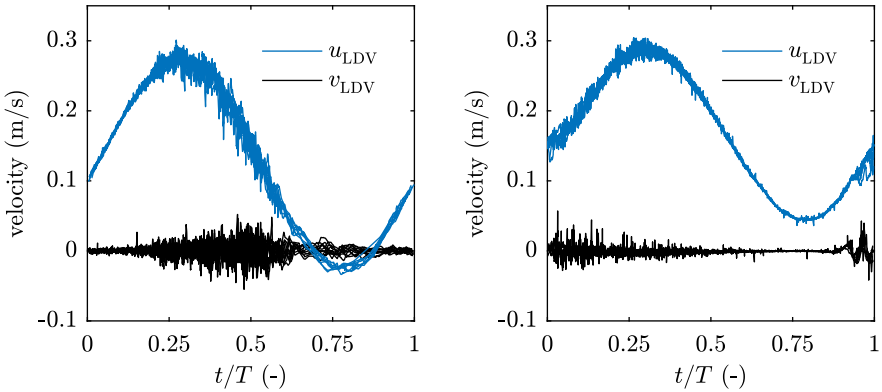

(a) Flow case 1. **(b)** Flow case 2.

Figure 3.15: Phase-locked velocities from LDV in axial (u_{LDV}, blue) and in circumferential direction (v_{LDV}, black). Fluctuations appear in both velocity components at the same time.

around $t/T \approx 0.9$ with a maximum fluctuation at $t/T \approx 0.1$ in the middle of the acceleration. Fluctuations then constantly decay. In the circumferential direction, there exists an oscillating motion at the beginning of the fluctuations ($t/T = 0.9$), which seems to be strictly periodic.

MRV Observations

Figure 3.16 shows the magnitude and in-plane velocity exemplary for the first flow case. At the time steps, where an increased turbulence in the LDV measurements is present, the noise in MRV also drastically increases in the magnitude and phase images. While at $t/T = 0.08$ almost no noise is present, considerable artifacts cover the image at $t/T = 0.46$. The noise is not only present in the region of the flow, but does also affect the image along the phase encoding direction. This is a sort of MRV measurement error known as turbulence artifacts, which is a special type of motion artifact (Petersson et al., 2010). The source of these artifacts is the turbulent fluctuating motion,

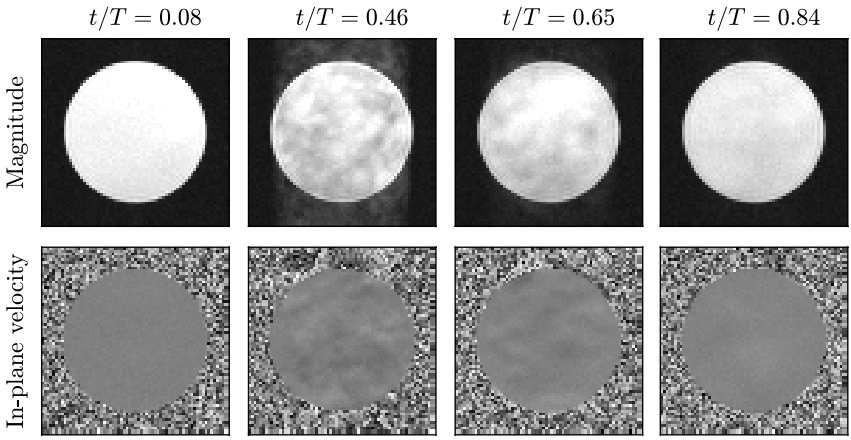

Figure 3.16: Magnitude and in-plane velocity of the flow from case 1 at different time steps. At $t/T = 0.08$ almost no noise can be observed, while at $t/T = 0.46$ considerable artifacts cover the images along the phase encoding direction. These artifacts decrease for $t/T = 0.65$ and are almost gone at $t/T = 0.84$.

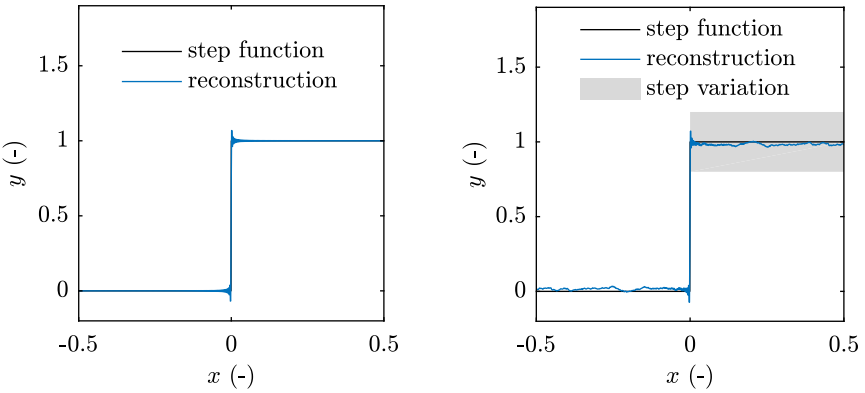

(a) Laminar case, with a constant step height.

(b) Turbulent case, where the step height changes during acquisition.

Figure 3.17: Simulation of the effect of turbulent motion on the MRV image.

while the reason is the piecewise sampling of the k-space during the MRV acquisition. This effect can be demonstrated with a simple 1D example of a MRV measurement:

Consider a step function as being representative of a velocity to be measured, shown in Figure 3.17a. The region $x < 0$ represents the region outside the flow field, while $x > 0$ represents the region inside the flow. During the MRV acquisition, the step function is Fourier transformed and subsequently reconstructed with a finite number of frequencies using an inverse Fourier transform. For the laminar case with a constant velocity, respectively step height, this results in the reconstruction depicted in Figure 3.17a. Ignoring the Gibbs phenomenon at the sharp edges of the step function for now, one can see that the region with constant amplitude is reconstructed very well. The amplitudes of the different frequencies from the Fourier transform 'interfere' with each other so that the sum of all modes results in an almost constant value.

Now we consider a step with varying step height during acquisition, for example caused by turbulent velocity fluctuations. To simulate a MRV sequence, the step is Fourier transformed and only a single frequency information is taken at a time, corresponding to a single row in the k-space. Then the step

height is arbitrarily changed, in the present example with a mean variation of 10 %. Subsequently the next frequency amplitude is obtained and so on. The reconstructed step function is shown in Figure 3.17b. Due to the inconsistency of the step height during acquisition, the sum of the different modes is not constant and affects the entire image. In a two or three dimensional MRV acquisition this effect takes place along the phase encoding direction. It has to be emphasized that these errors depend strongly on the flow, the MRI sequence, the sampling method and the reconstruction process.

Detection of Transition

The observations from MRV and LDV suggest to use the *spatial* noise in MRV, respectively the velocity uncertainty, as an indicator for turbulence and compare this with the *temporal* velocity fluctuations from LDV. It has to be emphasized that this method for the detection of transition does not provide a quantitative value of turbulence, as for example the method developed by Dyverfeldt et al. (2009), which was used in several other studies (Dyverfeldt et al., 2008; Freudenhammer, 2017). The present approach is rather to find an indicator for turbulence. The purpose is to demonstrate that phase-locked turbulent structures are present in both experimental investigations.
First, the velocity fluctuations u'_{LDV} and v'_{LDV} are obtained as a measure for turbulence. The phase-locked velocity from Figure 3.15 is divided into time intervals of equal width Δt, and in each interval the standard deviation of the velocity is calculated. Since the mean value of the axial velocity also changes with time, this would cause an error. Therefore, u'_{LDV} in axial direction is calculated according to

$$u'_{\mathrm{LDV}}(t_i) = \sqrt{\frac{1}{N-1}\sum_{n=1}^{N}(u_n - u_{\mathrm{fit}}(t_A))} \quad \text{for} \quad t_i - \frac{\Delta t}{2} < t_i < t_i + \frac{\Delta t}{2}\,, \tag{3.26}$$

where u_{fit} is a continuous curve, fitted to the temporal evolution of the phase-locked LDV signal, N is the total number of bursts in each time interval, t_A is the arrival time of the corresponding burst in the cycle with velocity u_n, and t_i is the time in the middle of each interval. In the circumferential velocity component no mean flow is expected, thus $u_{\mathrm{fit}} = 0$ for this case.
The velocity uncertainty of the MRV measurement $\sigma_{u,\mathrm{MRV}}$ is calculated with the dual-acquisition method according to Equation 2.26 for each time step.

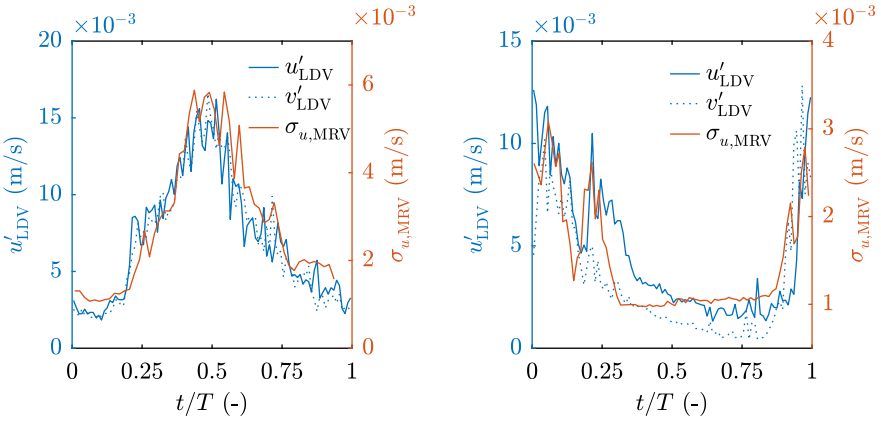

(a) Flow case 1. **(b)** Flow case 2.

Figure 3.18: Qualitative comparison of temporal fluctuations from LDV and spatial fluctuations from MRV.

Figure 3.18a shows the results for the first flow case. Note that this method does not allow a quantitative comparison, since the basis of the computations and the underlying phenomena are completely different. MRV and LDV show very good qualitative agreement with a starting point of the transition around $t/T \approx 0.2$ and a maximum at $t/T \approx 0.5$. The fluctuations from both LDV components are of the same order. For the second case, depicted in Figure 3.18b, the agreement is also very good. MRV fluctuations increase at $t/T \approx 0.8$, while LDV shows a slightly delayed increase at $t/T \approx 0.9$. Both LDV and MRV show a distinct peak of fluctuations at $t/T \approx 0.2$. Overall, the agreement of u'_{LDV}, v'_{LDV}, and $\sigma_{u,\mathrm{MRV}}$ is very good for both flows, suggesting that the transition occurs in both experimental setups at the same time.

Velocity Profiles and Wall Shear Stress

Velocity profiles of the flow case 1 are shown in Figure 3.19a. The LDV and MRV results are in good agreement. When the flow is in the transitional regime (Re_{ta}), the increased noise in the MRV data is visible as an apparent asymmetry over the individual segments. Compared to the results from the previous chapters, the curvature of the velocity profile is much lower in the

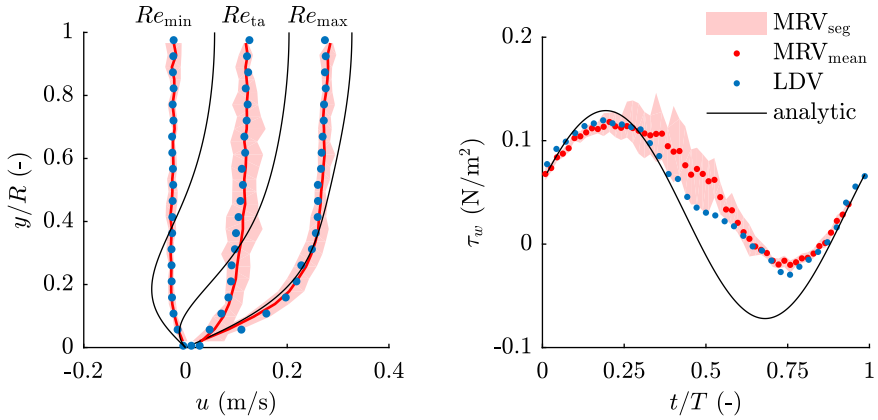

(a) Velocity profiles. **(b)** Wall shear stress.

Figure 3.19: Results of the transitional pulsating pipe flow (case 1) from MRV and LDV, compared to the analytical solution.

region near the wall due to the lower Womersley number. In the middle of the pipe the measured velocity profiles are significantly flatter than those from the analytical solution. On the other hand, the deviations at the wall depend strongly on the phase in the cycle. For the maximum Reynolds number ($Re_{\max}$), the profiles are in relatively good agreement in the region near the wall ($0 < y/R < 0.2$), while deviations increase during deceleration (Re_{ta} and $Re_{\min}$). The analytical solution shows a considerable backflow for the time of minimum Reynolds number ($Re_{\min}$), while LDV and MRV show a flat profile over the entire pipe cross-section.

The corresponding wall shear stress is shown in Figure 3.19b. MRV and LDV measurements are in very good agreement with the analytical solution for the accelerating phase, while at the decelerating phase the measured WSS is considerably higher. The noise in the MRV data is again clearly increased for $0.25 < t/T < 0.75$. The WSS from MRV starts to deviate from the laminar solution at $t/T \approx 0.3$, where also LDV values starts to deviate.

Velocity profiles and WSS both indicate that the turbulence significantly influences the flow field. When the turbulent bursts first appear ($t/T = 0.2$), the velocity profile flattens, leading to a higher wall shear stress and higher deviations from the analytical solution. As the turbulence decays, the velocity

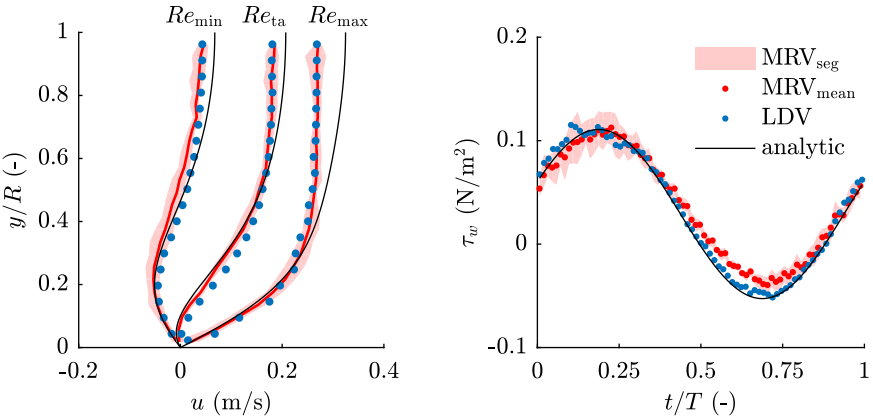

(a) Velocity profiles. **(b)** Wall shear stress.

Figure 3.20: Results of the transitional pulsating pipe flow (case 2) from MRV and LDV, compared to the analytical solution.

profile and the wall shear stress start to approach the analytical laminar solution. Due to the influence of viscous and inertia forces, the flow first starts to adapt to the laminar solution near the wall. Thus, the wall shear stress and velocity profile in this region are in very good agreement in the accelerating phase. Before the entire velocity profile has reached its fully developed state, the transition sets in within the next cycle.

Velocity profiles from flow case 2 are shown in Figure 3.20a. Again, the velocity profiles from MRV and LDV are in good agreement. The deviation from the analytical laminar solution is only apparent in the middle of the pipe, in the region approximately $y/R > 0.4$. In accordance with the occurrence of turbulent bursts, the deviations in the velocity profiles are most prominent at $Re_{\max}$, while the deviations are lower in the laminar phase during deceleration (Re_{ta} and $Re_{\min}$).

The wall shear stress from LDV (Figure 3.20b) shows no deviation from the analytical solution. Due to the low curvature of the velocity profile, the underestimation of the WSS from LDV is negligible. MRV shows a slightly lower amplitude of the WSS, probably due to minor deviations in the velocity profile at Re_{ta}. Compared to the flow case 1, no influence of the turbulence on the WSS can be detected.

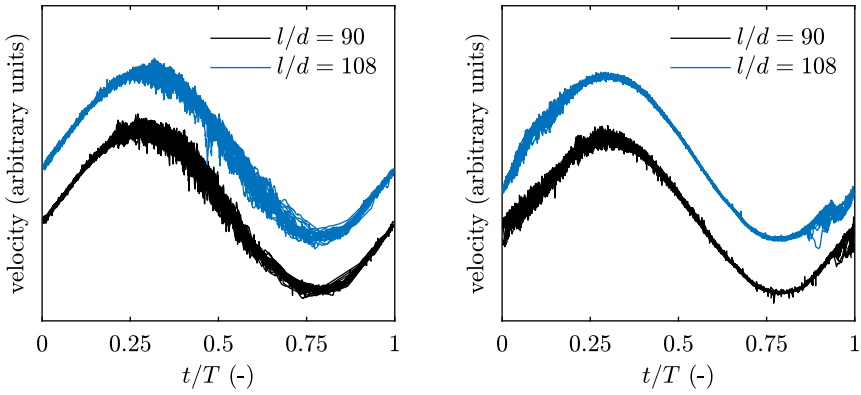

(a) Flow case 1. **(b)** Flow case 2.

Figure 3.21: Centerline velocities measured at the initial measurement section ($l/d = 90$) and downstream ($l/d = 108$) shows no change for the first case, but different behavior for the second flow case.

Discussion

While a strong influence on the WSS is found for the first flow, the turbulence in the second case seems not be strong enough to significantly change the velocity profile near the wall or influence the wall shear stress. The profiles deviate in the middle of the pipe from the analytical solution for the phases of turbulence, but near the wall no influence can be detected.
All LDV and MRV measurements were carried out at the axial distance of $l/d = 90$ downstream of the inlet. A variation of the measurement position l/d, depicted in Figure 3.21, shows an influence on the position of velocity fluctuations in the cycle for the flow case 2. This indicates that the second flow is not yet fully developed regarding turbulence and thus not completely located in the regime described by Iguchi & Ohmi (1984). As outlined in the literature, the transition in the *conditionally turbulent* regime occurs at all axial distances of the pipe at the same time. In the flow case 2, rather a locally bounded turbulent structure is present, which initially develops upstream of the measurement section, probably at the static mixer, and subsequently travels downstream carried by the flow field. Since its position in the cycle then depends on the axial measurement distance, this would also explain

why the turbulence is present in the accelerating phase. The strictly periodic motion at the beginning of the turbulence, at $t/T \approx 0.9$, can also be explained with this phenomenon. It is suggested that a longer inflow length would solve this problem, which on the other hand is not possible due to space limitations of the MRI scanner.
However, it cannot be ruled out that such an effect may also be present in the human circulatory system, where for example turbulent structures may originate from the heart and travel downstream into the aorta. This effect was already observed for the flow in the canine aorta (Nerem et al., 1972).

3.2.4 Summary: Pulsating Pipe Flows

In section 3.2.1 a modified analytical solution for pulsating pipe flows was derived, which uses the volume flow rate instead of the pressure gradient. The solution proved to be a valuable reference for the evaluation of velocity profiles and the wall shear stress. The necessary time dependent volume flow rate could be extracted from the MRV data with a thresholding method.
The flows considered in section 3.2.2 proved to be in the laminar regime. The WSS and velocity profiles could be measured very well with LDV. The azimuthal averaging of the MRV data showed good results for the wall shear stress compared to LDV. However, this method is restricted to axisymmetric flows in *in vitro* experiments. The high curvature of the velocity profiles near the wall leads to two implications compared to steady flows. First, the methods developed in section 3.1 need to be applied in a steady flow prior to each measurement to determine the wall position. Secondly, it could be shown that due to the curvature, the influence of the finite size of the detection volume is noticeable, although being only about $b_d \approx 150\,\mu\text{m}$ long. The wall shear stress is systematically underestimated with LDV up to 12 %. In contrast, the results from MRV show larger systematic underestimations of 12 - 26 %.
For transitional flows, discussed in section 3.2.3, the starting of transition could be detected from image artifacts in MRV data. Depending on the flow, a significant influence on the WSS and minor influences on the velocity fields were found.

4 Flow Through Aneurysms

In this chapter the measurements are extended to more complex geometries of aneurysms. **Section 4.1** discusses the steady flow through an aneurysm, while **section 4.2** addresses unsteady volume flow rates. Parts of this chapter have already been published in Bauer et al. (2019) and Bauer et al. (2020).

The modeling of the aneurysm geometry can be divided into the analysis of either patient specific or generic geometries. The advantage of the former are that specific information, e.g. before surgical intervention, can be obtained, allowing an individual prediction of the existing *in vivo* flow field. However, generic models provide a more general description of the problem, allowing a better comparison between different research groups, different WSS estimators and CFD codes. Exactly for these reasons, a generic geometry of an abdominal aortic aneurysm, initially shown at the beginning of this thesis in Figure 1.2a, is used in the present chapter.

Literature Overview

In literature there exist several experimental investigations of flows through generic aneurysms. The first experimental *in vitro* investigations were conducted by Scherer (1973), who performed numerous flow visualizations in optically transparent aneurysm models under steady flow conditions. It was found that the fluid passed through the middle of the aneurysm without following the aneurysm wall. Later on, Stehbens (1974) conducted also visualization experiments and investigated more closely the separation and reattachment points. In a following study, Musto & Roach (1980) measured the flow velocities in the aneurysm. Up to this point, all investigations focused on the velocity field without considering the wall shear stress.
Budwig et al. (1993) was the first who experimentally investigated the wall shear stress in a symmetric generic aneurysm and obtained preliminary results for the spatial distribution of the wall shear stress. Additionally, Budwig

et al. (1993) conducted several numerical simulations in laminar flows to obtain a continuous WSS distribution over the axial length of the aneurysm. Budwig concluded that in the areas around the attachment and reattachment points strong spatial gradients and high WSS peaks exist. The studies were extended by the group of Asbury and Peattie, who conducted several *in vitro* experiments on the flow patterns, the pressure distribution and the wall shear stress (Asbury et al., 1995; Peattie et al., 1996a,b). However, all studies examined only steady flow conditions.

Further experimental investigations were later conducted by Egelhoff et al. (1999) and Deplano et al. (2007, 2013, 2016), who considered pulsating volume flow rates. Deplano analyzed the effect of vortex development occurring under unsteady conditions. Due to the strong adverse pressure gradient in the deceleration phase of the cycle, vortex rings may detach at the inlet of the aneurysm, travel downstream, become unstable, and either decay or impinge on the wall located downstream. Nevertheless, in those studies the wall shear stress was not measured.

In this context, a comprehensive analysis of the time-varying wall shear stress distribution is given in Peattie et al. (2004), where also the stability of the developing vortex ring is discussed. Salsac et al. (2006) also gives a thorough description of the unsteady wall shear stress, but does not consider the instability and transition of the vortex ring. Both studies from Peattie et al. (2004) and Salsac et al. (2006) investigate peak Reynolds numbers based on the undilated vessel diameter of $Re_{\max} = 2300$ and $Re_{\max} = 2700$, which is presumed to be too low for the human aorta (Kousera et al., 2013). Yip & Yu (2001, 2003) provide an overall description of the flow inside an aneurysm, discuss the stability and decay of the vortex, as well as the spatial and temporal evolution of the WSS. Beside these experimental studies, there exist several numerical simulations of steady and pulsating flows through generic abdominal aneurysms, for example the works from Perktold (1987); Vorp et al. (1998) and Finol et al. (2003).

Flow Models and Experimental Setup

The geometry of the aneurysm model used in this study, which is shown schematically in Figure 4.1a, is axially symmetric with a smooth expansion of the diameter. The shape is based upon the work of Budwig et al. (1993), Peattie et al. (2004) and Salsac et al. (2006) with an inlet diameter equal to those of the straight pipe of $d = 26\,\text{mm}$ and a length of $L = 104\,\text{mm}$, corresponding to $L/d = 4$. The maximum diameter of the aneurysm is $D = 65\,\text{mm}$, thus the expansion ratio α is $\alpha = D/d = 2.5$. The function for the aneurysm radius r_A in dependence of its dimensionless length $x/d \in [-2, 2]$, where x denotes the axial distance measured from the point of maximum diameter (Figure 4.1a) is

$$r_A(x/d) = \frac{1}{2} + \frac{\alpha - 1}{2} \exp\left(4^{\zeta} - \left(0.25 - \left(\frac{(x/d) + 2}{4} - 0.5\right)^2\right)^{-\zeta}\right), \quad (4.1)$$

with the shape parameter $\zeta = 0.7186$. Compared to *in vivo* aneurysms, the size of the generic aneurysm model is relatively large, but not uncommon. Surgical intervention is typically recommended when the bulge diameter is larger than 50 - 55 mm (Kemmerling & Peattie, 2018).

Two geometrically identical aneurysm models are fabricated from polyamide using a laser powder bed fusion process (Formiga P100, EOS). The first model, which is used for the MRV measurements, is completely opaque. In the second model, optical access for LDV measurements is ensured. This optical access is given through a $128 \times 8\,\text{mm}$ slit in the model in the axial direction (Figure 4.1). The slit is covered with a 0.5 mm thick transparent film of polycarbonate, which is glued to the inner surface of the model. A recess of respective depth for the film is provided. Before insertion of the transparent film, the film is thermoformed onto a negative form of the aneurysm, ensuring a smooth transition without any abrupt edges.

For the measurement of velocity profiles with LDV, the aneurysm model is submerged in water (Figure 4.1b). The refractive index of the transparent film is not equal to the refractive index of the surrounding fluid, but due to the small thickness of only 0.5 mm, this introduces only an insignificant shift of the measurement position. For the acquisition of the wall shear stress, this setup does not allow an accurate determination of the wall-tangential velocity u_t, since the radial velocity component cannot be measured. Therefore, the

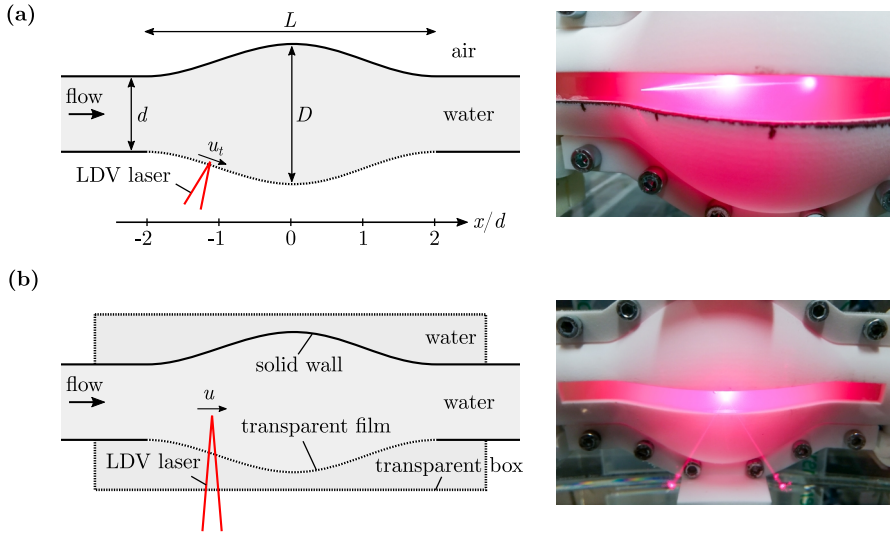

Figure 4.1: (a): Schematic representation of the aneurysm model including the geometric dimensions. This setup is used for measurements of the WSS, where the acquisition of wall-tangential velocities is possible. **(b)**: Aneurysm model submerged in water for LDV measurements of axial and circumferential velocities. Adapted from Bauer et al. (2020).

model is not submerged in water, but instead the LDV head is rotated for each measurement position along the axial distance x/d so that the optical axis is perpendicular to the surface (Figure 4.1a). The measurement of WSS requires only a penetration depth slightly deeper than the measurement volume size, thus the curvature effect of the aneurysm wall is negligible and the incidence angles of both laser beams can be assumed to be equal.

Post-Processing of the MRV Data

For the calculation of the wall shear stress and the velocity profiles from the MRV data, the same azimuthal averaging process is applied as for the pipe flows. The averaged data has the same spatial resolution as the original MRV data. The boundary of the geometry is determined as follows. First, the midpoint and diameter within each axial slice is determined from the MRV

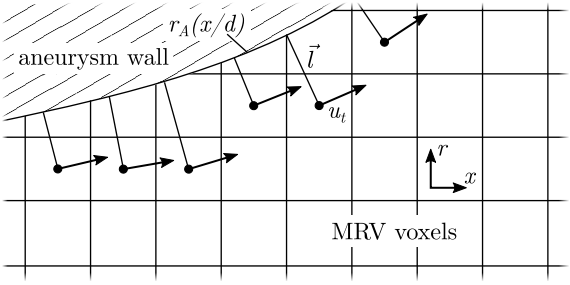

Figure 4.2: The WSS is calculated between the first voxel not embedded into the wall and the wall with radius r_A for each axial slice in x-direction. Adapted from Bauer et al. (2020).

magnitude, as described in section 3.1.2. Using the resulting center axis and the location of maximum diameter, the known geometry of the aneurysm is positioned.
The velocity gradient, respectively the WSS, is calculated between the first voxel located completely inside the flow field and the wall position

$$\tau_w = \eta \left.\frac{\partial u}{\partial y}\right|_{y=0} \approx \eta \frac{\Delta u_t}{\Delta y} \approx \eta \frac{u_t}{|\vec{l}|}, \tag{4.2}$$

with the wall-tangential velocity u_t and the distance to the wall $|\vec{l}|$, which is schematically shown in Figure 4.2. The wall position is known from the wall function r_A from Equation 4.1. There, the no-slip condition is assumed. Note that for each axial slice the distance $\vec{l}$ between the wall and the first MRV voxel varies.

4.1 Steady Aneurysm

In this section, steady flows through an aneurysm are examined. A laminar and a turbulent flow are considered, which Reynolds numbers are very similar to the steady pipe flows already discussed in section 3.1. The Reynolds number for the laminar flow in this section is $Re = 1998$, which is slightly higher compared to the flow through the straight pipe. It was chosen in order to be comparable to literature values from Budwig et al. (1993). MRV measurement parameters and flow conditions are given in Table 4.1.
The goal of the present experimental investigation is to generate a spatial distribution of the WSS within a flow model which is suited for both MRV and LDV reference measurements.

Table 4.1: Flow conditions of the steady flows through the aneurysm and corresponding MRV measurement parameters.

Parameter	Case 1	Case 2
Flow	laminar	turbulent
Re (-)	1998	5320
$\dot{V}$ (L/min)	2.31	6.20
Sequence type	3D3C	3D3C
Voxel size (mm)	0.5 (isotropic)	0.5 (isotropic)
$venc$ (m/s)	0.02	0.25
TE (ms)	11.6	6.9
TR (ms)	58.4	39.2
N_{acq} (-)	1	1

General Flow Phenomena

Figure 4.3a shows the velocity field in a cross sectional view of the aneurysm, obtained from the MRV measurement at the laminar flow conditions. The steady flow enters the aneurysm from the left and detaches from the wall due to the steep expansion and the associated adverse pressure gradient at about $x/d \approx -2$. Resulting from the detachment of the flow, a large recirculation zone forms in the middle of the aneurysm. The flow reattaches at an axial distance of $x/d \approx 2$. In the vicinity of the resulting stagnation point, shown

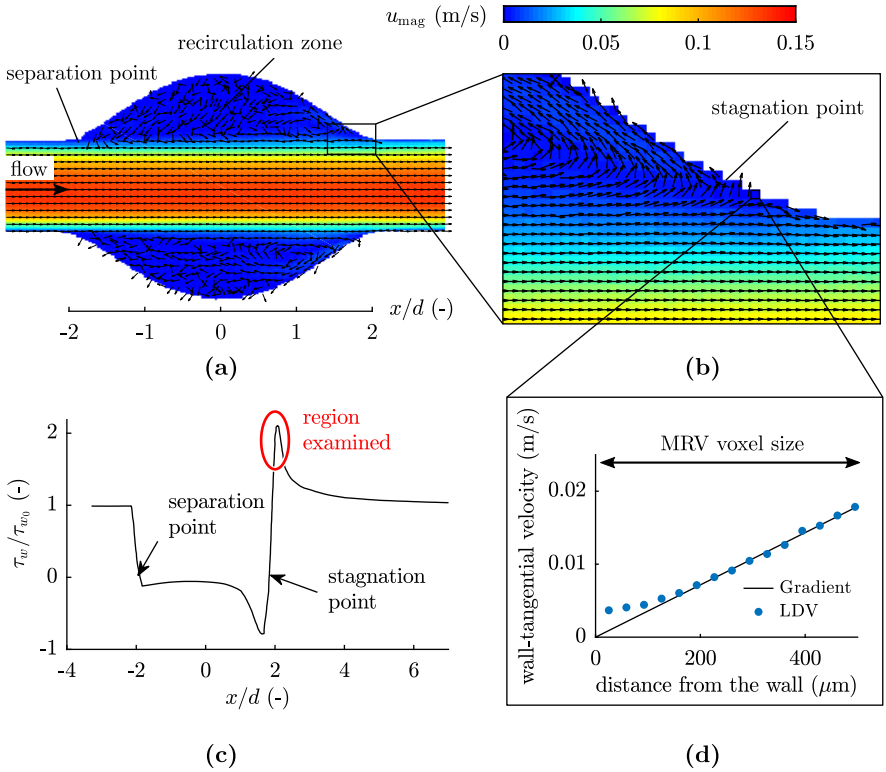

Figure 4.3: (a): Velocity magnitude of the MRV data in the middle of the aneurysm geometry at $Re = 1998$. **(b)**: Close-up view of the MRV data in the region near the point of reattachment, where local variations in the velocity lead to high spatial gradients of the wall shear stress. **(c)**: Results from Budwig et al. (1993) in a laminar flow show high spatial variations of the WSS. The region examined in this chapter is highlighted. **(d)**: Exemplary LDV measurement at an axial distance of $x/d = 2.1$. Adapted from Bauer et al. (2019).

in Figure 4.3b, large velocity gradients exist in the radial and axial direction, suggesting a high local wall shear stress with large spatial variations.
Results from Budwig et al. (1993), which are shown in Figure 4.3c, confirm that the wall shear stress experiences high spatial variations around the detachment point and in the local vicinity of the reattachment point. Downstream of the detachment point, the wall shear stress first reaches a minimum value, slightly below zero, due to the small negative velocities in the recirculation zone. At the reattachment point, the wall shear stress shows a continuous decrease followed by a sudden increase, reaching a global maximum of about $\tau_w/\tau_{w_0} = 2.2$, where τ_{w_0} is the WSS at the entrance of the aneurysm, respectively in the straight pipe. Downstream of the aneurysm the WSS slowly decreases and approaches the initial value of the pipe. In the turbulent flow with $Re = 5320$, the same flow characteristics are observed.
For clinical studies, these spatial variations may be the key factor for the development and growth of enlargements, as suggested by Meng et al. (2007) and Boussel et al. (2008). The challenge for *in vivo* measurements and post-processing algorithms is to properly resolve this variation.
For these reasons, the focus for the following LDV wall shear stress measurements is placed on a small region around the peak of the wall shear stress, downstream of the reattachment point, marked in Figure 4.3c. An exemplary WSS measurement with LDV at the point $x/d = 2.1$ is depicted in Figure 4.3d, showing also the high spatial resolution of LDV compared to MRV.

4.1.1 Laminar Flow

Numerical Simulations

In comparison to the pipe flows, neither an analytical solution nor an already available baseline computation is available to serve as a reference. Therefore numerical simulations, also referred to as computational fluid dynamics (CFD), provide comparison data of the velocity field and the associated wall shear stress. Additionally, since LDV is a pointwise measurement technique, it requires a rather substantial effort to measure the spatial distribution of the wall shear stress in the aneurysm. The CFD yields a more detailed distribution of the WSS, while individual LDV measurement points serve as control points to verify that the computations and measurements match.

The numerical simulations are conducted using the finite-volume based open source toolbox OpenFOAM® with the Semi-Implicit Method for Pressure Linked Equations (SIMPLE) for coupling the velocity and pressure fields. Since no turbulence is present in the laminar flow, the equations are solved directly without any additional turbulence models.
The total axial length of the solution domain covering the aneurysm geometry is $l = 13d$, with the inflow and outflow pipes being $l = 4d$ and $l = 5d$ long respectively. The computational mesh comprises 1.1×10^6 cells in total and 5.6×10^3 cells for each axial cross-sectional area. The mesh structure is a three-dimensional hexahedral mesh. Further grid refinement did not result in any noticeable changes in the velocity and wall shear stress values, thus it is presumed that grid independence has been reached. The zero-gradient boundary condition is applied at the outflow cross-section. The discretization of both convective and diffusive transport terms is achieved using the second-order accurate central differencing scheme (CDS).
For a better comparison with the experimental data, the CFD results from the hexahedral grid are averaged in azimuthal direction similar to the MRV data.

Improvement of SNR and Velocity Uncertainty

For the present 3D3C measurements of the aneurysm the acquisition time is rather long compared to the 2D1C measurements from the previous chapters. Thus, multiple repetitions to reduce the noise and measurement uncertainty are not possible due to the limited measurement time. As has been shown in section 2.3.2, the uncertainty furthermore reduces only by a factor of $1/\sqrt{N_{\mathrm{acq}}}$. A more effective method is to choose a lower velocity encoding value *venc*, which is linearly proportional to the velocity uncertainty $\sigma_u \propto venc$. The choice of a *venc* below the maximum flow velocity will however result in phase wraps and ambiguity. Phase wraps up to the second order can be corrected semi-automatically with an algorithm described in Bruschewski et al. (2014). For multiple phase wraps this method is no longer applicable.
For the measurement of the laminar flow through the aneurysm a method is proposed, which can handle multiple phase wraps. In a first 'reference' measurement the *venc* is set to $venc = 0.1\,\mathrm{m/s}$, which results in single phase wraps in the region of high velocities. These can be corrected semi-

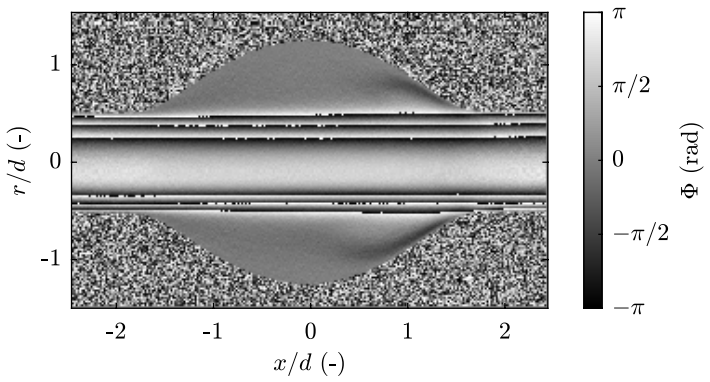

Figure 4.4: Phase image for $Re = 1998$ and $venc = 0.02\,\mathrm{m/s}$. Phase wraps up to the third order occur near the center axis of the aneurysm. This ambiguity can be corrected with a reference measurement.

automatically. Subsequently, a second acquisition is performed with $venc = 0.02\,\mathrm{m/s}$, resulting in phase wraps up to the third order, which is shown in Figure 4.4. The reference measurement is now used to correct those phase wraps. Thereafter the difference between both velocity fields is calculated and rounded to $2venc\,j$, where j is the number of phase wraps, shown in Figure 4.5. This is basically the same method proposed by Bruschewski et al. (2014), with the only difference being that the 'true' value of the velocity is known from the reference measurement.

With this method a reduction of the uncertainty by a factor of 5 is achieved with only 2 measurements, instead of $\sqrt{2}$ from an identical repetition. Note that the reduction of the *venc* is only feasible up to a certain limit, depending on the uncertainty of the initial reference measurement.

The SNR and velocity uncertainty of the MRV data are calculated from the single-acquisition method. The signal-to-noise ratio is SNR = 16 and the velocity uncertainty calculates to $\sigma_u = 0.4\,\%$ for the low *venc* and $\sigma_u = 2\,\%$ for the high *venc* acquisition.

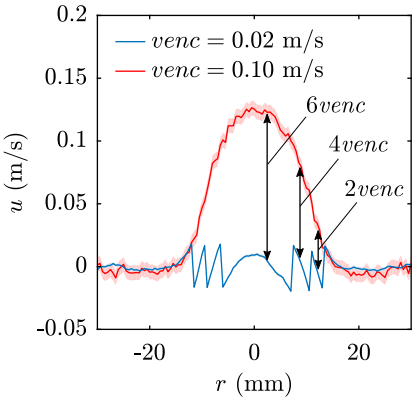

Figure 4.5: Velocity profiles at $x/d = 0$ from measurements with high and low *venc*. The shaded area indicates the $2\sigma_u$ interval.

Velocity Profiles and Inlet Conditions

To verify that the transparent film influences neither the LDV measurements nor the flow field, velocity profiles of MRV and LDV are compared. Measurements are performed at characteristic locations at the inlet of the aneurysm ($x/d = -2.2$), at the separation point ($x/d = -1.65$), at the point of maximum negative wall shear stress, where also the curvature of the transparent film is most prominent ($x/d = 1.4$), at the reattachment point ($x/d = 1.6$), at the point of maximum positive wall shear stress ($x/d = 1.8$), and at the outlet of the aneurysm ($x/d = 2.2$). Results are shown in Figure 4.6.
The MRV data exhibits a slight asymmetry of the flow field, which can be clearly identified from the deviations of the velocity profiles around the circumference. The asymmetry decreases considerably at the wall. The mean MRV velocity profiles agree well with the LDV measurements for all axial locations. Thus, no influence of the transparent film is found.
The maximum Reynolds number for which fully developed laminar inlet conditions can be achieved is $Re \approx 1356$, as outlined in section 3.1. Higher Reynolds numbers require a longer inlet pipe length, which is not possible due to geometric limitations at the MRI scanner. However, for a quantitative comparison between LDV and MRV, a flow which is not fully developed does

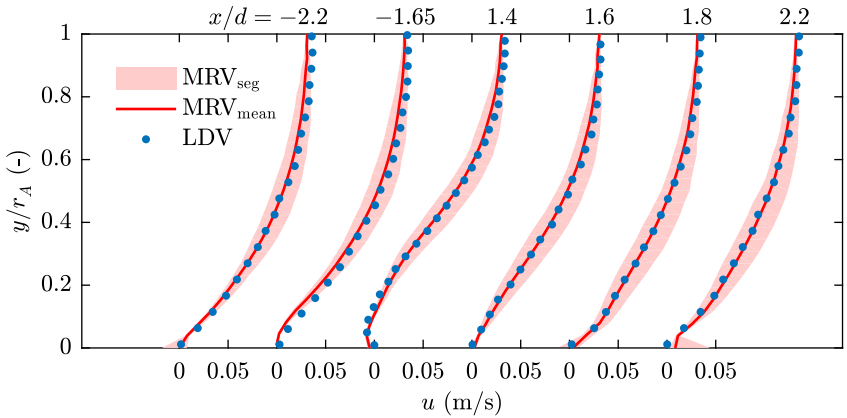

Figure 4.6: Velocity profiles from MRV and LDV at different axial positions x/d. The radial coordinate is normalized with the local aneurysm radius r_A.

not constitute an impediment as long as both flow conditions are equal. For the numerical simulation the boundary condition at the inlet of the aneurysm cannot be assumed to be a fully developed Hagen-Poiseuille profile and needs to be adapted to the present flow. Therefore, an additional inflow length of 2 m is provided in the simulation similar to the experimental setup, assuming an uniform velocity profile at the entrance of the pipe. This is in accordance with the velocity profile generated by the static mixer.
The different velocity profiles at the inlet of the aneurysm ($x/d = -2.2$) are shown in Figure 4.7. The inflow condition of the numerical simulation is in excellent agreement with the measured LDV velocity profile at the respective location. The analytical fully developed laminar solution predicts a higher velocity in the middle of the pipe and would therefore be erroneous. As already mentioned, the flow in the MRV measurements is slightly asymmetric.

Wall Shear Stress

For the laminar flow conditions, the region at the wall, where a nearly linear velocity profile prevails, is large enough to apply the same procedure as described in section 3.1.2 and which is shown exemplary in Figure 4.3d. A

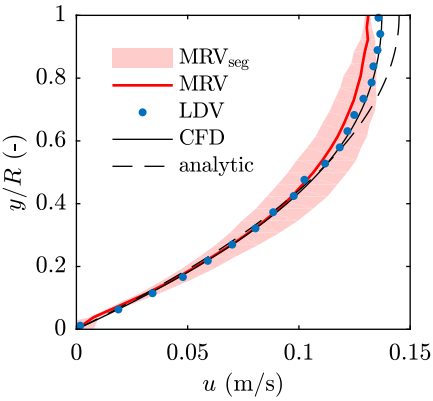

Figure 4.7: Velocity profiles at the inlet of the aneurysm. The analytical fully developed laminar solution does not coincide with the velocity profile obtained with LDV.

linear fit is used to determine the velocity gradient, while the measurement points which lie partially within the wall are omitted.

The results for the laminar flow through the aneurysm are shown in Figure 4.8. The laser Doppler shows a distinct peak of the wall shear stress at $x/d = 1.8$. Although even small upstream variations in the flow may influence the separation and reattachment points and thus the local wall shear stress, the experimental results are in excellent agreement with the numerical simulation. In comparison to the results from Budwig et al. (1993), the peak of the WSS is shifted approximately $x/d \approx 0.3$ upstream. The deviations from the wall shear stress in comparison to results from Budwig et al. (1993) may be caused by a slightly different shape of the aneurysm, which was not completely documented in Budwig et al. (1993).

The wall shear stress from the MRV data exhibits a systematic underestimation, especially in the regions of higher wall shear stress amplitudes ($1 < x/d < 2$). The high variance in the data around $1 < x/d < 1.5$ is caused by a variable distance $\vec{l}$ between the first voxel and the wall, which was shown in Figure 4.2. In this region, the curvature of the aneurysm wall is maximum. Compared to the CFD, the underestimation of the positive peak at the aneurysm outlet is 26 %.

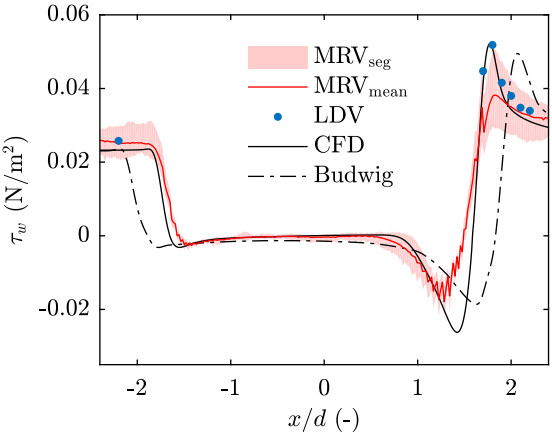

Figure 4.8: Experimental data compared to computational results for the wall shear stress distribution in the aneurysm at $Re = 1998$. Adapted from Bauer et al. (2019).

4.1.2 Turbulent Flow

For the turbulent flow the error analysis yields a signal-to-noise ratio of SNR = 21 and a velocity uncertainty of $\sigma_u = 1.1\,\%$. This seems quite low for a turbulent flow and as outlined in Bruschewski et al. (2016) this value may be biased due to turbulence. Since only a single acquisition is available, which does not account for these errors, it is expected that the true uncertainty is higher.

The determination of the gradient in the turbulent flow through the aneurysm is challenging. Only a few points remain in the linear region of the boundary layer velocity profile, contrary to the turbulent pipe flow initially discussed in section 3.1. In the following section, four different approaches for the estimation of τ_w from the LDV data are discussed, which may be better suited for this flow.

The first method is the aforementioned manual estimation of the gradient by visual inspection of the velocity profile. Usually this method results in the choice of the steepest gradient.

As suggested by many other authors (Clauser, 1956; Kendall & Koochesfahani, 2008; Rodríguez-López et al., 2015), the data points which lie outside the

viscous sublayer ($y^+ > 5$) may contribute as well to the calculation of the wall shear stress. The second and third methods to estimate τ_w are based upon this idea, which relies on the universal shape of the velocity profile, respectively the law of the wall, introduced in section 3.1.2. The principle used in the following paragraph is described in detail in Kendall & Koochesfahani (2008), while a good overview about similar techniques can be found in Rodríguez-López et al. (2015). The wall shear stress and the position of the wall are iteratively determined by fitting the measurement data to the aforementioned law of the wall or other empirically or numerically derived velocity profiles. The measured velocity u is normalized with respect to the friction velocity u_τ to obtain u^+

$$u^+ = \frac{u}{u_\tau}\,, \tag{4.3}$$

and the wall normal coordinate is expressed in the form of

$$y^+ \quad = \quad (y + y_0)\frac{u_\tau}{\nu}\,, \tag{4.4}$$

where y_0 is a possible offset of the wall distance. The values of u_τ and y_0 are chosen iteratively to fit the measurement data to the model. The optimal values for u_τ and y_0 are determined with the minimum of the residual function

$$\Psi(u_\tau, y^+) = \frac{1}{N}\sum_{n=0}^{N}\frac{|u_n^+ - u_{n,\mathrm{model}}^+|}{u_n^+}\,, \tag{4.5}$$

which is a measure of the difference between the measured data points u_n^+ and the model data points $u_{n,\mathrm{model}}^+$. The residual function gives more weight to the data points near the wall. The wall shear stress is then calculated from $\tau_w = u_\tau^2\rho$. Two models are used, to which the data is fitted:
For the first model the velocity profile developed by Musker (1979) is used. It is valid from the viscous sublayer to the logarithmic region and is given in the implicit form of

$$\frac{du^+}{dy^+} = \frac{\dfrac{(y^+)^2}{\kappa} + \dfrac{1}{C}}{(y^+)^3 + \dfrac{(y^+)^2}{\kappa} + \dfrac{1}{C}}\,, \tag{4.6}$$

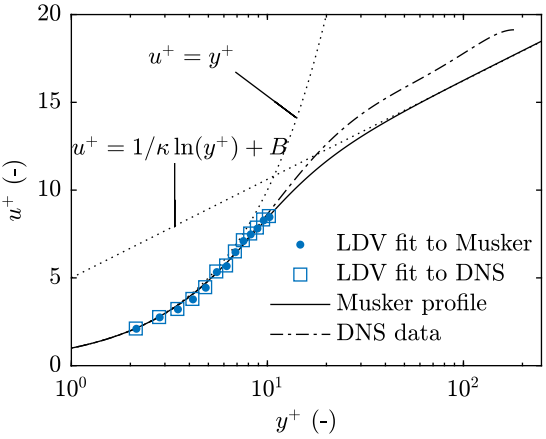

Figure 4.9: Velocity profiles in wall coordinates, including an exemplary fit of the measured LDV data at $x/d = 1.75$. Adapted from Bauer et al. (2019).

with $\kappa = 0.41$ and $C = 0.001093$.
The second velocity profile used as a model is the data from the DNS of a turbulent pipe flow at $Re = 5300$ from El Khoury et al. (2013). The axisymmetric geometry of the aneurysm motivated the use of this data set. Exemplary results of both methods are shown in Figure 4.9.
The last method to calculate τ_w is the one proposed by Durst et al. (1996b), which fits the measurement data to a model of the form

$$u = \frac{u_\tau^2}{\nu}(y - y_0) + C_2(y - y_0)^2 + C_4(y - y_0)^4 + C_5(y - y_0)^5 \,, \tag{4.7}$$

with the free fitting parameters C_2, C_4, C_5, u_τ and y_0. This method satisfies the momentum equation, but is restricted to the region $y^+ < 12$.
The results of all four methods are shown in Figure 4.10. The LDV measurements are in fairly good agreement with each other. All LDV post-processing methods show a peak of τ_w at $x/d = 1.8$. In general, the methods from Musker (1979) and the fit to the DNS data differ only slightly with a peak of $\tau_w \approx 0.4\,\mathrm{N/m^2}$. In comparison, the manual assessment yields slightly lower values, owing to the steep gradient and the few points inside the linear region. The method proposed by Durst et al. (1996b) gives considerable lower results

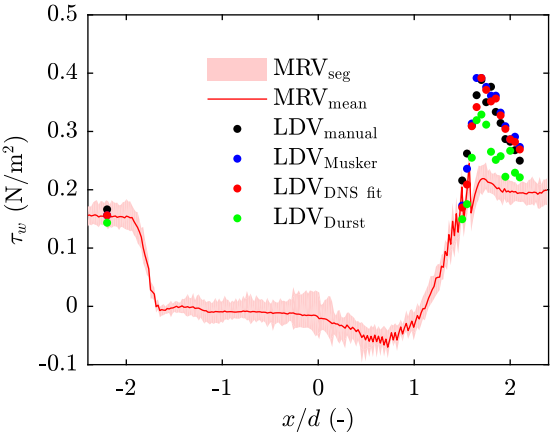

Figure 4.10: Wall shear stress distribution for different LDV post-processing methods, compared to MRV data of the turbulent flow. Adapted from Bauer et al. (2019).

with a peak of $\tau_w \approx 0.35\,\mathrm{N/m^2}$. Additionally, the data exhibits higher scatter. The reason for the similar results from the fits to the velocity profile from Musker (1979) and the DNS is the very similar velocity profile near the wall and the fact that the LDV data was restricted to this area (Figure 4.9). The reason for the highly scattered results obtained with the method proposed by Durst et al. (1996b) is unknown, but the method may be more sensitive to measurement errors.

The MRV data underestimates the local wall shear stress significantly in the region of the peak. The magnitude of this deviation is even higher compared to the deviations obtained from the laminar flow through the aneurysm. In contrast to the laminar flow, the symmetry before and after the aneurysm is less significant, but there exists a larger scatter in the recirculation zone. It should be mentioned that the turbulent flow field exhibits a high degree of non-uniformity due to turbulence artifacts, similar to the situation of the transitional pulsating pipe flows. The shaded area in this case is not only a measure for asymmetry, but also represents those turbulent fluctuations.

In summary, the LDV is able to capture the wall shear stress of the complex geometry of an aneurysm model and is able to identify regions where τ_w may affect the local behavior of the vessel walls.

4.1.3 Summary: Steady Aneurysm

The flow models presented in this section provide a spatial distribution of the wall shear stress. The transparent film, which was specially used in the LDV measurements, was not found to influence either the flow or the LDV measurement.
It was shown that a considerable reduction of the *venc* and a correction of occurring phase wraps with a reference measurement could significantly improve the image quality. When measurement time is limited, this method is better suited than a repetition of the MRV sequence with identical parameters.
The flow phenomena observed in the aneurysm are in line with predictions from literature. For the laminar case the wall shear stress from LDV was in excellent agreement with the numerical simulation and up to some extend also with the results from Budwig et al. (1993), although the geometry obviously differed. For the turbulent case all LDV post-processing methods showed a characteristic peak of the wall shear stress at the predicted location.
Wall shear stress values from MRV were notably underestimated (26 %) in the laminar case. In the case of the turbulent flow MRV even completely failed to predict a peak of the WSS value at the downstream end of the aneurysm.
In this section it was shown that LDV is capable of measuring a spatial distribution of the wall shear stress. Nevertheless, the effort for such measurements is significant since a complete velocity profile has to be acquired and the laser head has to be rotated and positioned for each axial location x/d of the aneurysm wall. On the other hand, numerical simulations provide a detailed and even three-dimensional WSS distribution. Thus, it seems beneficial to use CFD and LDV complementary. Results from CFD should be verified with LDV at several locations and the other way around.

4.2 Unsteady Aneurysm

In this section, the most complex and realistic flow considered in this study is analyzed. As outlined in the literature overview, an analysis of the wall shear stress of unsteady flows through aneurysms are rare and an extensive discussion of the time-resolved WSS distribution has not yet been presented. Thus, an additional goal of this section is to gain a deeper understanding of the wall shear stress distribution of a realistic pulsating flow through an abdominal aneurysm. The methods proposed in the previous chapters are used to achieve this goal. For example, the temperature stability is monitored to ensure a symmetrical flow field; the volume flow rate is extracted from the MRV data to obtain an analytical solution at the inlet and to serve as a boundary condition for a CFD simulation; the position of the wall for LDV measurements is determined from a velocity profile in a steady flow; the transparent film in the aneurysm is used to measure the WSS and velocity profiles; the velocity uncertainty from MRV is used to detect a possible laminar-turbulent transition, and a CFD is conducted to complement the sparse LDV measurement data.

Table 4.2: Flow conditions of the unsteady flow through the aneurysm and corresponding MRV measurement parameters.

Parameter	Value
Flow	physiological (exercise)
Re (-)	$Re_{\max} = 7649$
Wo (-)	20
T (s)	2.7
Sequence type	3D3C + time
Voxel size (mm)	0.6 (isotropic)
$venc$ (m/s)	0.25
TE (ms)	5.2
TR (ms)	128
Phases (-)	21
FOV (voxels)	$216 \times 224 \times 224$
N_{acq} (-)	1

The flow examined corresponds to the exercise conditions of the physiological pulsating pipe flow from section 3.2. Compared to the measurements in the straight pipe, the temporal resolution of the MRV measurement is reduced to 21 phases due to the increased acquisition time of 3D3C sequences. However, the spatial and temporal resolutions are still considerably higher than those used in *in vivo* applications. To accelerate the acquisition, the data is acquired with a k-t-accelerated 4D flow sequence (Bauer et al., 2013; Jung et al., 2008, 2011). Flow and MRV parameters are given in Table 4.2.
Results from section 3.2 show that this type of flow is laminar in a straight pipe over the entire cycle. However, as indicated in other studies (Yip & Yu, 2001, 2003; Peattie et al., 2004) a laminar-turbulent transition can be expected in the aneurysm at these Reynolds numbers.
Therefore, the velocity field is first examined in detail. Afterwards, the wall shear stress is analyzed and interpreted with respect to the occurring flow phenomena. Parts of this section have already been published in Bauer et al. (2020).

4.2.1 Numerical Simulations

As outlined in section 4.1, a continuous spatial WSS distribution over the entire axial length of the aneurysm is difficult to achieve with LDV. Thus, an extensive CFD simulation is conducted in parallel to complement the sparse LDV data (Bopp, 2018; Bopp et al., 2019a,b; Bauer et al., 2020).
The aneurysm geometry is meshed using OpenFOAMs® built-in function *blockMesh*, resulting in a three-dimensional hexahedral grid with 2.2×10^6 cells. The mesh is refined towards the wall, with the wall-next cells being located in the viscous sublayer at $y^+ < 1$ for the entire geometry and all time steps. At the inlet and outlet of the aneurysm an additional length of $5d$ is provided in each direction. The inflow condition is generated by a precursor simulation of the fully developed flow in a pipe of $2d$ length, which is schematically shown in Figure 4.11. After the fully developed state in the precursor has been reached, the flow field is mapped onto the inlet. The zero-gradient boundary condition is applied at the outflow cross-section. The temporal discretization corresponds to the second-order three-time step scheme with the Courant number Co adopted to be always $Co < 1$ due to the use of controlled adaptive time steps. The central differencing scheme is

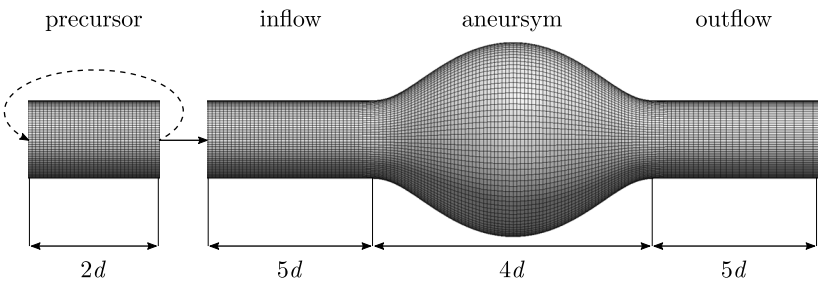

Figure 4.11: Mesh of the computational domain for the unsteady CFD simulation including the aneurysm, inflow, outflow and precursor with the respective axial lengths (not true to scale). Adapted from Bopp et al. (2019a).

used for the discretization of the convective terms.
Contrary to the laminar steady flow through the aneurysm, weak turbulence is expected in this configuration. Thus, an Unsteady Reynolds-Averaged Navier-Stokes (URANS) modeling framework is used for the computation.
An appropriate advanced turbulence model on the second-moment closure level is employed, which is denoted by Improved Instability-Sensitive Reynolds-Stress Model (IISRSM). This near-wall Reynolds stress model by Jakirlić & Hanjalić (2002) is capable of separately capturing the kinematic wall blockage effects related to both Reynolds-stress and stress dissipation anisotropies.
However, its straightforward temporal integration within the URANS method cannot adequately reproduce the turbulent activity intensification pertinent to a separated shear layer due to its time-averaged rationale. This is especially the case in flows which separate at a curved continuous wall, as encountered in the aneurysm configuration. Thus, this RANS model is further sensitized to account for fluctuating turbulence within the Unsteady RANS framework, as proposed by Jakirlić & Maduta (2015).
The computational model includes both scale resolved fluctuations and modeled turbulence. For this reason, the velocity field changes for consecutive cycles. Since MRV and LDV are phase-averaged measurements, the CFD data is also phase-averaged over 15 simulated cycles. The data is further averaged in the circumferential direction as already described in section 4.1 for the steady flow through the aneurysm.

4.2.2 Velocity Field

Prior to the evaluation of the wall shear stress, the velocity field is examined more closely. As suggested in other studies (Peattie et al., 2004; Yip & Yu, 2001, 2003), the flow through an aneurysm may be in a transitional regime even though the upstream flow in the pipe is laminar. It is therefore necessary to verify whether the same flow conditions are present in both experimental setups before proceeding further to the investigation of the WSS. First, the flow field obtained with MRV is examined. Afterwards, it is verified that LDV agrees well with MRV regarding the velocity field and laminar-turbulent transition.
In accordance with medical terminology, the upstream end of the aneurysm is called *proximal* end, while the downstream end is termed *distal* end.

MRV Velocity Field

The results of the MRV measurements are shown in a cross sectional (sagittal) view in Figure 4.12. Velocities are shown as velocity magnitudes.
At the beginning of the cycle ($t/T = 0.07$, Figure 4.12a), the flow is close to zero and the velocity vectors are randomly oriented. As the flow rate increases ($t/T = 0.21$, Figure 4.12b), a separation point develops at the inlet around $x/d \approx -1.8$, followed by a small recirculation zone downstream. The flow separation appears to have little influence on the velocity field downstream, where the flow is still fully attached. Subsequently, the flow rate reaches its maximum at $t/T = 0.26$ (Figure 4.12c). At this time the pressure gradient is already negative, which enhances the flow separation and the recirculation zone at the proximal neck. A symmetrical vortex ring forms downstream of the point of detachment, with its center initially located at $x/d \approx -1.3$. At the wall this vortex ring induces negative velocities. For the region $x/d > 0$ the flow is still fully attached and not influenced by the vortex. Subsequently the flow rate rapidly decreases ($t/T = 0.36$, Figure 4.12d), while the vortex ring reaches its maximum strength. Carried by the mean flow field, the vortex begins to travel downstream. At the center axis of the aneurysm a region with high velocities up to $u_{\mathrm{mag}} = 0.33\,\mathrm{m/s}$ exists, surrounded by the vortex ring. The vortex center induces reversed flow in the vicinity of the wall over a large area of $-1.0 < x/d < 0.2$. At $t/T = 0.45$ (Figure 4.12e), the flow rate is close to its minimum value. At the wall, the flow is again fully attached

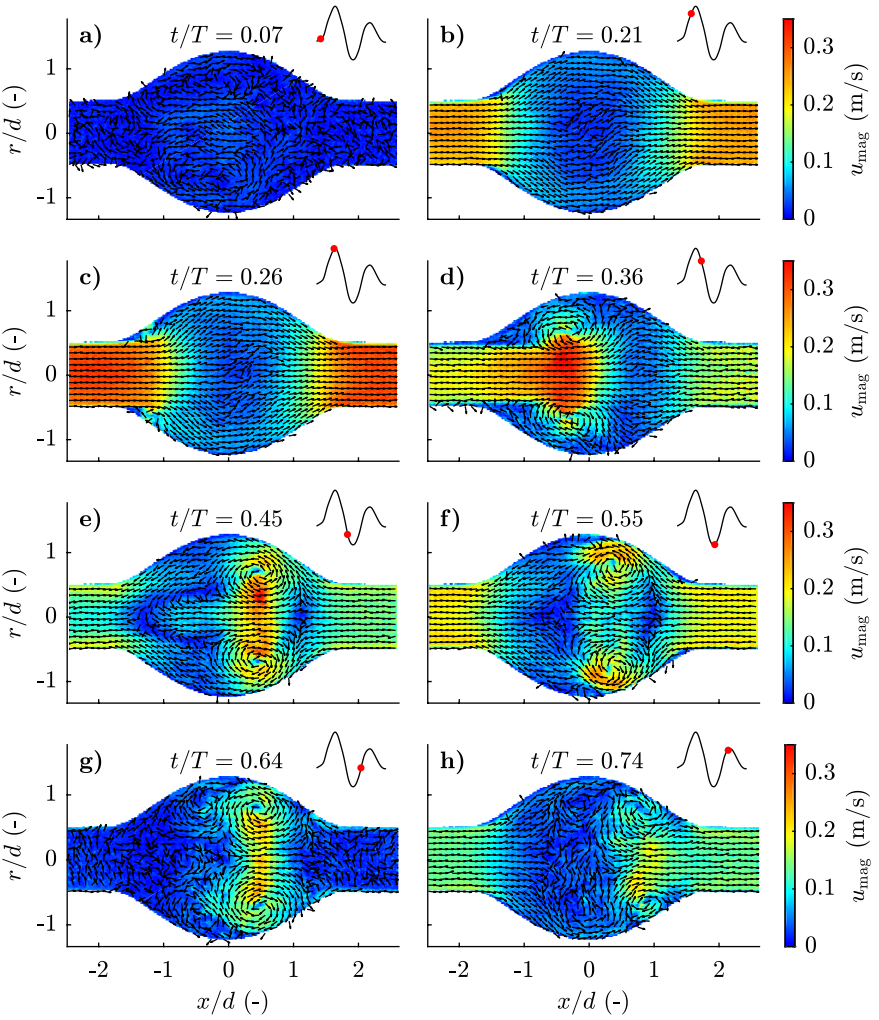

Figure 4.12: Time series of the velocity field obtained with MRV, in a sagittal view. The respective flow rate at each time step is depicted in the upper right corners. At the beginning, the flow is fully attached **(a)**, then the flow detaches at the proximal neck due to the increasing flow rate **(b)**, and forms a vortex ring **(c)**, which subsequently induces negative velocities at the wall, grows, and travels downstream **(d-e)**, weakens **(f-g)** and finally dissipates **(h)**. Adapted from Bauer et al. (2020).

over the entire aneurysm length, but with velocity vectors pointing in the upstream direction. At $t/T = 0.55$ (Figure 4.12f) a secondary separation zone forms at the distal neck of the aneurysm at $x/d = 1.5$. However, this region initially covers only a few voxels. Compared to the previous time step the primary vortex ring has traveled upstream due to the negative flow rate and lost strength. Starting from $t/T = 0.64$ (Figure 4.12g), the vortex ring begins to decay significantly. As the volume flow rate reaches its second maximum at $t/T = 0.74$ (Figure 4.12h) the vortex is almost completely dissipated. In the region where the vortex impinged onto the wall, only a weak circulation and fluctuating velocities remain. In the later cycle the flow rate approaches zero and the flow in the aneurysm comes to a rest.

Comparison with LDV and CFD Data

Velocity profiles of the axial component from MRV and LDV measurements are shown in Figure 4.13. Since laser Doppler velocimetry is a pointwise measurement technique, velocity profiles are acquired along straight lines between the center axis and the transparent wall at six different locations, which are at the inlet of the aneurysm ($x/d = -2.2$), the point of separation ($x/d = -1.3$), the center of the aneurysm ($x/d = 0.0$), the region where the vortex impinges onto the wall and maximum WSS values are expected ($x/d = 0.6$ and $x/d = 1.0$) and at the outlet ($x/d = 2.2$).
MRV velocity profiles are obtained by circumferential averaging. The red curve in Figure 4.13 represents the mean velocity over all segments, while the shaded area is the range, where all 12 velocity profiles fall. The velocity profiles are evaluated at the peak volume flow rates of $t/T = 0.02, 0.26, 0.55$ and 0.79.
At $t/T = 0.02$ (Figure 4.13a), just before the volume flow rate increases, the velocity profiles from MRV and LDV coincide excellently for all axial distances. The velocity fluctuations u' from LDV, which are shown with error bars, show no significant indications of turbulence; only minor fluctuations in the middle of the aneurysm exist. The flow is perfectly symmetric, as can be seen from the MRV velocity for the different segments. The analytical laminar solution does not fit either at the inlet or outlet. For $t/T = 0.26$ (Figure 4.13b), mean values agree well. Flow separation starts to take place at the proximal end ($x/d = -1.3$), where the results show negative velocities at the wall and a

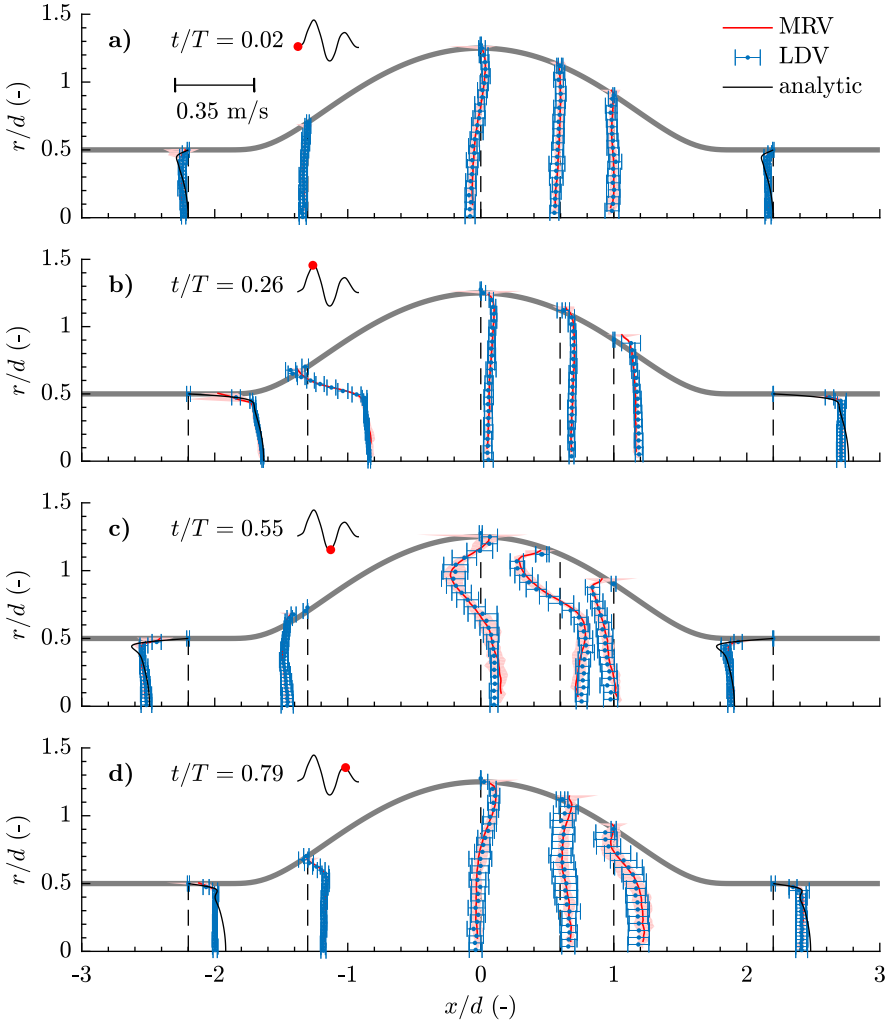

Figure 4.13: Comparison of velocity profiles at four time steps, acquired with MRV and LDV. An analytical solution is depicted at the inlet and outlet. LDV error bars show the velocity fluctuations u', the shaded area indicate the variation of the MRV velocity profiles over the circumferential direction. In the first time step a length scale for the velocity amplitudes is given. (Reprinted from Bauer et al. (2020), with permission of Springer Nature. © 2020 Springer Nature.)

recirculation zone. While for all axial positions u' has decreased, fluctuations increase in the shear layer at $x/d = -1.3$, where the vortex ring develops. Despite the periodic flow separation, the velocity field shows no deviation from symmetry. The analytical laminar solution fits perfectly for the high volume flow rates at the inlet, but not at the outlet. At this point, the velocity profile is significantly flattened. At the time of maximum negative volume flow rate ($t/T = 0.55$, Figure 4.13c), the vortex ring has reached the distal end of the aneurysm. Mean velocity profiles show again good agreement. However, large fluctuations are present in the region near the vortex ring, accompanied by an apparent asymmetric MRV flow field. Minor deviations from the mean value exist near the center axis. The analytical solutions at the inlet and outlet do not fit the measurements well. For $t/T = 0.79$ (Figure 4.13d) the fluctuations are lower in the inlet due to the forward flow. Absolute mean velocities especially at $x/d = 0.6$ are lower; however fluctuations still persist there.

The deviations of the mean MRV values from LDV near the center axis originate most likely from less voxels available at this position in the averaging process. Furthermore, MRV values at the wall are subject to partial volume effects. In both regions the accuracy and reliability of the MRV data is therefore reduced.

The results from LDV indicate that in the center of the aneurysm the vortex introduces instabilities, as noticed in several other studies (Yip & Yu, 2001, 2003; Peattie et al., 2004). It is therefore assumed that these instabilities lead to either weak turbulence or non-periodic velocity fluctuations between consecutive cycles. This might also cause the flattened velocity profile at the outlet in Figure 4.13b compared to the inlet, due to enhanced mixing in the aneurysm bulk. The WSS values are expected to be higher at the outlet than in the inlet. Inspection of the MRV velocities as well as the magnitude data show that in the area, where the vortex ring introduces large velocity fluctuations, image artifacts occur, which potentially lead to the apparent deviations between individual MRV segments. The flow is therefore not necessarily asymmetric in these stages of the cycle, but affected by image artifacts due to velocity fluctuations. These fluctuations do not decay completely during one cycle and are therefore present until the next increase of the volume flow rate ($t/T = 0.02$, Figure 4.13a).

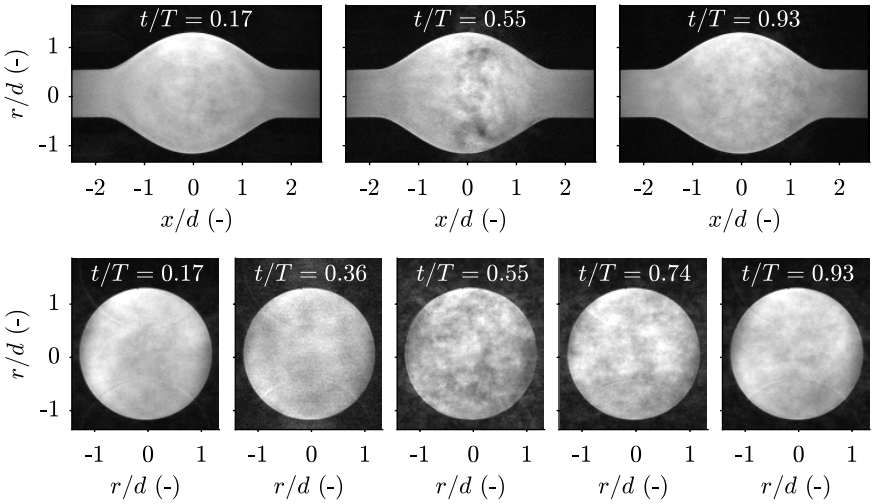

Figure 4.14: Top row: MRV magnitude data in a sagittal plane in the middle of the aneurysm for three different time steps. Bottom row: Transverse plane at $x/d = 0$ for five different time steps. The vortex decay introduces substantial image artifacts around $x/d \approx 0$ for $t/T = 0.55$. (Reprinted from Bauer et al. (2020), with permission of Springer Nature. © 2020 Springer Nature.)

Deviations from the analytical solution at the inlet are caused by the back flow through the aneurysm; hence, not providing sufficient time to fully develop in the later phase of the cycle.

Turbulence and Velocity Fluctuations

Figure 4.14 shows the MRV magnitude. The noise drastically increases during the time steps when the velocity fluctuations are present in the LDV data. Image artifacts appear around $x/d \approx 0$ and $t/T = 0.55$ where the vortex ring introduces substantial velocity fluctuations. Visual inspection of the MRV data suggests that this noise could be used as an indicator for the laminar-turbulent transition as already discussed and evaluated for the transitional pulsating pipe flow in section 3.2.3. For a qualitative estimation of the transition the *time dependent* velocity fluctuations obtained from LDV are compared to the *spatial* image fluctuations and thus the velocity uncertainty from MRV.

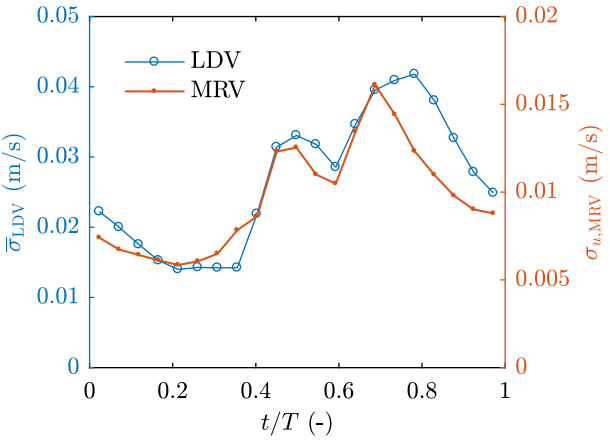

Figure 4.15: Temporal evolution of the mean velocity fluctuations $\overline{\sigma}_{\mathrm{LDV}}$ from LDV and the velocity uncertainty $\sigma_{u,\mathrm{MRV}}$ from MRV at $x/d = 0.6$. Adapted from Bauer et al. (2020).

In the LDV data an axisymmetric turbulence ($v' = w'$) is assumed and a mean fluctuation σ_{LDV} over all velocity components is computed

$$\sigma_{\mathrm{LDV}} = \sqrt{\frac{1}{3}\left(u'^2 + 2v'^2\right)}\,. \tag{4.8}$$

Additionally, an average velocity fluctuation $\overline{\sigma}_{\mathrm{LDV}}$ is calculated for each of the 6 axial positions, where the velocity profiles in Figure 4.13 have been acquired.
For the MRV data, the velocity uncertainty is calculated according to section 2.3.2 with

$$\sigma_{u,\mathrm{MRV}} = \frac{venc}{\pi}\frac{1}{\mathrm{SNR}}\,. \tag{4.9}$$

As only one MRV dataset is available ($N_{\mathrm{acq}} = 1$), the single-acquisition approach is used. According to NEMA (2014), the region in the background actually needs to be free of artifacts. However, as the intention of the present approach is to detect those artifacts, a region in the background along the phase encoding direction is used, which includes those artifacts.
Results of the computations are shown in Figure 4.15 exemplary for a slice

located at $x/d = 0.6$. Both values show very good agreement. The uncertainty increases as the vortex ring approaches the slice ($t/T \approx 0.5$) and gradually decreases when the volume flow rate is negative and the vortex ring moves upstream ($t/T \approx 0.6$). The velocity uncertainty $\sigma_{u,\mathrm{MRV}}$ has its maximum at $t/T \approx 0.7$, while LDV shows a maximum around $t/T \approx 0.8$. Possible deviations may occur due to the calculation of a mean turbulence intensity over each velocity profile in the LDV measurements. Taken as a whole, the agreement is fairly good.
It has to be emphasized that the present methods for the detection of transition have been employed on phase-locked (LDV), respectively phase-averaged (MRV) data. Thus, it cannot be ruled out that the flow through the aneurysm is in the laminar regime over the entire cycle and only differs between consecutive cycles. A change of the laminar velocity field between consecutive cycles would lead to an increased standard deviation within each time interval of the phase-locked LDV signal. In addition, it would lead to the so-called turbulence artifacts in the MRV data due to inconsistencies between different k-space rows.
However, it is assumed that the same effects appear in the LDV and MRV data at the same time, suggesting that the WSS values will be comparable. In summary, the agreement of the velocity fields between the experiments is excellent, so that a substantiated comparison of WSS values is now feasible.

4.2.3 Wall Shear Stress

The wall shear stress from MRV is calculated from the circumferentially averaged velocity field, where the averaged data has the same spatial resolution as the original data. A symmetric flow field is required for this procedure, which has been verified in the previous section.
For the determination of the wall position as well as the first LDV measurement point totally inside the aneurysm, the procedure described in section 3.1 is used. Afterwards, the velocity gradient is measured with the unsteady pulsating volume flow rate. The laser Doppler signal is phase-averaged at 84 time steps ($\Delta t = 32\,\mathrm{ms}$ intervals), which is four times the temporal resolution as MRV. The CFD data is obtained at 270 time steps ($\Delta t = 10\,\mathrm{ms}$ intervals). The spatial distribution of the WSS from MRV, LDV and CFD for the first half of the cycle is shown in Figure 4.16 and for the second half of the cycle in

Figure 4.17. The circumferentially averaged velocity field from MRV is given on the bottom (using the right colorbar and the lower axis), while the WSS distribution of the corresponding time step is depicted on top (using the left axis). Additionally, the vortex centers of the flow field are identified manually and their position is highlighted. The most prominent vortex ring is termed *primary* vortex, while all other vortices are referred to as *secondary* vortices.
In general, almost no deviation between the individual LDV measurement points and the numerical simulation is observed in the first half of the cycle. In contrast, the results from MRV show significant underpredictions, especially in the regions and at the time steps where high WSS peaks are present. Below, the WSS distribution is discussed in detail for each time step.
While the volume flow rate is close to zero (Figure 4.16a), the WSS is negligible small over the entire aneurysm length. In the middle of the flow field a secondary vortex is still present from the previous cycle, which does not influence the WSS.
During the time steps when the flow rate increases (Figure 4.16b,c) no vortex is present in the aneurysm. The global WSS distribution is almost similar to the distribution encountered in steady flows (Budwig et al., 1993; Bauer et al., 2019). The constant wall shear stress observed in the straight pipe drastically decreases when the flow enters the aneurysm. At $t/T = 0.21$ (Figure 4.16c) a separation point forms at ($x/d = -1.6$) followed by a small zone of weak recirculation and a negative WSS. The wall shear stress then remains almost constant over the aneurysm length until the proximal end, where a distinct peak of $\tau_w = 0.85\,\mathrm{N/m^2}$ is observed. Downstream of the peak the WSS continuously decreases due to the development of the laminar velocity profile in the pipe. In general MRV is not capable of resolving the high WSS peaks at the distal and proximal ends, yielding an underestimation up to 56 %.
Due to the formation of a primary vortex from the recirculation zone at $t/T = 0.26$ (Figure 4.16d), the CFD results exhibit a very narrow peak of $\tau_w = -0.8\,\mathrm{N/m^2}$ at $x/d \approx -1.3$. The strong vortex formation causes a secondary, minor and counter rotating vortex to develop upstream, which cannot be resolved properly with the low spatial resolution of MRV, but is clearly visible in the WSS distribution from CFD. This leads to a localized positive WSS in the area around $x/d \approx -1.4$. At the outflow of the aneurysm τ_w reaches its maximum value during the entire cycle of $\tau_w = 1.1\,\mathrm{N/m^2}$, which is again significantly underestimated by 54 % with MRV.

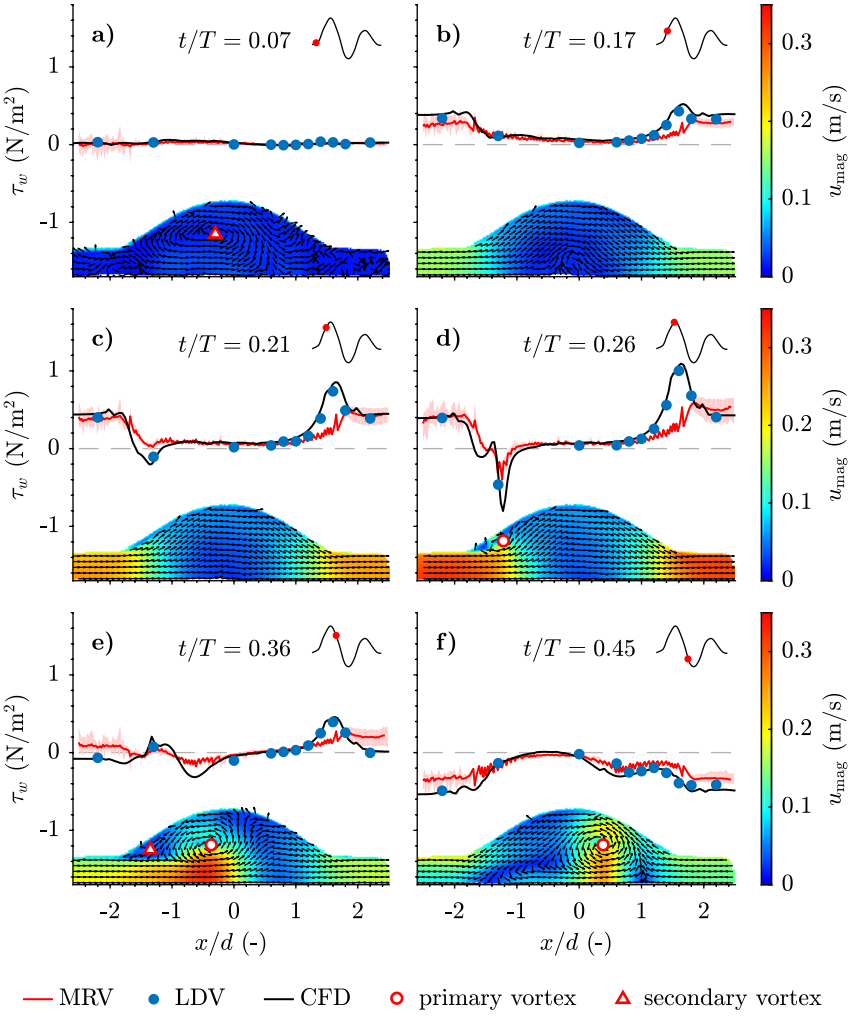

Figure 4.16: Spatial distribution of the WSS from MRV, LDV and CFD in the first half of the pulsation cycle. The respective flow rate at each time step is depicted in the upper right corners. The circumferentially averaged velocity field from MRV is shown on the bottom (using the right colorbar and the lower axis), while the spatial WSS distribution is depicted on top (using the left axis). Additionally, the vortex centers in the flow field are highlighted. Adapted from Bauer et al. (2020).

When the volume flow rate decreases, but is still positive (Figure 4.16e), the pressure gradient is already negative. The velocities at the wall, where viscous forces dominate over inertia forces, may follow the pressure gradient faster than the flow in the middle of the cross section. This causes a reversed flow at the wall and negative WSS values in the straight pipes of the inlet and outlet. Results from MRV still predict a positive value at these locations, because the WSS from MRV is measured 1-2 voxels away from the wall; hence, those negative velocities cannot be detected with MRV. The influence of the primary and secondary vortices on the WSS is observed in the region $-1.5 < x/d < 0$, leading to lower respectively higher WSS values in their direct vicinity.
At $t/T = 0.45$ (Figure 4.16f) the secondary vortex is dissipated, and the primary vortex introduces only a minor additional negative WSS on the wall. Overall, at this time step no peaks of the WSS can be observed; hence, the MRV yields a reasonable result of the WSS, which is only slightly underestimated.
The second half of the cycle is shown in Figure 4.17. Taken as a whole, the agreement between LDV and CFD is lower compared to the first half of the cycle, especially in the region where the vortex impinges onto the wall.
At the maximum negative volume flow rate ($t/T = 0.55$, Figure 4.17a), the primary vortex impinges onto the distal wall and induces high negative WSS values up to $\tau_w = -0.6\,\mathrm{N/m^2}$. In combination with the negative flow rate, the flow detaches from the wall distal of the primary vortex at $x/d = 1.4$ and proximal in its wake around $x/d \approx 0$. Hence, two secondary vortices emerge. This phenomenon could not be clearly identified from the non-averaged velocity field in Figure 4.12. At the proximal neck of the aneurysm, the identical phenomena as for the forward flow discussed in Figure 4.16b, Figure 4.16c and the steady flows, is observed: The region where the flow cross section narrows exhibits a high WSS. Since the flow direction is reversed, this peak is observed at the proximal neck at $x/d = -1.8$ with $\tau_w = -0.7\,\mathrm{N/m^2}$. This time step represents the most complex flow situation in the cycle, since it contains 3 vortex rings and multiple stagnation and detachment points. The numerical simulation shows good agreement with the wall shear stress values measured with LDV except around $x/d \approx 1.0$, where the computation shows higher WSS magnitudes.
At $t/T = 0.64$ (Figure 4.17b) the flow situation is again highly complex with at least 3 vortices. The WSS calculation from MRV data completely fails

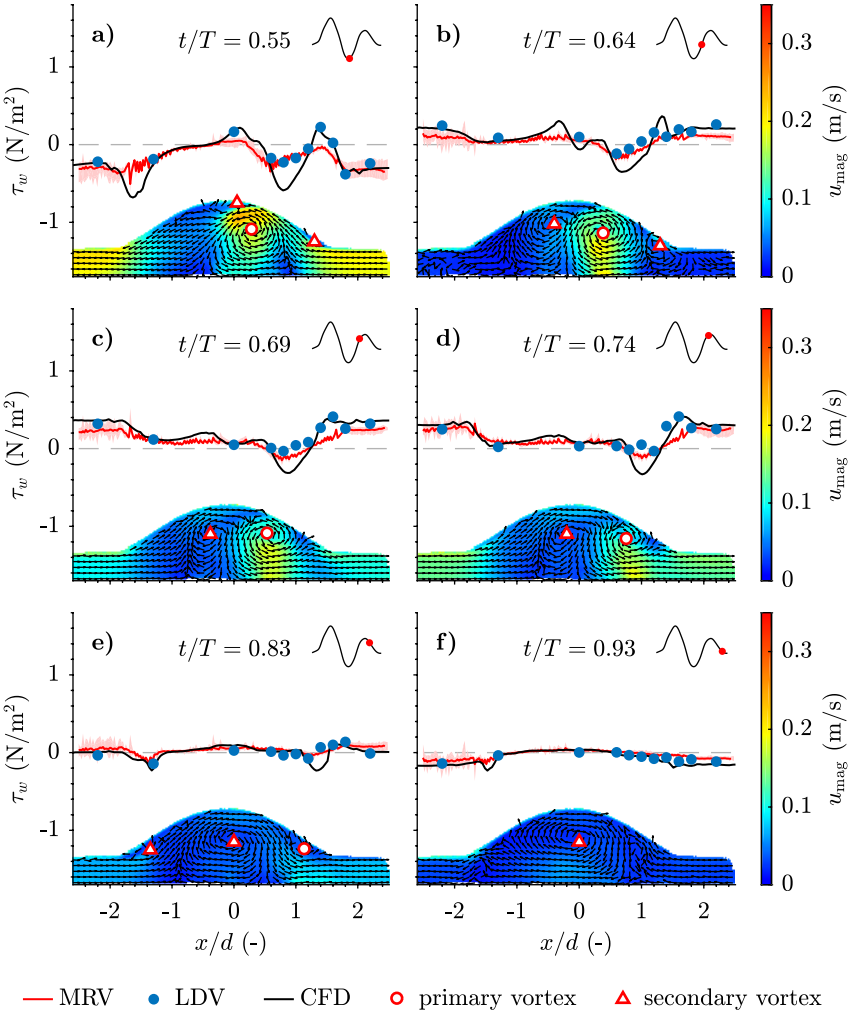

Figure 4.17: Spatial distribution of the WSS from MRV, LDV and CFD in the second half of the pulsation cycle. The respective flow rate at each time step is depicted in the upper right corners. The circumferentially averaged velocity field from MRV is shown on the bottom (using the right colorbar and the lower axis), while the spatial WSS distribution is depicted on top (using the left axis). Additionally, the vortex centers in the flow field are highlighted. Adapted from Bauer et al. (2020).

to predict the correct WSS distribution here. The CFD shows a localized positive WSS peak at $x/d = 1.4$ from the secondary vortex. In contrast, MRV and LDV do not show this peak.
Around the second maximum flow rate ($t/T = 0.69$ and $t/T = 0.74$, Figure 4.17c,d) the WSS distribution is comparable to the flow situation at $t/T = 0.21$ (Figure 4.16c), with a beginning detachment at the proximal end and a slightly increased WSS at the outflow. However, a major difference exists: The primary vortex strongly influences the WSS with $\tau_w = -0.4\,\mathrm{N/m^2}$ at the distal end.
In the next time step ($t/T = 0.83$, Figure 4.17e), the overall wall shear stress is close to zero, except at the proximal ($x/d = -1.5$) and distal ($x/d = 1.3$) ends, where the primary and a secondary vortices lead to $\tau_w \approx -0.1\,\mathrm{N/m^2}$.
At the end of the cycle (Figure 4.17f), the flow situation equals the situation at the beginning (Figure 4.16a).

4.2.4 Discussion

In summary, a vortex originates at every peak of the volume flow rate at the location where the cross section expands, which is the proximal end for positive flow rates and the distal end for negative flow rates. The wall shear stress is significantly altered in the region where those vortices are located in close proximity to the wall. The most prominent WSS peaks are found at the outlet of the aneurysm when the vortex impinges onto the wall, at the distal end at the highest volume flow rate, and at the position where the primary vortex ring initially develops. Compared to the first two peaks, the latter WSS peak is restricted not only to a very narrow spatial region of $\Delta x/d \approx 0.2$ (Figure 4.16d), but also to a short time interval. It is worth noting that the temporal gradient of the wall shear stress is most prominent at that position. Although the absolute values are higher at the distal end, their temporal evolution is quite predictable and the distribution changes only slowly. Compare for example the evolution of the high WSS value at $x/d = 1.6$ between Figure 4.16c and Figure 4.16d, or the high negative value at the same location between Figure 4.17a and Figure 4.17b with the temporal change at $x/d = -1.3$ between Figure 4.16d and Figure 4.16e.
For a more substantiated and quantitative evaluation of the WSS temporal change it is reasonable to calculate the temporal wall shear stress gradient

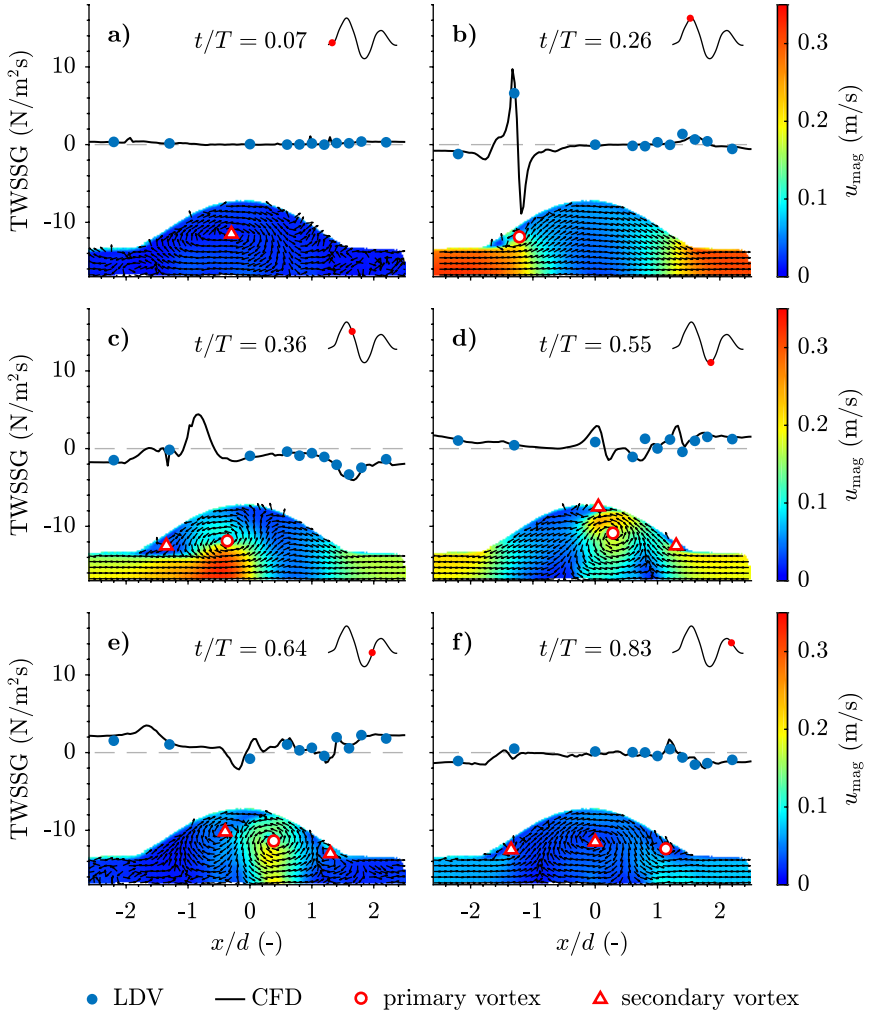

Figure 4.18: Temporal wall shear stress gradient (TWSSG) from LDV and CFD for different time steps during the cycle. A distinct peak is observed when the primary vortex detaches at the proximal end ($t/T = 0.26$). The circumferentially averaged velocity field from MRV is shown on the bottom (using the right colorbar and the lower axis), while the TWSSG distribution is depicted on top (using the left axis). Additionally, the vortex centers in the flow field are highlighted. Adapted from Bauer et al. (2020).

(TWSSG), which is a measure of the temporal change of the WSS at the respective spatial location. This quantity has also been discussed in literature, where the endothelium of the vessel was found to be sensitive to the TWSSG (White et al., 2001). The TWSSG is calculated from a central differencing scheme according to

$$\mathrm{TWSSG}(t_i) = \left.\frac{\partial \tau_w(x,t)}{\partial t}\right|_{t=t_i} \approx \frac{\tau_w(t_i+\Delta t) - \tau_w(t_i-\Delta t)}{2\Delta t}\,, \qquad (4.10)$$

where t_i is the respective time step in the cycle and Δt the time interval between two consecutive time steps. Results of the calculation of the TWSSG are shown for six representative time steps in Figure 4.18. Similar to the wall shear stress results, the agreement between LDV and CFD is very good. The magnitude of the TWSSG is below $\pm 4\,\mathrm{N/(m^2\,s)}$ for the entire cycle and all locations of the aneurysm, except for $t/T = 0.26$ (Figure 4.18b). At this point, two exceptionally high peaks of TWSSG $= \pm 10\,\mathrm{N/(m^2\,s)}$ are located at the position where the high temporal change of the WSS was initially assumed. There, the primary vortex begins to develop. In agreement with the CFD, the results from LDV show the same peak.

The temporal evolution of the WSS at this point ($x/d = -1.3$) is now analyzed in more detail and shown in Figure 4.19. While CFD and LDV results agree excellently up to $t/T = 0.3$ and fairly good in the later cycle, the MRV measurements systematically underestimate the WSS, especially the negative peak at $t/T = 0.25$. At the time the vortex ring starts to develop ($t/T \approx 0.2$), the WSS from LDV and CFD rapidly decreases from $\tau_w = 0.1\,\mathrm{N/m^2}$ to $\tau_w = -0.55\,\mathrm{N/m^2}$ and subsequently increases again to $\tau_w = 0.17\,\mathrm{N/m^2}$. The temporal change at this point appears in a short time interval of $\Delta t/T \approx 0.1$, which is in the same order of magnitude as the temporal resolution of the MRV measurement ($\Delta t/T \approx 0.05$). Thus, it is assumed that the underprediction from MRV not only originates from the low spatial resolution, but also from the limited temporal resolution.

To re-assess the effect of the intrinsic temporal averaging of MRV, the temporally high resolved WSS results from CFD are phase-averaged with different numbers of time steps (phases) during the cycle. The minimum number of only 1 time step corresponds to an overall mean value, while 21 time steps yield the same temporal resolution as the MRV measurement. In Figure 4.20a the results are depicted for 5, 20 and 40 phases. As expected, the use of fewer

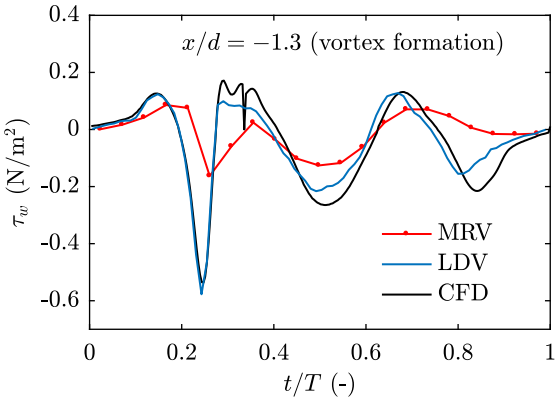

Figure 4.19: Temporal evolution of the WSS at the position where the primary vortex initially develops ($x/d = -1.3$). The vortex development close to the wall leads to a high negative WSS for a very short time period ($\Delta t/T = 0.1$), which cannot be resolved properly with MRV. (Reprinted from Bauer et al. (2020), with permission of Springer Nature. © 2020 Springer Nature.)

time steps yields a significant underestimation of the peak at $t/T = 0.25$. Figure 4.20b shows this specific underestimation of the peak at $t/T = 0.25$ in relation to the number of time steps. 0 % underestimation corresponds to the WSS value from the CFD with the highest temporal resolution (270 time steps). A high scatter can be noticed, which can be explained with the location of the time steps relative to the WSS peak. The upper bound of the distribution represents the situation when a time step coincides with the location of the peak, yielding less underestimation, while the lower bound represents a poorly matched position, resulting in a more pronounced underestimation. It can be seen that the underestimation due to a low temporal resolution can be significant. The WSS value calculated from the MRV data is also shown in Figure 4.20b. For the present 21 phases, the underprediction is approximately 70 %, which is significantly higher than the expected underprediction. It is assumed that this further underestimation originates from the low spatial resolution. Thus, it can be roughly divided into the underestimation due to a low temporal resolution (35 %) and due to a low spatial resolution (35 %).
In literature it is well known that the spatial resolution of MRV is not suffi-

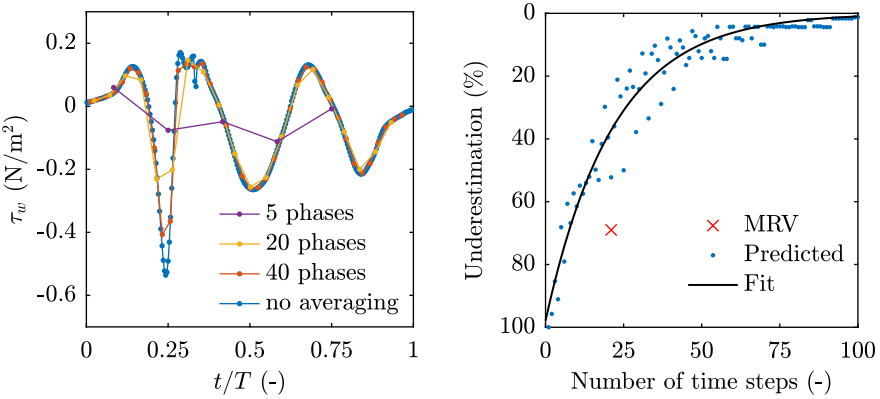

(a) Temporal evolution of the WSS at $x/d = -1.3$ with different numbers of time steps.

(b) Theoretical underestimation of the WSS at $x/d = -1.3$ in dependence on the number of time steps.

Figure 4.20: Underestimation of the WSS from temporal averaging. Adapted from Bauer et al. (2020).

cient to accurately determine the wall shear stress directly from the near-wall velocity gradient. However, it is in general not assumed that a low temporal resolution can reduce the wall shear stress estimation to the same order, which has been discussed in Montalba et al. (2018) and Zimmermann et al. (2018). The temporally highly resolved LDV and CFD results show that the underprediction may indeed be very large. Even for the case of a sufficiently high spatial resolution, an underprediction of approximately 35 % is expected with the present number of phases during the cycle.

Nevertheless, this effect is only present at the location where the primary vortex ring develops. This indicates that for an accurate determination of the wall shear stress it is not sufficient to calculate the WSS from individual MRV images acquired with a low temporal resolution in a step-by-step procedure without a proper representation of the flow field in-between those time steps. Furthermore, it is assumed that this effect cannot be solved by an interpolation between consecutive phases. As the only reasonable solution it is recommended to use dynamic MRI sequences with a high temporal resolution for abdominal aneurysms where strong vortices appear.

4.2.5 Summary: Unsteady Aneurysm

In this chapter, a detailed analysis of the time-resolved wall shear stress distribution in an aneurysm has been presented, which was not documented in literature in such a comprehensive extent. In accordance with previous investigations, the flow in the aneurysm is found to be in the laminar-turbulent transitional regime. Furthermore, a strong vortex ring is observed, which substantially influences the WSS distribution and leads to high wall shear stress amplitudes when it is located close to the wall.

A high peak of the WSS is present for a very limited time and in a very localized region where the primary vortex ring initially develops. The intrinsic temporal averaging during the acquisition of the MRV data is found to significantly decrease this peak. CFD results, which are averaged in the same manner, show a similar behavior. This indicates that besides the spatial resolution the temporal resolution is a crucial factor for the determination of the WSS. This needs to be considered - at least in flows where vortex rings are observed.

The agreement of the wall shear stress values between LDV measurements and the CFD simulation is found to be very good. In the second half of the pulsation cycle, minor deviations between both methods are present at the distal end of the aneurysm.

In this flow configuration, the deviation between the wall shear stress values obtained with MRV and the predicted values is most prominent, yielding an underprediction of 56 % at the distal end and even 70 % at the proximal end.

5 Conclusion and Outlook

This work was motivated by a high demand for *in vivo* measurements of the wall shear stress with MRV from the medical community. At the current state of the art, those measurements are highly biased. Furthermore, the 'true' *in vivo* WSS values remain unknown, inhibiting the evaluation of new post-processing methods. This fundamental problem - that the WSS values in flows measured with MRV are unknown - has been addressed with the present thesis. This has been accomplished by resorting to *in vitro* MRV measurements under well-defined flow conditions. Additionally, the 'true' WSS values have been measured with LDV to serve as a reference. The goal was to provide a *ground truth* of the WSS values and to establish a basis of standardized data sets to improve the comparability between different WSS estimators. In the context of this comparison step, such reference measurements are not yet available to such a comprehensive extent.

In the present work the human aorta has been chosen as a representative vessel. First, the flow conditions in the aorta were analyzed and simplified. Possible sources of errors were identified, enabling them to be avoided in the further analysis by means of a sequential increase of the complexity, starting from simple laminar flows up to unsteady flows using complex geometries. Special attention has been placed on the reproducibility and reliability of the measurements. This goal has been achieved, as shown with numerous comparisons of MRV and LDV data obtained for the exact same flow conditions. The comparability between MRV and LDV was excellent, although the measurements have been conducted on consecutive days and different locations.

In the course of this thesis a database has been established which contains the flows discussed in this work. These datasets include the MRV data as well as the corresponding wall shear stress values from LDV and has been used by the other research groups within the interdisciplinary project (Bopp et al., 2019a,b; Egger & Teschner, 2019; Shokina et al., 2019a,b). The MRV dataset

of the most realistic flow through an aneurysm model, which was examined in section 4.2, has furthermore been published online for other research groups to test their own WSS estimators (DOI:10.25534/tudatalib-113.2).
The data of this thesis also helped in the development of a new post-processing algorithm for the estimation of the WSS and for estimating the location of the vessel boundary. The algorithm proved to be independent of the spatial resolution, but is limited to pipe flows up to now. This work was performed by the group of Numerical and Scientific Computing at the Technische Universität Darmstadt (Egger & Teschner, 2019).

Beside the aforementioned measurements, further findings could be achieved. With the results reported on in section 4.2 it could be shown that not only the spatial resolution but also the temporal resolution may contribute to a significant and systematic under prediction of the WSS. This has been shown by examining unsteady flows with strong vortices, and is contrary to the widely shared notion that only spatial resolution is important. This is an important result since it implies that the estimation of the wall shear stress from single MRV images measured with common temporal resolutions may be biased. This applies even for sufficiently high spatial resolutions.
Furthermore, it was demonstrated in section 3.2 and section 4.2 that the laminar-turbulent transition can be qualitatively detected in the MRV images on the basis of occurring image artifacts. These artifacts are associated with an increase of the velocity uncertainty. Although this method does not allow a quantitative comparison of turbulence levels, it remains simple and requires neither a specialized MRI sequence nor extra measurement effort.
In this thesis a relatively simple method for the calculation of the WSS from MRV data has been employed, which uses finite differences and circumferentially averaged velocity profiles. The results obtained with this method clearly demonstrate that the underestimation of the WSS from MRV data increases with an increased complexity of the flow (1 - 9 % in steady pipe flows, 12 - 26 % in pulsating pipe flows, 26 % in steady flows through aneurysms and 56 % in pulsating flows through aneurysms). Thus, the systematic errors encountered in *in vivo* applications, where the complexity is further increased, are expected to be in the same order of magnitude or even higher. This clearly emphasizes

the need for a post-processing method, which does not strongly rely on data points close to the wall.

Despite the excellent agreement of the WSS values between LDV and the predictions from analytical solutions, the laser Doppler system achieved its theoretical limit regarding the spatial resolution. As has been demonstrated in section 3.2, the finite size of the detection volume might not be adequate to yield an absolute 'ground truth' value of the WSS. A systematic under prediction of the WSS in the LDV measurements is still present.
Moreover, it became apparent that the measurement of a spatial WSS distribution in complex geometries with LDV involves a very large experimental effort. Thus, for such geometries it seems appropriate and reasonable to resort to numerical simulations, as discussed in chapter 4. The results obtained with the IISRSM computational scheme exhibited very good agreement with experimental values. At least for the transitional and low-Reynolds number regime its use can therefore be recommended. However, an extensive comparison with experimental data, for example regarding the velocity fields, needs to be conducted to ensure that the numerical simulation coincides well with the measured values over the entire flow field.

Outlook

Although the present work can be considered successful, it does not solve the problem regarding a reliable and unbiased estimation of the wall shear stress from MRV data. This thesis only forms the basis for future wall shear stress estimators.
The flows considered in this study incorporate considerable simplifications and do not represent fully realistic *in vivo* conditions. For example, it is well known that the wall shear stress may be altered in geometries with rigid walls compared to the same flows through compliant models (Duncan et al., 1990; Lantz et al., 2011). In addition, the present work discusses only axial and symmetric flows, in which the circumferential velocity component has been neglected. In further investigations, the flows should therefore be extended accordingly to better reproduce *in vivo* conditions. As an example, elastic vessel walls made from transparent silicone and helical flows with a circumferential velocity component should be realized.

As mentioned above, the spatial resolution of LDV is not sufficiently high and can lead to underestimations of the WSS. For the present LDV system, a further decrease of the measurement volume size would lead to systematic errors, e.g. due to non-parallel interference fringes. A possible solution has been presented by Czarske (2001) with the use of a so-called laser profile sensor.
In contrast to conventional LDV systems, the laser profile sensor uses two separate laser pairs for each velocity direction. Thus, an one-component system requires two different wavelengths, resulting in two different but coinciding measurement volumes. The interference patterns are manipulated in such a way that the fringes of the first wavelength are converging, while the second measurement volume has diverging fringes. A particle passing through the measurement volume will scatter two different LDV signals, which will vary with its position in the measurement volume. Thus, the relative particle position in the measurement volume can be determined. The profile sensor allows a theoretical spatial resolution up to the order of 1 µm, which is significantly higher than a conventional LDV system.
Although its working principle has already been demonstrated in 2001, the system was not commercially available until the beginning of 2019. In a further step, this system could potentially improve the results and could finally lead to a 'real' ground truth measurement of the WSS.
Nevertheless, the development of MRV technology is also progressing. Extraordinary potential is currently expected from a new technique called *Compressed Sensing* (Lustig et al., 2007), which drastically accelerates the acquisition time, leaving more time for an increased spatio-temporal resolution. In the future the image quality will eventually improve to the extent that a significant increase of the reliability in the WSS measurements might be achieved. This would make complicated post-processing algorithms and thus LDV reference measurements obsolete. However, these advancements will probably still take some years. Nevertheless, there will always be a need to evaluate the measured and reconstructed results of the new sequences with other experimental data such as LDV, where this work and the corresponding data sets may continue to be useful.

Nomenclature

Small Greek Characters

α	$-$	aneurysm expansion ratio
δ	m	Stokes layer thickness
η	$\mathrm{Pa} \cdot \mathrm{s}$	dynamic viscosity
γ	$^{\mathrm{rad}}/_{\mathrm{sT}}$	gyromagnetic ratio
$\dot{\gamma}$	$^{1}/_{\mathrm{s}}$	shear rate
κ	$-$	von Kármán constant
λ_1, λ_2	m	wavelengths of the LDV laser beams
ν	$^{\mathrm{m}^2}/_{\mathrm{s}}$	kinematic viscosity
ω	Hz	angular (pulse) frequency
ω_L	Hz	Larmor frequency
ρ, ρ_f	$^{\mathrm{kg}}/_{\mathrm{m}^3}$	fluid density
ρ_p	$^{\mathrm{kg}}/_{\mathrm{m}^3}$	particle density
σ_{mag}	$-$	standard deviation of the MRV magnitude
σ_u	$^{\mathrm{m}}/_{\mathrm{s}}$	velocity uncertainty/fluctuation
σ_Φ	rad	phase uncertainty
τ	$^{\mathrm{N}}/_{\mathrm{m}^2}$	shear stress
τ_w	$^{\mathrm{N}}/_{\mathrm{m}^2}$	wall shear stress
τ_{w_0}	$^{\mathrm{N}}/_{\mathrm{m}^2}$	wall shear stress at the aneurysm inlet

τ_0	s	characteristic time of a seeding particle
θ	rad	intersection angle between LDV laser beams
ζ	–	aneurysm shape parameter

Capital Greek Characters

$\Delta\varphi_n$	rad	phase difference between pressure and flow rate
Λ_n	–	Womersley coefficient
$\mathbf{\Phi}$	rad	vector containing all phases in the ROI
Φ	rad	spin phase
Φ_0	rad	background phase
Ψ	–	residual function

Small Roman Characters

a	$\mathrm{m/s^2}$	acceleration
a_0, b_0, c_0	m	semi-axis of the measurement volume along x, y, z
a_d, b_d, c_d	m	semi-axis of the detection volume along x, y, z
b_s	m	beam separation at the LDV lens
c	–	constant
c_Δ	–	correction factor for the velocity uncertainty
d	m	pipe diameter
d_L	m	laser beam diameter
d_p	m	particle diameter
e	–	Euler's number
f	m	focal length
f_c	Hz	critical slip frequency

f_s	Hz	LDV shift frequency
g	$^{\mathrm{m}}/_{\mathrm{s}^2}$	gravitational acceleration
i	–	index / imaginary unit
j	–	number of phase wraps
l	m	length
$\vec{l}$	m	vector between aneurysm wall and the first voxel
n	–	index of summation
p	Pa	pressure
$\{r, \varphi, z\}$	–	cylindrical coordinate system
r_A	m	function of the aneurysm radius
r_w	m	beam waist radius
s	–	particle slip
t	s	time
t_A	s	arrival time of a tracer particle
t_i	s	time in the middle of the i-th interval
u, v, w	$^{\mathrm{m}}/_{\mathrm{s}}$	velocity in axial, circumferential, radial direction
u', v', w'	$^{\mathrm{m}}/_{\mathrm{s}}$	velocity fluctuation in the respective direction
u_{mag}	$^{\mathrm{m}}/_{\mathrm{s}}$	velocity magnitude
$\overline{u}$	$^{\mathrm{m}}/_{\mathrm{s}}$	time averaged velocity
u^+	–	dimensionless velocity
u_s	$^{\mathrm{m}}/_{\mathrm{s}}$	particle settling velocity
u_τ	$^{\mathrm{m}}/_{\mathrm{s}}$	wall shear velocity
u_t	$^{\mathrm{m}}/_{\mathrm{s}}$	wall-tangential velocity

$venc$	$^{m}/_{s}$	velocity encoding value
$\vec{x}$	m	position vector
$\{x, y, z\}$	m	Cartesian coordinate system
x_c, y_c	m	center point of the detection volume
y_0	m	initial guess of the wall position
y^+	–	dimensionless wall coordinate
y_s	m	particle settling distance

Capital Roman Characters

A	–	noise-free magnitude value
B	–	constant for the logarithmic law of the wall
B_0	T	magnetic field strength
C	–	constant
Co	–	Courant Number
D	m	maximum diamter of the aneurysm
G_s	$^{T}/_{m}$	spatial encoding gradient
G_v	$^{T}/_{m}$	velocity encoding gradient
L	m	aneurysm length
$\mathbf{M}$	–	vector containing all MRV magnitude values
M_0, M_1, M_2	–	magnetic gradient moments
M_z	$^{A}/_{m}$	axial magnetization
M_{xy}	$^{A}/_{m}$	transversal magnetization
N	–	upper bound of summation
N_{acq}	–	number of MRV acquisitions

N_c	–	number of receiver coils
P	W	power
P_0, P_n	Pa	amplitudes of the n-th harmonic pressure gradient
R	m	pipe radius
Ra	–	Rayleigh number
Re	–	Reynolds number
Re_{os}	–	amplitude of the oscillating Reynolds number
Re_{ta}	–	time averaged Reynolds number
ΔT	K	temperature difference between fluid and ambient
T	s	period time
T_1	s	spin-lattice relaxation time
T_2	s	spin-spin relaxation time
TE	s	echo time
TR	s	repetition time
T_{ambient}	K	ambient temperature
T_{fluid}	K	fluid temperature
TWSSG	$\mathrm{N/m^2 s}$	temporal wall shear stress gradient
U	$\mathrm{m/s}$	cross sectional mean velocity
U_0	$\mathrm{m/s}$	velocity amplitude
$\dot{V}$	$\mathrm{m^3/s}$	volume flow rate
$\dot{V}_0, \dot{V}_n$	$\mathrm{m^3/s}$	amplitudes of the n-th harmonic volume flow rate
V_{vox}	$\mathrm{m^3}$	voxel volume
Wo	–	Womersley number

Mathematical Operators

Δ	difference
$\langle\ \rangle$	arithmetic average
exp()	exponential function
var()	variance
$J_0(), J_1()$	Bessel function of the first kind zeroth/first order

Acronyms

2D1C	two-dimensional measurement with one velocity component
3D, 4D	three/four-dimensional
CDS	central differencing scheme
CFD	computational fluid dynamics
CT	computed tomography
DNS	direct numerical simulation
DV	detection volume
FOV	field of view
IISRSM	improved instability-sensitive Reynolds-stress model
LDV	laser Doppler velocimetry
MRI	magnetic resonance imaging
MRV	magnetic resonance velocimetry
MV	measurement volume
PC-MRI	phase-contrast magnetic resonance imaging
PIV	particle image velocimetry

PVC	polyvinyl chloride
RANS	Reynolds-averaged Navier-Stokes
RF	radio frequency
SIMPLE	semi-implicit method for pressure linked equations
SMX	static mixer with x-design
SNR	signal-to-noise ratio
TTL	transistor–transistor logic
TU	Technische Universität
TWSSG	temporal wall shear stress gradient
URANS	unsteady Reynolds-averaged Navier-Stokes
WSS	wall shear stress

List of Figures

List of Tables

Bibliography

Aggarwal, S., Qamar, A., Sharma, V., & Sharma, A. (2011). Abdominal aortic aneurysm: a comprehensive review. *Exp. Clin. Cardiol.*, 16(1):11.

Ahn, S., Shin, D., Tateshima, S., Tanishita, K., Vinuela, F., & Sinha, S. (2007). Fluid-induced wall shear stress in anthropomorphic brain aneurysm models: MR phase-contrast study at 3T. *J. Magn. Reson. Imaging*, 25(6):1120–1130.

Albrecht, H.-E., Damaschke, N., Borys, M., & Tropea, C. (2013). *Laser Doppler and Phase Doppler Measurement Techniques*. Springer-Verlag, Berlin Heidelberg.

Arzani, A. & Shadden, S. C. (2016). Characterizations and correlations of wall shear stress in aneurysmal flow. *J. Biomed. Eng.*, 138(1):014503.

Asbury, C. L., Ruberti, J. W., Bluth, E. I., & Peattie, R. A. (1995). Experimental investigation of steady flow in rigid models of abdominal aortic aneurysms. *Ann. Biomed. Eng.*, 23(1):29–39.

Atherton, T. J. & Kerbyson, D. J. (1999). Size invariant circle detection. *Image Vision Comput.*, 17(11):795–803.

Bauer, A., Bopp, M., Jakirlic, S., Tropea, C., Krafft, A. J., Shokina, N., & Hennig, J. (2020). Analysis of the wall shear stress in a generic aneurysm under pulsating and transitional flow conditions. *Exp. Fluids*, 61(2):59.

Bauer, A., Wegt, S., Bopp, M., Jakirlic, S., Tropea, C., Krafft, A. J., Shokina, N., Hennig, J., Teschner, G., & Egger, H. (2019). Comparison of wall shear stress estimates obtained by laser Doppler velocimetry, magnetic resonance imaging and numerical simulations. *Exp. Fluids*, 60(7):112.

Bauer, A., Wegt, S., Tropea, C., Krafft, A., Shokina, N., Hennig, J., Teschner, G., & Egger, H. (2018). Ground-truth for measuring wall shear stress with magnetic resonance velocimetry. In *19th International Symposium on Applications of Laser and Imaging Techniques to Fluid Mechanics, Lisbon, Portugal*.

Bauer, S., Markl, M., Föll, D., Russe, M., Stankovic, Z., & Jung, B. (2013). K-t GRAPPA accelerated phase contrast MRI: Improved assessment of blood flow and 3-directional myocardial motion during breath-hold. *J. Magn. Reson. Imaging*, 38(5):1054–1062.

Berg, P., Roloff, C., Beuing, O., Voss, S., Sugiyama, S.-I., Aristokleous, N., Anayiotos, A. S., Ashton, N., Revell, A., Bressloff, N. W., et al. (2015). The computational fluid dynamics rupture challenge 2013 - phase II: Variability of hemodynamic simulations in two intracranial aneurysms. *J. Biomed. Eng.*, 137(12):121008.

Bieging, E. T., Frydrychowicz, A., Wentland, A., Landgraf, B. R., Johnson, K. M., Wieben, O., & François, C. J. (2011). In vivo three-dimensional MR wall shear stress estimation in ascending aortic dilatation. *J. Magn. Reson. Imaging*, 33(3):589–597.

Bopp, M. (2018). Numerical simulation of pulsating flow in aneurysm models. Master's thesis, TU Darmstadt, Darmstadt, Germany.

Bopp, M., Bauer, A., Wegt, S., Jakirlic, S., & Tropea, C. (2019a). A computational and experimental study of physiological pulsatile flow in an aortic aneurysm. In *11th International Symposium on Turbulence and Shear Flow Phenomena, Southampton, UK*.

Bopp, M., Wegt, S., Bauer, A., Jakirlic, S., Tropea, C., Krafft, A., Shokina, N., & Hennig, J. (2019b). Harmonic and pulsatile flow in an aortic aneurysm model: Experiments and simulations. In *90th Annual Meeting of the International Association of Applied Mathematics and Mechanics, Vienna, Austria*.

Boussel, L., Rayz, V., Martin, A., Acevedo-Bolton, G., Lawton, M. T., Higashida, R., Smith, W. S., Young, W. L., & Saloner, D. (2009). Phase-contrast magnetic resonance imaging measurements in intracra-

nial aneurysms in vivo of flow patterns, velocity fields, and wall shear stress: comparison with computational fluid dynamics. *Magn. Reson. Med.*, 61(2):409–417.

Boussel, L., Rayz, V., McCulloch, C., Martin, A., Acevedo-Bolton, G., Lawton, M., Higashida, R., Smith, W. S., Young, W. L., & Saloner, D. (2008). Aneurysm growth occurs at region of low wall shear stress: patient-specific correlation of hemodynamics and growth in a longitudinal study. *Stroke*, 39(11):2997–3002.

Box, F. M., van der Geest, R. J., van der Grond, J., van Osch, M. J., Zwinderman, A. H., Palm-Meinders, I. H., Doornbos, J., Blauw, G.-J., van Buchem, M. A., & Reiber, J. H. (2007). Reproducibility of wall shear stress assessment with the paraboloid method in the internal carotid artery with velocity encoded MRI in healthy young individuals. *J. Magn. Reson. Imaging*, 26(3):598–605.

Boyd, A. J., Kuhn, D. C., Lozowy, R. J., & Kulbisky, G. P. (2016). Low wall shear stress predominates at sites of abdominal aortic aneurysm rupture. *J. Vasc. Surg.*, 63(6):1613–1619.

Brenn, G. (2016). *Analytical Solutions for Transport Processes.* Springer-Verlag, Berlin Heidelberg.

Bruschewski, M., Freudenhammer, D., Buchenberg, W., Schiffer, H.-P., & Grundmann, S. (2016). Estimation of the measurement uncertainty in magnetic resonance velocimetry based on statistical models. *Exp. Fluids*, 57(5):57–83.

Bruschewski, M., Scherhag, C., Schiffer, H.-P., & Grundmann, S. (2015). Influence of channel geometry and flow variables on cyclone cooling of turbine blades. In *ASME Turbo Expo 2015: Turbine Technical Conference and Exposition.*

Bruschewski, M., Schiffer, H.-P., & Grundmann, S. (2014). Measuring turbulent swirling flow with phase-contrast MRI. In *17th International Symposium on Applications of Laser and Imaging Techniques to Fluid Mechanics, Lisbon, Portugal.*

Budwig, R., Elger, D., Hooper, H., & Slippy, J. (1993). Steady flow in abdominal aortic aneurysm models. *J. Biomed. Eng.*, 115(4A):418–423.

Büttner, L., Bayer, C., Voigt, A., Czarske, J., Müller, H., Pape, N., & Strunck, V. (2008). Precise flow rate measurements of natural gas under high pressure with a laser Doppler velocity profile sensor. *Exp. Fluids*, 45(6):1103–1115.

Caro, C. G. (2012). *The Mechanics of the Circulation*. Cambridge University Press, Cambridge.

Çarpinlioğlu, M. Ö. & Gündogdu, M. Y. (2001). A critical review on pulsatile pipe flow studies directing towards future research topics. *Flow Meas. Instrum.*, 12(3):163–174.

Çarpinlioğlu, M. Ö. & Özahi, E. (2012). An updated portrait of transition to turbulence in laminar pipe flows with periodic time dependence (a correlation study). *Flow Turb. Combust.*, 89(4):691–711.

Carvalho, J. L., Nielsen, J.-F., & Nayak, K. S. (2010). Feasibility of in vivo measurement of carotid wall shear rate using spiral Fourier velocity encoded MRI. *Magn. Reson. Med.*, 63(6):1537–1547.

Cheng, C. P., Parker, D., & Taylor, C. A. (2002). Quantification of wall shear stress in large blood vessels using Lagrangian interpolation functions with cine phase-contrast magnetic resonance imaging. *Ann. Biomed. Eng.*, 30(8):1020–1032.

Chien, S. (1970). Shear dependence of effective cell volume as a determinant of blood viscosity. *Science*, 168(3934):977–979.

Chiu, J.-J. & Chien, S. (2011). Effects of disturbed flow on vascular endothelium: pathophysiological basis and clinical perspectives. *Physiol. Rev.*, 91(1):327–387.

Cibis, M., Potters, W. V., Gijsen, F. J., Marquering, H., VanBavel, E., Steen, A. F., Nederveen, A. J., & Wentzel, J. J. (2014). Wall shear stress calculations based on 3D cine phase contrast MRI and computational fluid dynamics: a comparison study in healthy carotid arteries. *NMR Biomed.*, 27(7):826–834.

Clauser, F. H. (1956). The turbulent boundary layer. In *Advances in applied mechanics*, volume 4, pages 1–51. Elsevier.

Constantinides, C. D., Atalar, E., & McVeigh, E. R. (1997). Signal-to-noise measurements in magnitude images from NMR phased arrays. *Magn. Reson. Med.*, 38(5):852–857.

Czarske, J. (2001). Laser Doppler velocity profile sensor using a chromatic coding. *Meas. Sci. Technol.*, 12(1):52.

Davies, P. F. (2009). Hemodynamic shear stress and the endothelium in cardiovascular pathophysiology. *Nat. Rev. Cardiol.*, 6(1):16.

D'Elia, M., Perego, M., & Veneziani, A. (2012). A variational data assimilation procedure for the incompressible Navier-Stokes equations in hemodynamics. *J. Sci. Comput.*, 52(2):340–359.

Deplano, V., Guivier-Curien, C., & Bertrand, E. (2016). 3D analysis of vortical structures in an abdominal aortic aneurysm by stereoscopic PIV. *Exp. Fluids*, 57(11):167.

Deplano, V., Knapp, Y., Bertrand, E., & Gaillard, E. (2007). Flow behaviour in an asymmetric compliant experimental model for abdominal aortic aneurysm. *J. Biomech.*, 40(11):2406–2413.

Deplano, V., Meyer, C., Guivier-Curien, C., & Bertrand, E. (2013). New insights into the understanding of flow dynamics in an in vitro model for abdominal aortic aneurysms. *Med. Eng. Phys.*, 35(6):800–809.

Dolan, J. M., Kolega, J., & Meng, H. (2013). High wall shear stress and spatial gradients in vascular pathology: a review. *Ann. Biomed. Eng.*, 41(7):1411–1427.

Duncan, D., Bargeron, C., Borchardt, S., Deters, O., Gearhart, S., Mark, F., & Friedman, M. (1990). The effect of compliance on wall shear in casts of a human aortic bifurcation. *J. Biomech. Eng.-T. ASME*, 112(2):183–188.

Durst, F., Ismailov, M., & Trimis, D. (1996a). Measurement of instantaneous flow rates in periodically operating injection systems. *Exp. Fluids*, 20:178–188.

Durst, F., Kikura, H., Lekakis, I., Jovanović, J., & Ye, Q. (1996b). Wall shear stress determination from near-wall mean velocity data in turbulent pipe and channel flows. *Exp. Fluids*, 20(6):417–428.

Durst, F., Müller, R., & Jovanovic, J. (1988). Determination of the measuring position in laser-Doppler anemometry. *Exp. Fluids*, 6(2):105–110.

Durst, F., Ray, S., Ünsal, B., & Bayoumi, O. (2005). The development lengths of laminar pipe and channel flows. *J. Fluid Eng.-T. ASME*, 127(6):1154–1160.

Dyverfeldt, P., Gårdhagen, R., Sigfridsson, A., Karlsson, M., & Ebbers, T. (2009). On MRI turbulence quantification. *Magn. Reson. Imaging*, 27(7):913–922.

Dyverfeldt, P., Kvitting, J.-P. E., Sigfridsson, A., Engvall, J., Bolger, A. F., & Ebbers, T. (2008). Assessment of fluctuating velocities in disturbed cardiovascular blood flow: in vivo feasibility of generalized phase-contrast MRI. *J. Magn. Reson.*, 28(3):655–663.

Efstathopoulos, E. P., Patatoukas, G., Pantos, I., Benekos, O., Katritsis, D., & Kelekis, N. L. (2008). Wall shear stress calculation in ascending aorta using phase contrast magnetic resonance imaging. Investigating effective ways to calculate it in clinical practice. *Phys. Medica*, 24(4):175–181.

Egelhoff, C., Budwig, R., Elger, D., Khraishi, T., & Johansen, K. (1999). Model studies of the flow in abdominal aortic aneurysms during resting and exercise conditions. *J. Biomech.*, 32(12):1319–1329.

Egger, H., Seitz, T., & Tropea, C. (2017). Enhancement of flow measurements using fluid-dynamic constraints. *J. Comput. Phys.*, 344:558–574.

Egger, H. & Teschner, G. (2019). On the stable estimation of flow geometry and wall shear stress from magnetic resonance images. *Inverse Probl.*, 35(9).

Einav, S. & Sokolov, M. (1993). An experimental study of pulsatile pipe flow in the transition range. *J. Biomech. Eng.-T. ASME*, 115(4A):404–411.

El Khoury, G. K., Schlatter, P., Noorani, A., Fischer, P. F., Brethouwer, G., & Johansson, A. V. (2013). Direct numerical simulation of turbulent pipe flow at moderately high Reynolds numbers. *Flow Turb. Combust.*, 91(3):475–495.

Elkins, C. J. & Alley, M. T. (2007). Magnetic resonance velocimetry: applications of magnetic resonance imaging in the measurement of fluid motion. *Exp. Fluids*, 43(6):823–858.

Fillinger, M. F., Raghavan, M. L., Marra, S. P., Cronenwett, J. L., & Kennedy, F. E. (2002). In vivo analysis of mechanical wall stress and abdominal aortic aneurysm rupture risk. *J. Vasc. Surg.*, 36(3):589–597.

Finol, E., Keyhani, K., & Amon, C. (2003). The effect of asymmetry in abdominal aortic aneurysms under physiologically realistic pulsatile flow conditions. *J. Biomed. Eng.*, 125(2):207–217.

Fortini, S., Espa, S., Querzoli, G., & Cenedese, A. (2015). Turbulence investigation in a laboratory model of the ascending aorta. *J. Turbul.*, 16(3):208–224.

Freudenhammer, D. (2017). *Magnetic Resonance Velocimetry for Unsteady Flows*. PhD thesis, TU Darmstadt.

Freudenhammer, D., Baum, E., Peterson, B., Böhm, B., Jung, B., & Grundmann, S. (2014). Volumetric intake flow measurements of an IC engine using magnetic resonance velocimetry. *Exp. Fluids*, 55(5):1724.

Frydrychowicz, A., Stalder, A. F., Russe, M. F., Bock, J., Bauer, S., Harloff, A., Berger, A., Langer, M., Hennig, J., & Markl, M. (2009). Three-dimensional analysis of segmental wall shear stress in the aorta by flow-sensitive four-dimensional-MRI. *J. Magn. Reson. Imaging*, 30(1):77–84.

Ghil, M. & Malanotte-Rizzoli, P. (1991). Data assimilation in meteorology and oceanography. In *Advances in geophysics*, volume 33, pages 141–266. Elsevier.

Glaßer, S., Lawonn, K., Hoffmann, T., Skalej, M., & Preim, B. (2014). Combined visualization of wall thickness and wall shear stress for the evaluation of aneurysms. *IEEE T. Vis. Comput. Gr.*, 20(12):2506–2515.

Gündogdu, M. Y. & Çarpinlioğlu, M. Ö. (1999a). Present state of art on pulsatile flow theory: Part 1: Laminar and transitional flow regimes. *JSME Int. J. B.-Fluid T.*, 42(3):384–397.

Gündogdu, M. Y. & Çarpinlioğlu, M. Ö. (1999b). Present state of art on pulsatile flow theory: Part 2: Turbulent flow regime. *JSME Int. J. B.-Fluid T.*, 42(3):398–410.

Gudbjartsson, H. & Patz, S. (1995). The Rician distribution of noisy MRI data. *Magn. Reson. Med.*, 34(6):910–914.

Haacke, E. M., Brown, R. W., Thomson, M. R., & Venkatesan, R. (1999). *Magnetic Resonance Imaging: Physical Principles and Sequence Design*. John Wiley & Sons.

Harloff, A., Berg, S., Barker, A., Schöllhorn, J., Schumacher, M., Weiller, C., & Markl, M. (2013). Wall shear stress distribution at the carotid bifurcation: influence of eversion carotid endarterectomy. *Eur. Radiol.*, 23(12):3361–3369.

Harloff, A., Nußbaumer, A., Bauer, S., Stalder, A. F., Frydrychowicz, A., Weiller, C., Hennig, J., & Markl, M. (2010). In vivo assessment of wall shear stress in the atherosclerotic aorta using flow-sensitive 4D MRI. *Magn. Reson. Med.*, 63(6):1529–1536.

Iguchi, M. & Ohmi, M. (1982). Transition to turbulence in a pulsatile pipe flow: Part 2, characteristics of reversing flow accompanied by relaminarization. *B. JSME*, 25(208):1529–1536.

Iguchi, M. & Ohmi, M. (1984). Transition to turbulence in a pulsatile pipe flow: 3rd report, flow regimes and the conditions describing the generation and decay of turbulence. *B. JSME*, 27(231):1873–1880.

Jakirlić, S. & Hanjalić, K. (2002). A new approach to modelling near-wall turbulence energy and stress dissipation. *J. Fluid Mech.*, 459:139–166.

Jakirlić, S. & Maduta, R. (2015). Extending the bounds of 'steady' RANS closures: Toward an instability-sensitive Reynolds stress model. *Int. J. Heat Fluid Fl.*, 51:175–194.

Jamison, R. A., Samarage, C. R., Bryson-Richardson, R. J., & Fouras, A. (2013). In vivo wall shear measurements within the developing zebrafish heart. *Plos One*, 8(10):e75722.

Janiga, G., Berg, P., Sugiyama, S., Kono, K., & Steinman, D. (2015). The computational fluid dynamics rupture challenge 2013 - phase I: prediction of rupture status in intracranial aneurysms. *Am. J. Neuroradiol.*, 36(3):530–536.

Jung, B., Stalder, A. F., Bauer, S., & Markl, M. (2011). On the undersampling strategies to accelerate time-resolved 3D imaging using k-t-GRAPPA. *Magn. Reson. Med.*, 66(4):966–975.

Jung, B., Ullmann, P., Honal, M., Bauer, S., Hennig, J., & Markl, M. (2008). Parallel MRI with extended and averaged GRAPPA kernels (PEAK-GRAPPA): optimized spatiotemporal dynamic imaging. *J. Magn. Reson. Imaging*, 28(5):1226–1232.

Kemmerling, E. M. & Peattie, R. A. (2018). Abdominal aortic aneurysm pathomechanics: Current understanding and future directions. In *Molecular, Cellular, and Tissue Engineering of the Vascular System*, pages 157–179. Springer.

Kendall, A. & Koochesfahani, M. (2008). A method for estimating wall friction in turbulent wall-bounded flows. *Exp. Fluids*, 44(5):773–780.

Köhler, U., Marshall, I., Robertson, M. B., Long, Q., Xu, X. Y., & Hoskins, P. R. (2001). MRI measurement of wall shear stress vectors in bifurcation models and comparison with CFD predictions. *J. Magn. Reson. Imaging*, 14(5):563–573.

Kousera, C., Wood, N., Seed, W., Torii, R., O'regan, D., & Xu, X. (2013). A numerical study of aortic flow stability and comparison with in vivo flow measurements. *J. Biomed. Eng.*, 135(1):011003.

Kyomen, S., Usui, T., Fukawa, M., & Ohmi, M. (1996). Combined free and forced convection for laminar steady flow in horizontal tubes. *JSME Int. J. B.-Fluid T.*, 39(1):44–50.

Lambossy, P. (1952). Oscillations forcées d'un liquide incompressible et visqueux dans un tube rigide et horizontal : calcul de la force de frottement. *Helv. Phys. Acta*, 25:371–386.

Lantz, J., Renner, J., & Karlsson, M. (2011). Wall shear stress in a subject specific human aorta - influence of fluid-structure interaction. *Int. J. Appl. Mech.*, 3(04):759–778.

Lasheras, J. C. (2007). The biomechanics of arterial aneurysms. *Annu. Rev. Fluid Mech.*, 39:293–319.

Levine, H. J. et al. (1997). Rest heart rate and life expectancy. *J. Am. Coll. Cardiol.*, 30(4):1104–1106.

Liepsch, D., Moravec, S., & Baumgart, R. (1992). Some flow visualization and laser-Doppler-velocity measurements in a true-to-scale elastic model of a human aortic arch - a new model technique. *Biorheology*, 29(5-6):563–580.

Lusis, A. J. (2000). Atherosclerosis. *Nature*, 407(6801):233–241.

Lustig, M., Donoho, D., & Pauly, J. M. (2007). Sparse MRI: The application of compressed sensing for rapid MR imaging. *Magn. Reson. Med.*, 58(6):1182–1195.

Mally, T. (2019). Investigation of the relaminarization in pulsating flows for MRV experiments. Master's thesis, TU Darmstadt, Darmstadt, Germany.

Markl, M., Frydrychowicz, A., Kozerke, S., Hope, M., & Wieben, O. (2012). 4D flow MRI. *J. Magn. Reson. Imaging*, 36(5):1015–1036.

Markl, M., Wallis, W., & Harloff, A. (2011). Reproducibility of flow and wall shear stress analysis using flow-sensitive four-dimensional MRI. *J. Magn. Reson. Imaging*, 33(4):988–994.

Markl, M., Wegent, F., Zech, T., Bauer, S., Strecker, C., Schumacher, M., Weiller, C., Hennig, J., & Harloff, A. (2010). In vivo wall shear stress distribution in the carotid artery: effect of bifurcation geometry, internal carotid artery stenosis, and recanalization therapy. *Circ.-Cardiovasc.-Imag.*, 3(6):647–655.

McMahon, T. A. & Bonner, J. T. (1983). *On Size and Life*. Scientific American Library, New York.

McRobbie, D. W., Moore, E. A., Graves, M. J., & Prince, M. R. (2006). *MRI: From Picture to Proton*. Cambridge University Press, Cambridge.

Meng, H., Wang, Z., Hoi, Y., Gao, L., Metaxa, E., Swartz, D. D., & Kolega, J. (2007). Complex hemodynamics at the apex of an arterial bifurcation induces vascular remodeling resembling cerebral aneurysm initiation. *Stroke*, 38(6):1924–1931.

Miura, Y., Ishida, F., Umeda, Y., Tanemura, H., Suzuki, H., Matsushima, S., Shimosaka, S., & Taki, W. (2013). Low wall shear stress is independently associated with the rupture status of middle cerebral artery aneurysms. *Stroke*, 44(2):519–521.

Montalba, C., Urbina, J., Sotelo, J., Andia, M. E., Tejos, C., Irarrazaval, P., Hurtado, D. E., Valverde, I., & Uribe, S. (2018). Variability of 4D flow parameters when subjected to changes in MRI acquisition parameters using a realistic thoracic aortic phantom. *Magn. Reson. Med.*, 79(4):1882–1892.

Moore, J. E. & Ku, D. N. (1994). Pulsatile velocity measurements in a model of the human abdominal aorta under resting conditions. *J. Biomed. Eng.*, 116(3):337–346.

Munarriz, P. M., Gómez, P. A., Paredes, I., Castaño-Leon, A. M., Cepeda, S., & Lagares, A. (2016). Basic principles of hemodynamics and cerebral aneurysms. *World Neurosurg.*, 88:311–319.

Musker, A. (1979). Explicit expression for the smooth wall velocity distribution in a turbulent boundary layer. *AIAA J.*, 17(6):655–657.

Musto, R. & Roach, M. R. (1980). Flow studies in glass models of aortic aneurysms. *Can. J. Surg.*, 23(5):452–455.

NEMA (2014). Determination of signal-to-noise ratio (SNR) in diagnostic magnetic resonance imaging. *NEMA Standards Publication MS 1-2008 (2014)*.

Nerem, R. M., Seed, W. A., & Wood, N. B. (1972). An experimental study of the velocity distribution and transition to turbulence in the aorta. *J. Fluid Mech.*, 52(1):137–160.

Oeppen, J., Vaupel, J. W., et al. (2002). Broken limits to life expectancy. *Science*, 296(5570):1029–1031.

Ohmi, M., Iguchi, M., & Urahata, I. (1982). Transition to turbulence in a pulsatile pipe flow part 1, wave forms and distribution of pulsatile velocities near transition region. *B. JSME*, 25(200):182–189.

Otsu, N. (1979). A threshold selection method from gray-level histograms. *IEEE T. Syst. Man Cyb.*, 9(1):62–66.

Oyre, S., Pedersen, E. M., Ringgaard, S., Boesiger, P., & Paaske, W. (1997). In vivo wall shear stress measured by magnetic resonance velocity mapping in the normal human abdominal aorta. *Eur. J. Vasc. Endovasc.*, 13(3):263–271.

Papathanasopoulou, P., Zhao, S., Köhler, U., Robertson, M. B., Long, Q., Hoskins, P., Yun Xu, X., & Marshall, I. (2003). MRI measurement of time-resolved wall shear stress vectors in a carotid bifurcation model, and comparison with CFD predictions. *J. Magn. Reson. Imaging*, 17(2):153–162.

Paul, E. L., Atiemo-Obeng, V. A., & Kresta, S. M. (2004). *Handbook of Industrial Mixing: Science and Practice*. John Wiley & Sons.

Peattie, R. A., Asbury, C. L., Bluth, E. I., & Riehle, T. J. (1996a). Steady flow in models of abdominal aortic aneurysms. Part II: Wall stresses and their implication for in vivo thrombosis and rupture. *J. Ultras. Med.*, 15(10):689–696.

Peattie, R. A., Asbury, C. L., Bluth, E. I., & Ruberti, J. W. (1996b). Steady flow in models of abdominal aortic aneurysms. Part I: Investigation of the velocity patterns. *J. Ultras. Med.*, 15(10):679–688.

Peattie, R. A., Riehle, T. J., & Bluth, E. I. (2004). Pulsatile flow in fusiform models of abdominal aortic aneurysms: flow fields, velocity patterns and flow-induced wall stresses. *J. Biomed. Eng.*, 126(4):438–446.

Perktold, K. (1987). On the paths of fluid particles in an axisymmetrical aneurysm. *J. Biomech.*, 20(3):311–317.

Petersson, S., Dyverfeldt, P., & Ebbers, T. (2012). Assessment of the accuracy of MRI wall shear stress estimation using numerical simulations. *J. Magn. Reson. Imaging*, 36(1):128–138.

Petersson, S., Dyverfeldt, P., Gårdhagen, R., Karlsson, M., & Ebbers, T. (2010). Simulation of phase contrast MRI of turbulent flow. *Magn. Reson. Med.*, 64(4):1039–1046.

Piatti, F., Pirola, S., Bissell, M., Nesteruk, I., Sturla, F., Della Corte, A., Redaelli, A., & Votta, E. (2017). Towards the improved quantification of in vivo abnormal wall shear stresses in BAV-affected patients from 4D-flow imaging: Benchmarking and application to real data. *J. Biomech.*, 50:93–101.

Poelma, C., Vennemann, P., Lindken, R., & Westerweel, J. (2008). In vivo blood flow and wall shear stress measurements in the vitelline network. *Exp. Fluids*, 45(4):703–713.

Potters, W. V., Ooij, P., Marquering, H., vanBavel, E., & Nederveen, A. J. (2015). Volumetric arterial wall shear stress calculation based on cine phase contrast MRI. *J. Magn. Reson. Imaging*, 41(2):505–516.

Ramaprian, B. & Tu, S.-W. (1980). An experimental study of oscillatory pipe flow at transitional Reynolds numbers. *J. Fluid Mech.*, 100(3):513–544.

Ray, S., Ünsal, B., & Durst, F. (2012). Development length of sinusoidally pulsating laminar pipe flows in moderate and high Reynolds number regimes. *Int. J. Heat Fluid Fl.*, 37:167–176.

Rodríguez-López, E., Bruce, P. J., & Buxton, O. R. (2015). A robust post-processing method to determine skin friction in turbulent boundary layers from the velocity profile. *Exp. Fluids*, 56(4):68.

Salsac, A.-V., Sparks, S., Chomaz, J.-M., & Lasheras, J. (2006). Evolution of the wall shear stresses during the progressive enlargement of symmetric abdominal aortic aneurysms. *J. Fluid Mech.*, 560:19–51.

Schenck, J. F. (1996). The role of magnetic susceptibility in magnetic resonance imaging: MRI magnetic compatibility of the first and second kinds. *Med. Phys.*, 23(6):815–849.

Scherer, P. W. (1973). Flow in axisymmetrical glass model aneurysms. *J. Biomech.*, 6(6):695–700.

Schneiders, J. F. & Scarano, F. (2016). Dense velocity reconstruction from tomographic PTV with material derivatives. *Exp. Fluids*, 57(9):139.

Shokina, N., Bauer, A., Teschner, G., Buchenberg, W. B., Tropea, C., Egger, H., Hennig, J., & Krafft, A. J. (2019a). Mr-based wall shear stress measurements in fully developed turbulent flow using the Clauser plot method. *J. Magn. Reson.*, 305:16 – 21.

Shokina, N., Teschner, G., Bauer, A., Tropea, C., Egger, H., Hennig, J., & Krafft, A. (2019b). Quantification of wall shear stress in large blood vessels using magnetic resonance imaging. *Comput. Techn.*, 24(4):4–27.

Siegel, R. L., Miller, K. D., & Jemal, A. (2018). Cancer statistics, 2018. *CA-Cancer J. Clin.*, 68(1):7–30.

Spurk, J. (2013). *Strömungslehre: Einführung in die Theorie der Strömungen*. Springer-Verlag, Berlin Heidelberg.

Stalder, A. F., Russe, M., Frydrychowicz, A., Bock, J., Hennig, J., & Markl, M. (2008). Quantitative 2D and 3D phase contrast MRI: optimized analysis of blood flow and vessel wall parameters. *Magn. Reson. Med.*, 60(5):1218–1231.

Stehbens, W. E. (1974). Flow disturbances in glass models of aneurysms at low Reynolds numbers. *Q. J. Exp. Physiol. CMS.*, 59(2):167–174.

Steinman, D. A., Hoi, Y., Fahy, P., Morris, L., Walsh, M. T., Aristokleous, N., Anayiotos, A. S., Papaharilaou, Y., Arzani, A., Shadden, S. C., et al. (2013). Variability of computational fluid dynamics solutions for pressure and flow in a giant aneurysm: the ASME 2012 summer bioengineering conference CFD challenge. *J. Biomed. Eng.*, 135(2):021016.

Tropea, C. & Yarin, A. L. (2007). *Springer Handbook of Experimental Fluid Mechanics*. Springer-Verlag, Berlin Heidelberg.

Valen-Sendstad, K., Bergersen, A. W., Shimogonya, Y., Goubergrits, L., Bruening, J., Pallares, J., Cito, S., Piskin, S., Pekkan, K., Geers, A. J., et al. (2018). Real-world variability in the prediction of intracranial aneurysm wall shear stress: the 2015 international aneurysm CFD challenge. *Cardiovas. Eng. Techn.*, 9(4):544–564.

Van Ooij, P., Potters, W. V., Guédon, A., Schneiders, J. J., Marquering, H. A., Majoie, C. B., vanBavel, E., & Nederveen, A. J. (2013). Wall shear stress estimated with phase contrast MRI in an in vitro and in vivo intracranial aneurysm. *J. Magn. Reson. Imaging*, 38(4):876–884.

Van Ooij, P., Potters, W. V., Nederveen, A. J., Allen, B. D., Collins, J., Carr, J., Malaisrie, S. C., Markl, M., & Barker, A. J. (2015). A methodology to detect abnormal relative wall shear stress on the full surface of the thoracic aorta using four-dimensional flow MRI. *Magn. Reson. Med.*, 73(3):1216–1227.

Vennemann, P., Lindken, R., & Westerweel, J. (2007). In vivo whole-field blood velocity measurement techniques. *Exp. Fluids*, 42(4):495–511.

Vorp, D. A., Raghavan, M., & Webster, M. W. (1998). Mechanical wall stress in abdominal aortic aneurysm: influence of diameter and asymmetry. *J. Vasc. Surg.*, 27(4):632–639.

Watton, P., Selimovic, A., Raberger, N. B., Huang, P., Holzapfel, G., & Ventikos, Y. (2011). Modelling evolution and the evolving mechanical environment of saccular cerebral aneurysms. *Biomech. Model. Mechan.*, 10(1):109–132.

White, C. R., Haidekker, M., Bao, X., & Frangos, J. A. (2001). Temporal gradients in shear, but not spatial gradients, stimulate endothelial cell proliferation. *Circulation*, 103(20):2508–2513.

Wolak, A., Gransar, H., Thomson, L. E., Friedman, J. D., Hachamovitch, R., Gutstein, A., Shaw, L. J., Polk, D., Wong, N. D., Saouaf, R., et al. (2008). Aortic size assessment by noncontrast cardiac computed tomography: normal limits by age, gender, and body surface area. *JACC-Cardiovasc. Imag.*, 1(2):200–209.

Womersley, J. R. (1955). Method for the calculation of velocity, rate of flow and viscous drag in arteries when the pressure gradient is known. *J. Physiol.-London*, 127:553–563.

Yang, Y., Cai, S., Mémin, E., & Heitz, D. (2017). Ensemble-variational methods in data assimilation. In *2nd Workshop on Data Assimilation and CFD Processing for PIV and Lagrangian Particle Tracking.*

Yip, T. & Yu, S. (2001). Cyclic transition to turbulence in rigid abdominal aortic aneurysm models. *Fluid Dyn. Res.*, 29(2):81–113.

Yip, T. & Yu, S. (2003). Cyclic flow characteristics in an idealized asymmetric abdominal aortic aneurysm model. *P. I. Mech. Eng. H*, 217(1):27–39.

Zhang, F., Barker, A., Gates, P., Strain, W., Fulford, J., Mazzaro, L., Shore, A., Bellenger, N., Lanning, C., & Shandas, R. (2009). Noninvasive wall shear stress measurements in human carotid artery using echo particle image velocimetry: initial clinical studies. In *2009 IEEE International Ultrasonics Symposium*, pages 562–565.

Zhang, Z. (2004). Optical guidelines and signal quality for LDA applications in circular pipes. *Exp. Fluids*, 37(1):29–39.

Zhou, X., Leow, C. H., Rowland, E., Riemer, K., Rubin, J. M., Weinberg, P. D., & Tang, M.-X. (2018). 3D velocity and volume flow measurement in vivo using speckle decorrelation and 2D high-frame-rate contrast-enhanced ultrasound. *IEEE T. Ultras. Ferr.*, 65(12):2233–2244.

Zimmermann, J., Demedts, D., Mirzaee, H., Ewert, P., Stern, H., Meierhofer, C., Menze, B., & Hennemuth, A. (2018). Wall shear stress estimation in the aorta: Impact of wall motion, spatiotemporal resolution, and phase noise. *J. Magn. Reson. Imaging*, 48(3):718–728.